
Observed and modeled biogeochemistry of filaments off Peru

A thesis submitted in fulfillment of
the requirements for the degree:

Master of Science

Climate Physics: Meteorology and Physical Oceanography

Faculty of Mathematics and Natural Sciences
Christian-Albrechts-Universität zu Kiel

Kiel, December 2017

Author: Jaard-Okke Frederik Hauschildt
Matrikel-Nr. 5657

- 1. Advisor:** Prof. Dr. Andreas Oschlies
- 2. Advisor:** Dr. Sören Thomsen

Abstract

The biogeochemistry of an observed cold filament off Peru and the representation of filaments in submesoscale-permitting ($1/45^\circ$) coupled biogeochemical model simulations are the focus of this thesis. Furthermore, we use the simulations to investigate the effect of submesoscale frontal processes on the distribution of biogeochemical tracers in the shallow oxygen minimum zone off Peru. The observed filament contains relatively cold, fresh and nutrient-rich waters originating in the coastal upwelling. Enhanced nitrate concentrations and offshore velocities of up to 0.5 m s^{-1} within the filament suggest an offshore transport of nutrients. Despite low chlorophyll α concentrations in the core of the filament, depth integrated primary production is 40% higher than at the upwelling front and 25% higher than offshore. The highly variable relationship of surface chlorophyll α and depth-integrated primary production highlights the inherent uncertainty of primary production estimates based on ocean-color measured by satellites. The observations are used to assess the results of two different biogeochemical model simulations (PISCES / BioEBUS). Both simulations exhibit filaments that are similar in lateral scale, horizontal and vertical structure and offshore extent to those observed, but differences exist in the biogeochemistry: While the PISCES simulation exhibits nitrate concentrations within filaments comparable to observations, filaments are largely depleted of nitrate in the BioEBUS simulation. This difference can be related to a higher phytoplankton growth rate and faster nitrate uptake in BioEBUS. The importance of sufficiently slow phytoplankton growth for maintaining realistic concentrations of upwelled nutrients offshore is therefore stressed. Furthermore, the simulations suggest that submesoscale frontal processes increase subduction and offshore export of nitrate which leads to reduced primary production. An increase in oxygen that resembles the pattern of the decrease in nitrate suggests a ventilation of the shallow oxygen minimum zone off Peru by vertical and horizontal eddy-fluxes.

Zusammenfassung

Die Biogeochemie eines beobachteten Kaltwasserfilaments vor Peru und die Darstellung von Filamenten in gekoppelten biogeochemischen Modellsimulationen die Teile des submesoskaligen Regimes explizit auflösen ($1/45^\circ$) sind der Fokus dieser Masterarbeit. Zusätzlich verwenden wir die Simulationen, um den Effekt von submesoskaligen Frontenprozessen auf biogeochemische Tracerverteilungen in der oberflächennahen Sauerstoffminimumzone vor Peru zu untersuchen. Das beobachtete Filament enthält relativ kaltes, frisches und nährstoffreiches Wasser, das dem küstennahen Auftriebsgebiet entstammt. Erhöhte Nitratkonzentrationen und seewärtige Strömungsgeschwindigkeiten von bis zu 0.5 m s^{-1} innerhalb des Filaments deuten auf einen seewärtigen Transport von Nitrat hin. Trotz niedriger Chlorophyll α Konzentrationen im Kern des Filaments ist die über die Tiefe integrierte Primärproduktion um 40% höher als an der Auftriebsfront und um 25% höher als im offenen Ozean. Die sehr variable Beziehung von Chlorophyll α an der Oberfläche und der über die Tiefe integrierten Primärproduktion zeigt die Unsicherheit auf, die mit Schätzungen der Primärproduktion auf Basis von Satellitenmessungen verbunden ist. Die Beobachtungen werden benutzt um zwei unterschiedliche biogeochemische Modellsimulationen (PISCES / BioEBUS) zu bewerten. Beide Simulationen zeigen Filamente die den beobachteten in der seitlichen und der seewärtigen Ausdehnung sowie in der horizontalen und vertikalen Struktur ähneln, aber es existieren Unterschiede in der Biogeochemie: Während die PISCES Simulation mit Beobachtungen vergleichbare Nitratkonzentrationen innerhalb von Filamenten zeigt, ist das Nitrat in Filamenten in der BioEBUS Simulation größtenteils aufgebraucht. Dieser Unterschied kann mit einer höheren Wachstumsrate von Phytoplankton und damit schnellerer Nitrataufnahme in BioEBUS in Verbindung gebracht werden. Die Bedeutung von ausreichend langsamem Phytoplankton-Wachstum für das Aufrechterhalten realistischer Konzentrationen von aufgetriebenen Nährstoffen im offenen Ozean wird daher betont. Weiterhin deuten die Simulationen darauf hin, dass submesoskalige Frontenprozesse die Subduktion und den Export von Nitrat in den off-

fenen Ozean erhöhen, was zu verringerter Primärproduktion führt. Eine Zunahme von Sauerstoff die dem Muster der Abnahme von Nitrat ähnelt deutet auf eine Ventilation der oberflächennahen Sauerstoffminimumzone vor Peru durch vertikale und horizontale Wirbelflüsse hin.

Contents

1 Introduction	9
2 Historical measurements in the upwelling off Peru	14
3 Filament survey	17
3.1 Hydrographic and meteorological measurements	18
3.2 Biogeochemical measurements	19
3.3 Satellite measurements	20
4 Coupled Physical-Biogeochemical Model	22
4.1 Physical model	22
4.2 Biogeochemical models	23
4.3 Impact of increased horizontal resolution	25
4.4 Impact of biogeochemical model choice	31
5 Characterization of an observed cold filament	36
5.1 Oceanographic setting	36
5.2 Cold filament	45
6 Representation of filaments in biogeochemical model simulations	57
6.1 PISCES	57
6.2 BioEBUS	62
6.3 Comparison and synthesis of observed and modeled filament characteristics	66
7 Discussion	74
7.1 Variability of chlorophyll and primary production in the Peru upwelling	74
7.2 Impact of the model formulation on the biogeochemistry of filaments	82
7.3 Effect of submesoscale processes on the biogeochemistry of the Peru upwelling system	89
8 Summary and Outlook	95

1 Introduction

The eastern margins of the subtropical oceans are characterized by upwelling of cold and nutrient-rich subsurface waters, caused by persistent along-shore winds that drive an offshore Ekman transport. The nutrients supplied to the sunlit surface ocean subsequently fuel high phytoplankton growth which supports a rich ecosystem ([Pennington et al., 2006](#)). These Eastern Boundary Upwelling Systems (EBUS) are found in all major ocean basins and named after the Canary, Benguela, California, and Peru-Chile current systems. The Peru-Chile upwelling system (PCUS) is the most productive EBUS in the world ocean accounting for 10 % of the global fishery production while occupying only 0.1 % of the ocean surface ([Chavez et al., 2008](#)). Furthermore, the high productivity and export of organic matter from the euphotic zone and its subsequent remineralization at depth by oxygen-consuming organisms lead to - in conjunction with poor ventilation by sluggish currents - the presence of the shallowest and most intense oxygen minimum zone (OMZ) in the world ocean which in turn affects marine life ([Wyrtki, 1962](#); [Paulmier et al., 2006](#); [Karstensen et al., 2008](#); [Stramma et al., 2010](#)). Because of the shallow oxycline that varies between only 10 m - 80 m depth and is often around 30 m ([Hammersley et al., 2007](#)), submesoscale frontal processes could potentially be important for its ventilation. The Peru upwelling ecosystem and the fisheries that depend on it thus have immense economical importance for the local population. Global relevance is given to EBUS by their role as natural sources of climate relevant trace gases to the atmosphere such as N₂O ([Friederich et al., 2008](#); [Arévalo-Martínez et al., 2015](#)) and CO₂ ([Chavez et al., 2007](#); [Gruber, 2015](#)). Two main along-shore currents off Peru are relevant for this study (Fig. 1): At the subsurface, the Peru-Chile Undercurrent flows poleward with a velocity of 10- 15 cm s⁻¹ at 100 m - 150 m depth along the shelf ([Wyrtki, 1963, 1967](#); [Brink, 1983](#); [Huyer et al., 1991](#); [Strub et al., 1998](#); [Penven et al., 2005](#); [Colas et al., 2012](#); [Chaigneau et al., 2013](#)). At the surface the Peru Coastal Current flows equatorward ([Penven et al., 2005](#)), but not continuously: Between 11°S - 16°S, southward surface velocities of 10- 15 cm s⁻¹ are observed, related to a near-surfacing of the PCUC ([Chaigneau et al., 2013](#)). At 14°S a persistent eddy-like feature is observed, which results in mean offshore velocities at this latitude

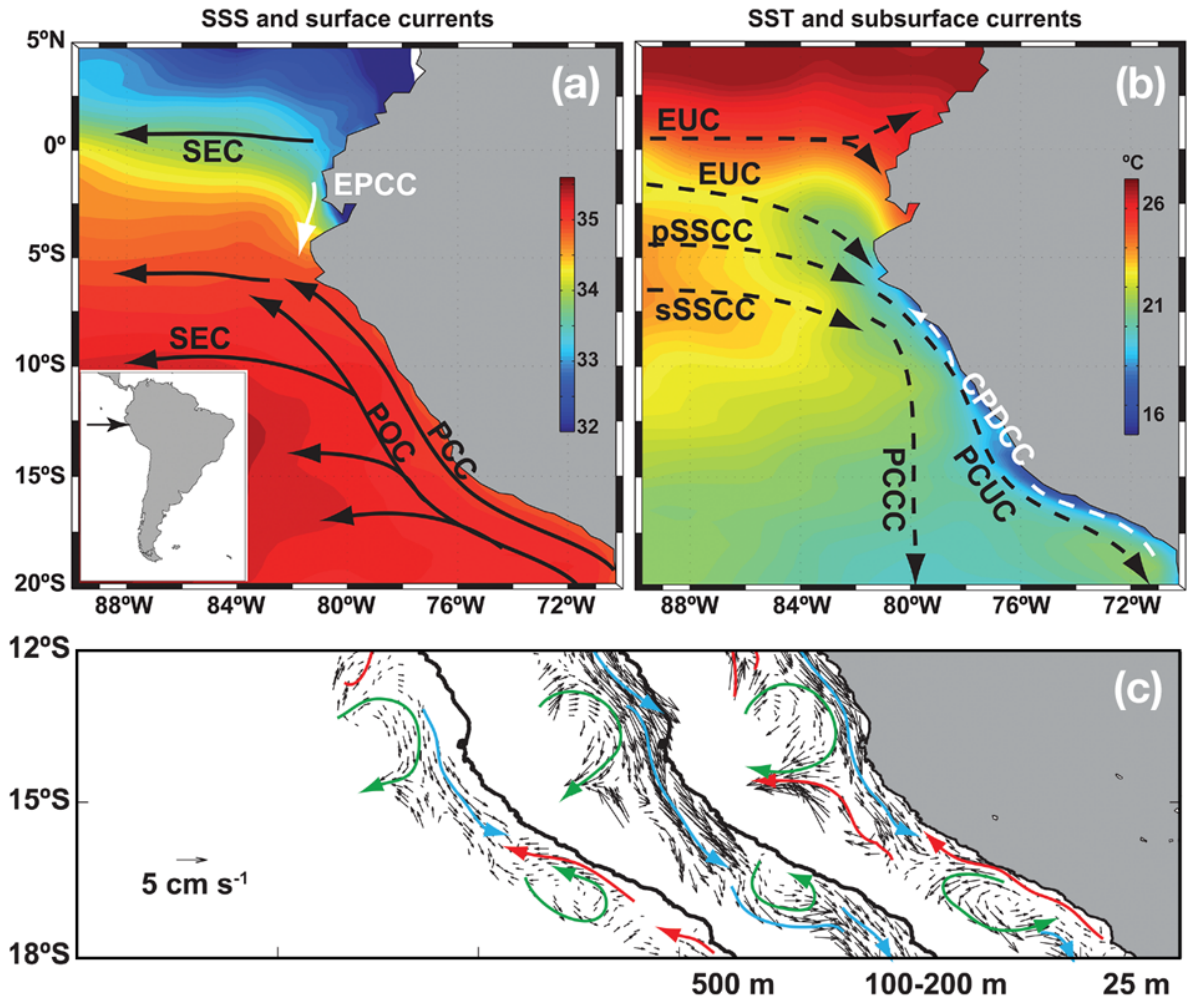


Figure 1: (a) Sea-surface salinity and surface circulation. (b) Sea-surface temperature and subsurface circulation. Relevant currents for this study are the Peru Coastal Current (PCC) at the surface and the Peru-Chile Undercurrent (PCUC) (c) Mean current along the coast of Peru at 25 m, between 100 m and 200 m, and at 500 m depth. Red and blue arrows represent the equatorward and poleward flows. Green arrows indicate mesoscale cyclonic (14°S) and anticyclonic (17°S) features. Figures taken from [Chaigneau et al. \(2013\)](#).

(Fig. 1c).

Mesoscale eddies, upwelling filaments and strong sea-surface temperature (SST) gradients at the upwelling front separating cold coastal from warm offshore waters are ubiquitous features in the PCUS ([Penven et al., 2005](#); [Colas et al., 2012](#); [Thomsen et al., 2016a,b](#)). When the upwelling front meanders and eventually becomes unstable, an ageostrophic secondary circulation develops in order to restore geostrophic balance ([Thomas et al., 2008](#); [Mcwilliams et al., 2009](#); [McWilliams et al., 2015](#)). This ageostrophic flow field can drive large vertical velocities and thus impact the physical-biogeochemical coupling by modifying vertical and lateral transports of nutrients and organic matter ([Lapeyre and Klein, 2006](#); [Lévy et al., 2012](#); [Mahadevan, 2015](#)). Furthermore, frontal processes may provide an effective conduit for vertical fluxes of heat and gas between the subsurface ocean and the atmosphere ([Ferrari, 2011](#); [D'Asaro et al., 2011](#)). While the submesoscale comprises of filaments, fronts, mixed-layer instabilities and symmetric instabilities, we focus here on filaments and fronts which constitute the upper end of the submesoscale variability spectrum with length scales of $\mathcal{O}(1\text{-}10)$ km.

Eddies have in the past been assumed to generally enhance biological productivity by either exposing nutrient-rich subsurface water to the well-lit euphotic zone or by lateral advection of nutrients. They are considered a major source of nutrients to the oligotrophic subtropical gyres, although the magnitude of this supply and the processes involved have been discussed controversially ([Falkowski et al., 1991](#); [Oschlies and Garçon, 1998](#); [Oschlies, 2001, 2002](#); [McGillicuddy et al., 1998, 2003, 2007](#); [Mahadevan et al., 2008](#); [Brannigan, 2016](#)). It has since become clear that the eddy-flux of any tracer strongly depends on the standing stock and its lateral and vertical gradients. In the highly productive EBUS, eddies and filaments have been shown to decrease productivity by exporting nutrients and organic matter offshore and downward below the euphotic zone ([Rossi et al., 2008, 2009](#); [Lévy, 2003](#); [Lathuilière et al., 2010](#); [Gruber et al., 2011](#); [Nagai, 2015](#)) as illustrated in Figure 2.

However, all of these studies are purely based on models and the quantification of submesoscale eddy-fluxes from observations has proven difficult. Submesoscale frontal processes

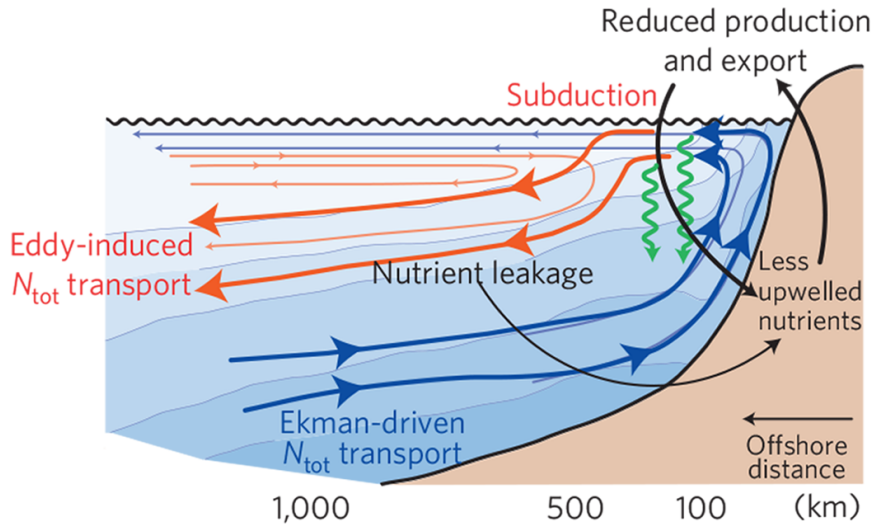


Figure 2: Conceptual diagram of the impact of mesoscale eddies on coastal circulation, nitrogen transport, and organic matter production and export. Figure taken from [Gruber et al. (2011)].

are intermittent and occur on small temporal scales of $\mathcal{O}(\text{days})$ and horizontal scales of $\mathcal{O}(1\text{--}10 \text{ km})$, making them inherently difficult to observe. In order to capture these processes synoptically and separate temporal from spatial variability, towed underway systems ([Pollard and Regier, 1992; Rudnick and Luyten, 1996; Thomas et al., 2013; Hosegood et al., 2017]) or multiplatform adaptive sampling approaches using glider fleets ([Thomsen et al., 2016a]) are increasingly being used for high-resolution hydrographic measurements. Horizontal currents can be measured by vessel-mounted acoustic doppler current profiler (ADCP), but vessel draft and ADCP blanking distance of around 20 m combined often exceed the mixed-layer depth (MLD) and thus do not capture the surface boundary layer where the strongest submesoscale flows are expected. Furthermore, the vertical velocities that characterize frontal processes and determine the associated vertical tracer fluxes can at present not be measured by ADCP at all, a deficit that some studies have overcome using acoustically-tracked neutrally buoyant floats providing Lagrangian estimates of the vertical velocity ([Vélez-Belchí and Tintoré, 2001; D'Asaro et al., 2011]). Satellite images allow for an identification of SST fronts, but satellite altimetry is limited to mesoscale

geostrophic current estimates that do not reveal the complex ageostrophic velocity structure associated with them. Observing submesoscale flows and their temporal variability thus remains challenging and technical as well as practical limitations preclude the quantification of submesoscale eddy-fluxes based on observations alone for the foreseeable future.

Here we conducted an integrated study in an attempt to close the gap between observations and models. We combine targeted shipboard observations of a cold filament and submesoscale-permitting coupled biogeochemical model simulations to address two main questions:

1. How does the observed biogeochemistry of cold filaments off Peru compare with their representation in submesoscale-permitting biogeochemical model simulations?
2. What is the role of filaments for primary production and the export of nutrients and oxygen into the shallow OMZ off Peru?

This thesis is structured as follows: First, an overview of historical measurements in the upwelling near 15°S off Peru is presented (Sec. 2), after which the filament survey that was carried out in this study is described (Sec. 3). A description of the coupled physical-biogeochemical model is given in section 4 along with an assessment of the impact of horizontal resolution on the simulations (Sec. 4.3) and differences between the two biogeochemical models (Sec. 4.4). An observed cold filament is characterized in section 5 and compared with the representation of filaments in biogeochemical model simulations in section 6, followed by a synthesis of observed and modeled filament characteristics that concludes the results (Sec. 6.3). The relevance of our results with respect to the questions above and in the context of the existing literature is discussed in section 7. A summary of this thesis and an outlook on future work and possible improvements of the model simulations is given in section 8.

2 Historical measurements in the upwelling off Peru

The coldest and most persistent upwelling in the PCUS is located near 15°S off Pisco ([Zuta and Urquiza, 1972](#)). Several studies have focused on this persistent upwelling in the past using integrated physical and biogeochemical, shipboard and airborne observations carried out off the coast of Peru during the years 1966, 1969, 1976 and 1977 ([Armstrong et al., 1967](#); [Minas et al., 1974](#); [Walsh et al., 1971](#); [Dagg et al., 1980](#); [Brink et al., 1981](#); [Nelson et al., 1981](#); [Brink, 1983](#); [Boyd and Smith, 1983](#); [Smith, 1983](#); [Packard et al., 1983](#); [Dengler, 1985](#); [Macisaac et al., 1985](#)). Even though these studies were conducted at a time well before satellite measurements and digital communication were ubiquitous, adaptive sampling strategies were implemented with a technical effort that is still impressive 30 - 50 years later. [Macisaac et al. \(1985\)](#) acquired biogeochemical measurements in a lagrangian framework following surface drogues. They planned their measurements according to sea-surface temperature with the support of an aircraft that mapped the area every other day and delivered maps of the previous day's temperature field to the ship by air drop. Underway measurements by autoanalyzer of nitrate, nitrite, ammonium, phosphate and silicate with a horizontal resolution of 250 m were carried out by [Dengler \(1985\)](#).

Cold water plumes extending offshore from the upwelling patch at distinct topographic features of the coastline, with an offshore extent related to the observed wind speed were also described by most of the early studies in underway measurements and infrared images taken by aircraft, features that would some years later be termed upwelling filaments ([Flament and Washburn, 1985](#)). Also consistently described are low phytoplankton concentrations within ~20 km from the coast despite an abundance of nitrate in the recently upwelled water, a feature that is also observed in satellite images during our survey (Fig. 12b). Three factors were proposed over the years to contribute to these high-nutrient, low-chlorophyll (HNLC) conditions in the upwelling center and generally in the eastern tropical Pacific, which will be outlined in the following: (1) A time lag of phytoplankton growth after upwelling ([Armstrong et al., 1967](#); [Boyd and Smith, 1983](#); [Macisaac et al., 1985](#)), (2) grazing pressure by herbivorous zooplankton ([Minas et al., 1974](#); [Walsh, 1976](#); [Whitledge, 1981](#)) and (3) nutrient limitation of phytoplankton growth by a lack of sil-

ica (*Nelson et al.*, 1981) or iron (*Hutchins et al.*, 2002; *Bruland et al.*, 2005). *Macisaac et al.* (1985) investigated the timescale of phytoplankton growth in the upwelling center near 15 °S in a lagrangian framework and found that the time required to complete a full growth cycle of upwelling, increase of nutrient uptake and finally nutrient depletion was 8 - 10 days. The growth cycle in their study is completed in the near-shore upwelling and maximum nutrient uptake already occurs at 10 km from the coast, indicating that the phytoplankton growth timescale cannot explain HNLC conditions further offshore. However, the trajectories of their drogues show a large along-shore component of the flow, suggesting that the HNLC area that is influenced by the phytoplankton growth timescale may be larger in conditions where a stronger offshore flow is present. *Minas et al.* (1974) first suggested that grazing by herbivorous zooplankton immediately after upwelling keeps the phytoplankton concentrations low, thereby slowing down the initial phytoplankton growth and reducing nutrient uptake which is an effective way to spread upwelled nutrients to the open ocean. The slowly growing phytoplankton standing stock observed in the PCUS was explained by a higher abundance of zooplankton in the euphotic zone due to the suboxic waters below and thus higher grazing pressure. This grazing hypothesis (*Walsh*, 1976) was the generally accepted explanation for the occurrence of HNLC conditions until it was discovered that a lack of iron can limit phytoplankton growth in the PCUS upwelling system (*Hutchins et al.*, 2002; *Bruland et al.*, 2005). Given the many possible explanations for HNLC conditions, *Pennington et al.* (2006) in their review of primary production in the Pacific arrive at the conclusion that not a single but multiple interdependent processes - mainly iron limitation and grazing - are likely responsible for the observed low Chl α concentrations. A possible interaction between different processes would be that iron limitation favors small phytoplankton which may be more susceptible to zooplankton grazing pressure which then limits the growth rate. A recent modeling study by *Vergara et al.* (2017) revisited the question of nutrient limitation of phytoplankton growth in the PCUS and found that iron is the limiting nutrient in winter and a co-limitation of silica and nitrate exists in summer. *Dengler* (1985) found both nitrate and silica to be above limiting levels in the PCUS during a survey in April - June 1976.

This brief literature review shows that HNLC conditions are ubiquitous in the PCUS and that the generating mechanisms are - although complex and still not fully understood - likely a combination of multiple interdependent biogeochemical processes. Furthermore, the timescale of phytoplankton growth following upwelling can be expected to impact the amount of nitrate and carbon that is subducted by filaments. Given a slowly growing phytoplankton standing stock, upwelled nutrients can be subducted below the euphotic zone before they are taken up by phytoplankton. It is therefore crucial that biogeochemical models represent these processes in order to obtain realistic near-surface distributions of nutrients and organic matter.

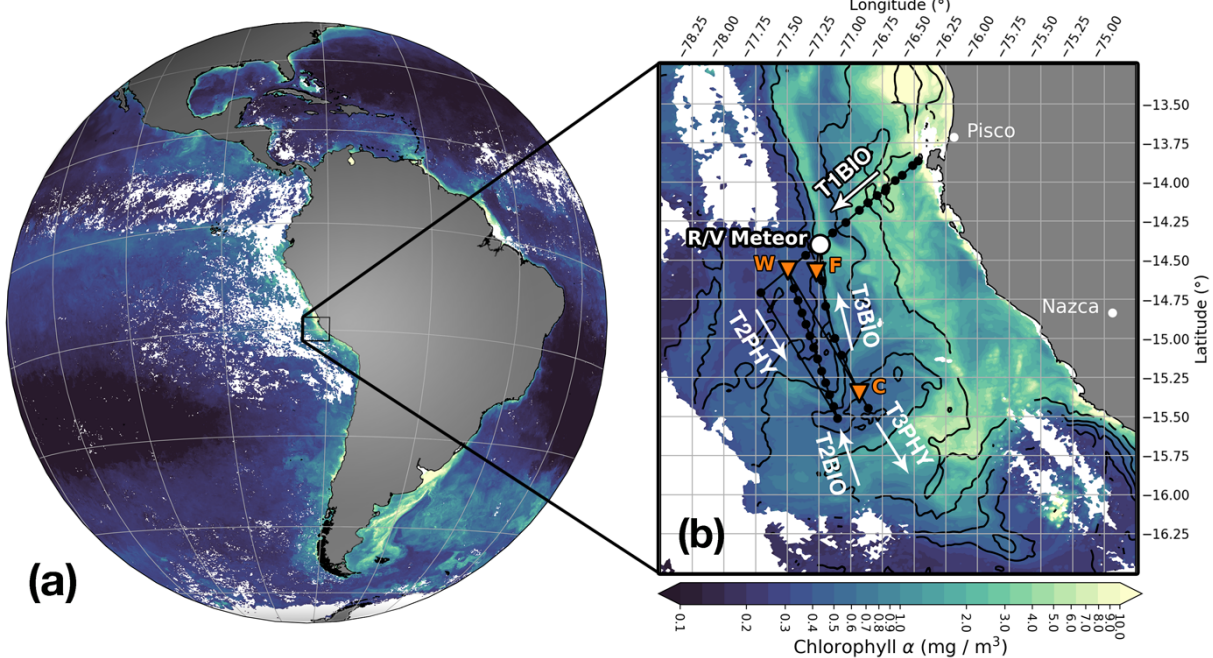


Figure 3: Surface chlorophyll α measured from satellite (a) in April 2017 (monthly composite) and (b) on April 14, 2017 at 18:25 UTC with the position of *R/V Meteor* and names of transects superimposed. Black lines with black circles mark the track of the filament survey with CTD stations and orange triangles indicate CTD stations where primary production was measured. Black contours represent the 20.98°C , 22.15°C , 23.1°C , and 24°C isotherms of smoothed (2.5 km gaussian window) satellite sea-surface temperature, white areas indicate missing data due to cloud cover.

3 Filament survey

Observing the biogeochemistry of coastal upwelling regions is challenging due to the inherent intermittency of multi-scale physical processes like eddies, filaments and fronts that interact with the biogeochemical cycles. A survey designed to investigate the biophysical coupling at a cold filament near 14°S off the coast of Peru was carried out on April 12-17, 2017 using an adaptive sampling strategy guided by real-time satellite images. The field work was conducted during *R/V Meteor* cruise M136 which started on April 11 and ended on April 29, 2017 in Callao, Peru and carried out as part of the "SFB754 - Climate-Biogeochemistry Interactions in the Tropical Ocean" project. The cruise track

during the survey consisted of five transects (Fig. 3b). The first transect (T1BIO) mapped the upwelling region in cross-shore direction with conductivity, temperature and depth (CTD) measurements including biogeochemical parameters (O_2 , NO_3^- , NO_2^- , NH_4^+) determined from water samples. On subsequent along-shore transects, a cold filament present ~ 100 km southeast of transect T1BIO was crossed by *R/V Meteor* four times in a zigzag pattern: Twice with high-resolution physical underway CTD measurements heading in southeast direction (T2PHY, T3PHY; Fig. 15) and two more times with station-based lowered CTD measurements including biogeochemical parameters heading in northwest direction (T2BIO, T3BIO; Fig. 14, 17). A dense sampling strategy with 8 - 10 km horizontal spacing between stations and 5 - 10 m vertical spacing between samples was applied for the biogeochemical transects. The physical underway transects were completed in under 8 hours and thus closely represent a synoptic view of the surface ocean.

3.1 Hydrographic and meteorological measurements

Hydrographic data was obtained from lowered conductivity, temperature and pressure (CTD) measurements using SeaBird SBE 9-plus CTD system equipped with two sets of pumped sensors. Water samples for oxygen, nutrients and salinity were taken using 24 Niskin bottles (10 l) mounted on a General Oceanics rosette. Salinity samples were analyzed on board with a Guildline Autosal 8 model 8400B salinometer to calibrate conductivity measurements to practical salinity (PSS-78) with an uncertainty of 0.003 g kg^{-1} . Practical salinity was converted to absolute salinity (TEOS-10) using routines of the Gibbs Seawater toolbox (<https://github.com/TEOS-10/GSW-Python>). The CTD was also equipped with an oxygen sensor and a WET Labs (USA) fluorometer. The oxygen sensor was calibrated to an accuracy of $1.5 \mu\text{mol}$ using Winkler titration. Because Winkler titration is not reliable in the core of the OMZ and results in too high values (*Thomsen et al.*, 2016b), a concentration of $0 \mu\text{mol l}^{-1}$ was assumed and the profiles corrected accordingly. As the Chl α concentrations determined from water samples were not significantly different from those measured by the fluorometer, the original factory calibration provided by the sensor manufacturer WET Labs (USA) was used. For more

details on calibration of Chl α fluorescence measurements, the reader is referred to [Loganova et al. \(2016\)](#). Underway subsurface temperature and salinity were measured using a Teledyne Oceanscience (Poway, USA) RapidCAST system acquiring profiles of the upper 70 m of the water column every 2 minutes resulting in a horizontal resolution of 500-900m depending on the vessel speed. Subsurface current velocities on *R/V Meteor* were recorded by a vessel-mounted acoustic Doppler current profiler (vmADCP). The system used was a Teledyne RD Instruments OceanSurveyor 75kHz ADCP capable of reaching a maximum depth of \sim 700m. The shallowest velocity measurements were acquired in a bin centered 18 m below the sea-surface. On transects T2PHY and T3PHY the vessel speed was kept nearly constant at \sim 5 m s $^{-1}$ to obtain high-quality velocity measurements (Fig. [15g,h](#)). Wind speed and direction on *R/V Meteor* were measured at 35.5 m height with a temporal resolution of one minute.

3.2 Biogeochemical measurements

Nutrient concentrations were determined onboard the ship by a QuAAstro autoanalyzer (SEAL Analytical, Southampton, UK) using standard photometric methods ([Grasshoff et al., 1983](#)). Primary production rates were measured by incubation from water samples taken at three CTD stations (orange triangles in Fig. [12](#)) and three depths per station (Fig. [14c](#); [18c](#)). Samples were taken in quadruplicate into 4.5 l polycarbonate bottles and subsequently in one of three incubators with continuously flowing surface sea water between -4/+10°C of the *in-situ* temperature shaded to 20% , 10% and 1% surface irradiance (Lee Filters, Seattle, WA, USA) depending only on the sampling depth and not on the *in-situ* photosynthetically available radiation (PAR). The samples were incubated for a total of 48 hours. After 24 hours of incubation, three bottles were amended with ^{13}C labeled bicarbonate solution ($\text{H}^{13}\text{CO}_3^-$) while one bottle was amended with unlabeled bicarbonate solution and air to determine background natural abundance of ^{13}C . After another 24 hours of incubation, the samples were filtered, dried and pelletized. Particulate organic C and the relative abundance of ^{13}C was then determined through continuous

flow isotope ratio mass spectrometry coupled to an elemental analyzer. For a more detailed description of the sample processing and the equations used to calculate the carbon fixation rate from the relative abundance of ^{13}C , the reader is referred to [Krupke et al. \(2015\)](#).

3.3 Satellite measurements

To guide the shipboard measurements and put them into a regional context MODIS (Moderate Resolution Imaging Spectroradiometer) Level 2 along-track sea-surface temperature (SST) and chlorophyll a (Chl α) products with an approximate resolution of 1 km from the TERRA and AQUA satellites were used (<https://oceandata.sci.gsfc.nasa.gov/>). We restricted our analysis to daylight images of SST and used the cloud mask based on ocean color because of obvious deficiencies of the cloud mask based on infrared SST data alone. In addition, the April 2017 composite of Chl α images was downloaded from NASA (<https://neo.sci.gsfc.nasa.gov>). SST data from AVHRR (Advanced Very High Resolution Radiometer) at 25 km resolution was downloaded from NOAA (<ftp://eclipse.ncdc.noaa.gov/pub/OI-daily-v2/NetCDF/>). To relate the shipboard current velocity measurements to the synoptic mesoscale circulation during the cruise, geostrophic surface velocities derived from satellite altimetry processed by the SL-TAC multission altimeter data processing system ([SEALEVEL_GLO_PHY_L4_NRT_OBSERVATIONS_008_046](#)) were downloaded from CMEMS (Copernicus Marine Environment Monitoring Service, <http://marine.copernicus.eu>). Primary production estimates based on the VGPM model ([Behrenfeld and Falkowski, 1997](#)) and Chl α measurements from the VIIRS satellite at weekly resolution were downloaded from the Oregon State University Ocean Productivity website (<http://www.science.oregonstate.edu/ocean.productivity/>).

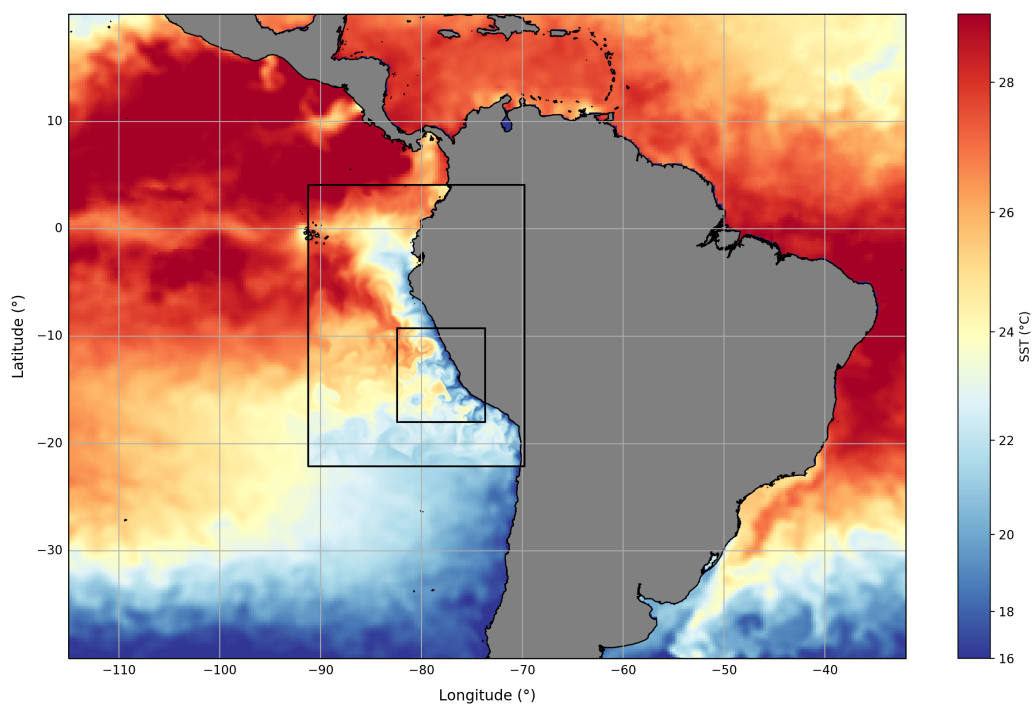


Figure 4: Modeled sea-surface temperature (SST) on April 14, 2017 in the coarse- ($1/9^\circ$) and high-resolution ($1/45^\circ$) simulations superimposed on AVHRR satellite SST. Black rectangles indicate model domains of the coarse- and high-resolution nests.

4 Coupled Physical-Biogeochemical Model

4.1 Physical model

ROMS (Regional Oceanic Modeling System) is a free-surface, terrain-following coordinate model that solves the Primitive Equations using the Boussinesq approximation and a hydrostatic vertical momentum balance. A detailed description including the numerical schemes is given in [Shchepetkin and Mcwilliams \(2004\)](#). The model was configured as a nested set of two spatial domains using an offline, one-way embedding procedure (Fig. 4). The outer domain has a resolution $1/9^\circ$ over a region of 2207 km in zonal direction by 2911 km in meridional direction ($24.4^\circ \times 26.2^\circ$), and the inner domain has a resolution of $1/45^\circ$ over a region of 918 km in zonal direction by 973 km in meridional direction ($8.69^\circ \times 8.76^\circ$). There are 32 vertical sigma-levels, the resolution varies with water depth and amounts at the surface to 1-2 m on the shelf and 5 m offshore. The model topography was derived from the GEBCO (General Bathymetric Chart of the Oceans, <http://www.gebco.net>) product, interpolated onto the model grid and smoothed to reduce pressure gradient errors. The lateral open boundary conditions of the outer domain for temperature, salinity, velocities and sea-level were provided at $1/12^\circ$ resolution by the MERCATOR model (<https://www.mercator-ocean.fr>) which assimilated in-situ data transmitted from *R/V Meteor* during cruise M136, as well as satellite SST and sea-level measurements. The open boundary conditions for oxygen, nitrate, phosphate and silicate were provided at $1/2^\circ$ resolution by the *CARS* (CSIRO Atlas of Regional Seas) climatology ([Ridgway et al., 2002](#)); for dissolved inorganic carbon (DIC), dissolved organic carbon (DOC) and iron, model output from a global $2^\circ \times 2^\circ$ NEMO-PISCES simulation was used ([Aumont et al., 2015b](#)). The model was forced with surface wind stress derived from the daily level-2 wind product provided by the ASCAT scatterometer flying on the MetOp-B satellite (<https://podaac.jpl.nasa.gov/dataset/ASCATB-L2-25km>). The net surface heat flux Q is given by the *COADS* ([Worley et al., 2005](#)) climatology relaxed to *AVHRR* (Advanced Very High Resolution Radiometer; <ftp://eclipse.ncdc.noaa.gov/pub/OI-daily-v2/NetCDF/>) daily SST according to

$$Q = Q_{\text{COADS}} - \frac{dQ}{dT} \cdot (\text{SST}_{\text{ROMS}} - \text{SST}_{\text{AVHRR}}) \quad (1)$$

where $\frac{dQ}{dT}$ represents the additional heat flux that is imposed per degree of temperature difference between model SST and observed SST.

After a spinup of 14 years for the $1/9^\circ$ simulation with *PISCES* biogeochemistry, the $1/9^\circ$ simulation with *BioEBUS* biogeochemistry and both $1/45^\circ$ simulations were started from this model state and run from January 2013 until April 2017.

4.2 Biogeochemical models

The concentration of a tracer C_i in *ROMS* is given by

$$\frac{\partial C_i}{\partial t} = -\nabla \cdot (uC_i) + K_h \nabla^2 C_i + \frac{\partial}{\partial z} (K_z \frac{\partial C_i}{\partial z}) + BIO(C_i) \quad (2)$$

with terms on the right-hand side representing (1) advection (2) horizontal diffusion (3) vertical mixing and (4) a residual caused by biogeochemical processes.

The biogeochemical models that *ROMS* was coupled to in our different simulations were *PISCES* and *BioEBUS*, both of which will be described in the following. The configuration of the physical model was identical with two exceptions: (1) The lateral tracer mixing acted on isopycnal surfaces (TS_MIX_ISO) in the PISCES simulations and on geopotential surfaces (TS_MIX_GEO) in the BioEBUS simulations. (2) A newer version of the surface boundary layer mixing parameterization (LMD_SKPP2005) was used in the BioEBUS simulations than in the PISCES simulations. While no rigorous testing on the effects of these differences has been done, the seasonal cycle of the average mixed-layer depth was similar in all simulations and we assume effects to be small. The mesoscale variability (i.e. the position of mesoscale eddies) was different in the PISCES and BioEBUS simulations, which may also be related to the choice of parameterizations. However, in the turbulent mesoscale regime large differences resulting from small perturbations such as those generated by numerical errors are generally expected. The differences between simulations that were run on separate machines can thus likely be attributed to these

numerical differences.

The *PISCES* (Pelagic Interaction Scheme for Carbon and Ecosystem Studies) model simulates the biogeochemical cycles of carbon and the main nutrients (P, N, Si, Fe). It includes two phytoplankton compartments (nanophytoplankton and diatoms), two zooplankton size classes (microzooplankton and mesozooplankton), two detritus classes termed small particulate organic carbon (1 - 100 μm , POC) and big particulate organic carbon (100 - 5000 μm , GOC) and a description of the carbonate chemistry. The sinking velocities for the detritus classes are constant for POC (3 m d^{-1}) and increasing from a minimum value (50 m d^{-1}) at the surface to a maximum value (200 m d^{-1}) at 5000 meters depth for GOC. In our configuration, *PISCES* is not coupled to a sediment model which could act as a reservoir for POC and DOC. Particles that reach the bottom are immediately converted to dissolved organic carbon (DOC) and subsequently remineralized. A detailed model description is given in [Aumont et al. \(2015b\)](#).

The *BioEBUS* (Biogeochemical model for the Eastern Boundary Upwelling Systems) model is nitrogen-based and includes nitrate, nitrite and ammonium as prognostic variables. The complex nitrogen cycle allows nitrification, denitrification and annamox, which are important processes in oxygen minimum zones ([Kalvelage et al., 2013](#)) to be explicitly represented. However, the model lacks the nutrients phosphate, silicate and iron which are present in *PISCES*. Similar to *PISCES*, *BioEBUS* includes two phytoplankton compartments (nanophytoplankton and diatoms), two zooplankton size classes (microzooplankton and mesozooplankton) and two types of detritus (POC and GOC). The sinking velocities for the detritus classes are constant at 1 m d^{-1} (POC) and 40 m d^{-1} (GOC) respectively. *BioEBUS* includes a sediment model and a cumulative layer exists at the sediment-water interface where sinking particles are stored without further interaction with the water column. A detailed model description is given in [Gutknecht et al. \(2013\)](#).

Both biogeochemical models have in common that they use two compartments each for

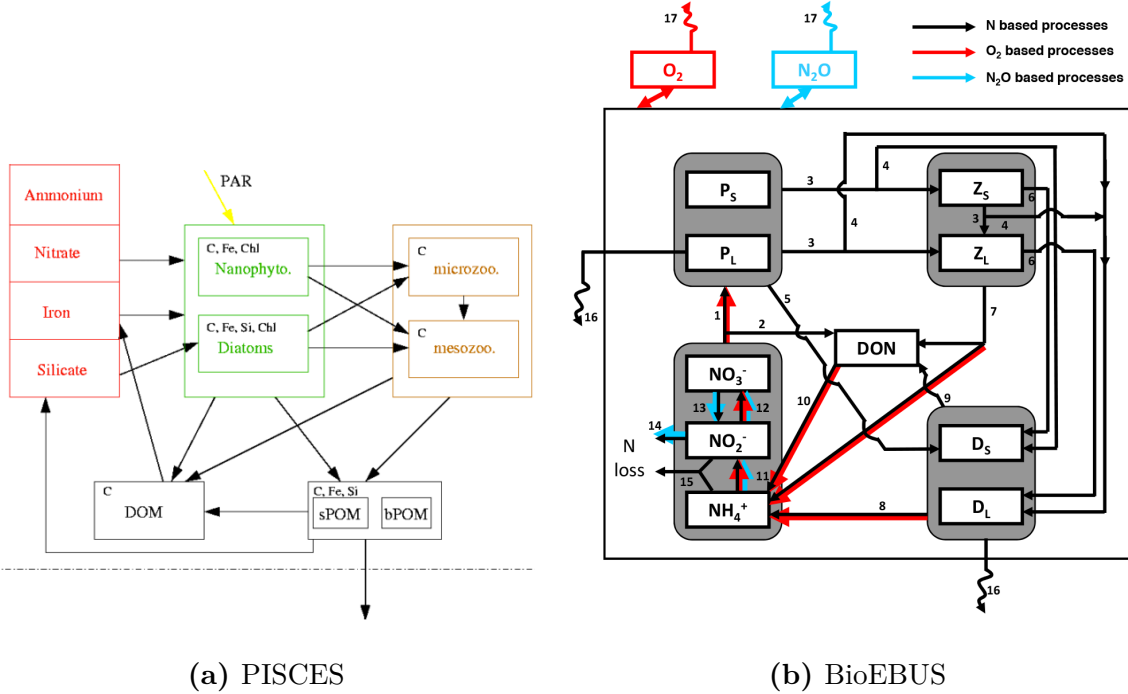


Figure 5: Diagrams showing prognostic variables and processes of the (a) *PISCES* and (b) *BioEBUS* models. Only the ecosystem model is shown in (a), thus omitting oxygen and the carbonate system. Figures are taken from (a) Aumont *et al.* (2015b) and (b) Gutknecht *et al.* (2013), respectively.

the representation of phytoplankton, zooplankton and detritus. The main advantages of each model are a more complex nitrogen cycle and a sediment model in *BioEBUS* and the explicit representation of phosphate, silicate, iron and carbonate chemistry in *PISCES*.

4.3 Impact of increased horizontal resolution

Two simulations at coarse ($1/9^\circ$) and high ($1/45^\circ$) horizontal resolution with the same 32 vertical levels were run with each of the two biogeochemical models. To assess the effect of increased horizontal resolution, we interpolated the high-resolution simulations on the coarse-resolution grid and analyzed the difference. Mesoscale eddies dominate the differences between the BioEBUS and PISCES simulations on timescales of several months. We identified 2 years as a useful averaging period to compare simulations that exhibit substantial differences on the mesoscale. Because the BioEBUS simulations were

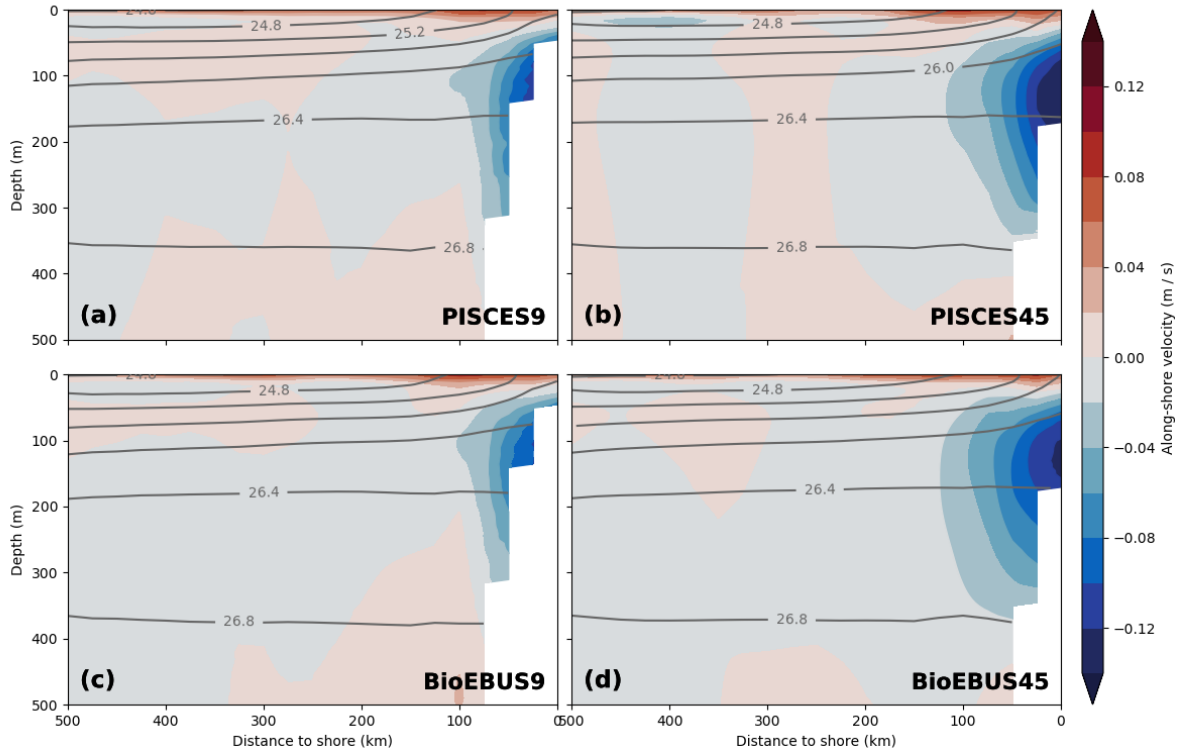


Figure 6: Along-shore currents in the (a) PISCES9 (c) BioEBUS9 (b) PISCES45 and (d) BioEBUS45 simulations, averaged on depth levels in along-shore direction with 25 km cross-shore bins in a coastal band of 500 km width between 10.5 °S and 17.5 °S over the period 2015 - 2016.

only started in 2013 from the PISCES9 initial conditions, the first two years were not used and all following analysis is based on averages over the period 2015 - 2016, assuming a sufficient adjustment of the relatively fast near-surface biogeochemistry by this time.

The mean kinetic energy (MKE) increased between the coarse- and high-resolution simulations especially near the coast (not shown), which manifests most notably as an increase in the mean along-shore currents (Fig. 6). The poleward undercurrent that is seen near the shelf break at ~100 m depth extends ~20 km further offshore and is $\sim 4 \text{ cm s}^{-1}$ stronger in its core in the 1/45° compared with the 1/9° simulations. This result is consistently found in both sets of simulations (PISCES & BioEBUS) and the stronger undercurrent is closer to observed values of $10 - 15 \text{ cm s}^{-1}$ ([Chaigneau et al., 2013](#)). No substantial

changes in the cross-shore circulation are discernible (not shown). Two factors are likely responsible for the changes in strength and shape of the poleward undercurrent in our simulations: Firstly, the smoothing of the model topography can be reduced at higher resolution, leading to a steeper shelf break. Secondly, numerical diffusion is reduced at higher resolution i.e. previously subgrid-scale processes are explicitly resolved and contribute to the average kinetic energy. In addition to the mean circulation, the eddy kinetic energy (EKE) increased in the $1/45^\circ$ compared with the $1/9^\circ$ simulations as apparent in surface EKE fields (Fig. 7). The change in EKE between the coarse- and high-resolution simulations is positive almost everywhere, small areas of negative EKE change are only found in the BioEBUS45 simulation north of 12°S and in the PISCES45 simulation in the southeast corner of the model domain. The strongest absolute change is seen in a coastal band 100 km in width with a maximum near Pisco ($2 \cdot 10^{-3} \text{ m}^2 \text{s}^{-2}$). The EKE increase in the BioEBUS simulations ($1 \cdot 10^{-3} \text{ m}^2 \text{s}^{-2}$) is smaller than in the PISCES simulations ($2 \cdot 10^{-3} \text{ m}^2 \text{s}^{-2}$) and the highest EKE values occur in different locations, at 14.5°S in PISCES and near the coast at 17°S in BioEBUS. In contrast, the largest *relative* changes are found between 100-200 km offshore where low EKE ($< 2 \cdot 10^{-4} \text{ m}^2 \text{s}^{-2}$) is found in the coarse-resolution simulations and range from -75 % to 500 % locally. Averaged over the model domain an increase in surface EKE by 89% and 113% is observed in the PISCES and BioEBUS simulations, respectively. A band of $\sim 200\%$ EKE increase around 12°S in the PISCES simulations (Fig. 7c) coincides with a persistent filament that formed there repeatedly (not shown). The increases in MKE (not shown) and EKE (Fig. 7) around 12°S could be related to a topographic bend in the coastline that favors the generation of filaments in this area in the high-resolution simulations but is not present due to smoothed topography in the coarse-resolution simulations. EKE of $> 1.2 \cdot 10^{-3} \text{ m}^2 \text{s}^{-2}$ is not found north of 13°S in the BioEBUS45 simulation, which is where the strongest EKE increase occurred in the PISCES45 simulation, the reason of which remains unclear. In general, the PISCES and BioEBUS simulations agree qualitatively on the result of increased EKE in the high-resolution simulations, but magnitude and locations of these changes exhibit considerable differences. Although only the changes in surface EKE are described here,

similar changes in EKE were found at the subsurface (not shown).

Consistent vertical patterns of relative changes in the biogeochemical fields emerge when we subtract average cross-shore sections of the coarse-resolution simulations from the corresponding sections in the high-resolution simulations (Fig. 8). Note that in contrast to Figure 7, only the changes in the mean fields and not the mean fields themselves are shown. The effect on the distribution of oxygen and nitrate is greatest around the $\sigma_\theta = 25.6 \text{ kg m}^{-3}$ isopycnal that approximately coincides with the $10 \mu\text{mol l}^{-1} \text{NO}_3^-$ nutricline (not shown), where an O_2 increase by $\sim 20 \mu\text{mol l}^{-1}$ and a nitrate decrease by $2.5 \mu\text{mol l}^{-1}$ is observed. An area of negative change in oxygen ($-15 \mu\text{mol l}^{-1}$) with a vertical extent of $\sim 100 \text{ m}$ is found slightly deeper around the 26 kg m^{-3} isopycnal at 350 - 500 km offshore. An O_2 increase ($+5 \mu\text{mol l}^{-1}$) and NO_3^- decrease ($-0.75 \mu\text{mol l}^{-1}$) is found 100 m below the pycnocline within 300 km from the coast. Between 200 - 300 m changes in O_2 are positive but small ($< 2.5 \mu\text{mol l}^{-1}$) while changes in NO_3^- are negative ($-0.75 \mu\text{mol l}^{-1}$) in BioEBUS but inconclusive in PISCES. At first glance, considerable differences in the NO_3^- changes from coarse to high resolution seem to exist between the PISCES and BioEBUS simulations: While both positive and negative NO_3^- changes are visible in PISCES, negative changes dominate in the BioEBUS simulations (Fig. 8e,f). On closer inspection the patterns of NO_3^- change appear very similar in PISCES and BioEBUS but exhibit an offset of $\sim 1.5 \mu\text{mol l}^{-1}$, which could be related to differences in the mean NO_3^- fields between the two biogeochemical models (Fig. 10e,f). The pattern correlation between the opposing O_2 and NO_3^- changes around the nutricline is therefore high. An increase in $\text{Chl}\alpha$ concentration ($+ 0.3 \text{ mg m}^{-3}$) centered around the nutricline coincides with the changes in O_2 and NO_3^- described above. A surface $\text{Chl}\alpha$ decrease of $\sim 0.6 \text{ mg m}^{-3}$ in PISCES and $\sim 0.3 \text{ mg m}^{-3}$ in BioEBUS is apparent, which coincides with a NO_3^- increase ($+1 \mu\text{mol l}^{-1}$) in PISCES but a NO_3^- decrease ($-0.5 \mu\text{mol l}^{-1}$) in BioEBUS. $\text{Chl}\alpha$ changes below $\sim 100 \text{ m}$ are negligible ($< 0.05 \text{ mg m}^{-3}$) due to low mean $\text{Chl}\alpha$ concentrations at these depths (not shown).

In order to identify horizontal patterns associated with the O_2 and NO_3^- changes described above (Fig. 8a,b,e,f) their average distributions at 75 m depth are investigated (Fig. 9a-l).

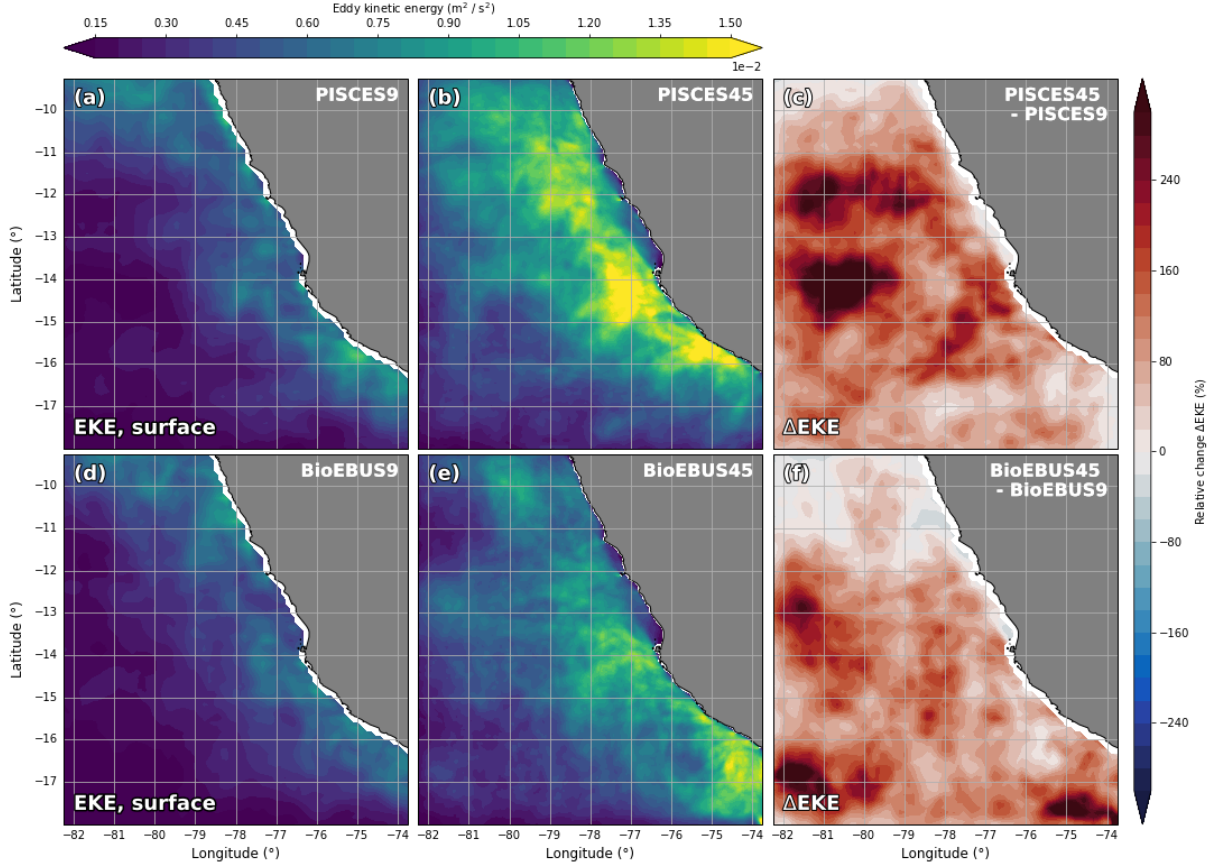


Figure 7: Surface eddy kinetic energy for the (a) PISCES9 (d) BioEBUS9 (b) PISCES45 and (e) BioEBUS45 simulations, averaged over the period 2015-2016. Panels (c,f) show the relative change in EKE with increased resolution calculated as $\Delta\text{EKE} = \text{EKE}_{1/45^\circ} - \text{EKE}_{1/9^\circ}$ for the (c) PISCES and (f) BioEBUS simulations. The velocity fields were interpolated at the given depths using ROMSTOOLS ([Penven et al., 2007](#)) functions translated from the original Matlab code into the Python programming language (<https://github.com/jaard/romstools-visual>). Eddy velocities were calculated using a Reynolds decomposition with $u' = u - \langle u \rangle_{30\text{d}}$ and $v' = v - \langle v \rangle_{30\text{d}}$, where u and v are the daily (PISCES) / 3-day (BioEBUS) average zonal and meridional velocity components, respectively and $\langle \cdot \rangle_{30\text{d}}$ denotes a 30-day moving average. The eddy kinetic energy per unit mass is then given by $\text{EKE} = \frac{1}{2} \cdot (u'^2 + v'^2)$.

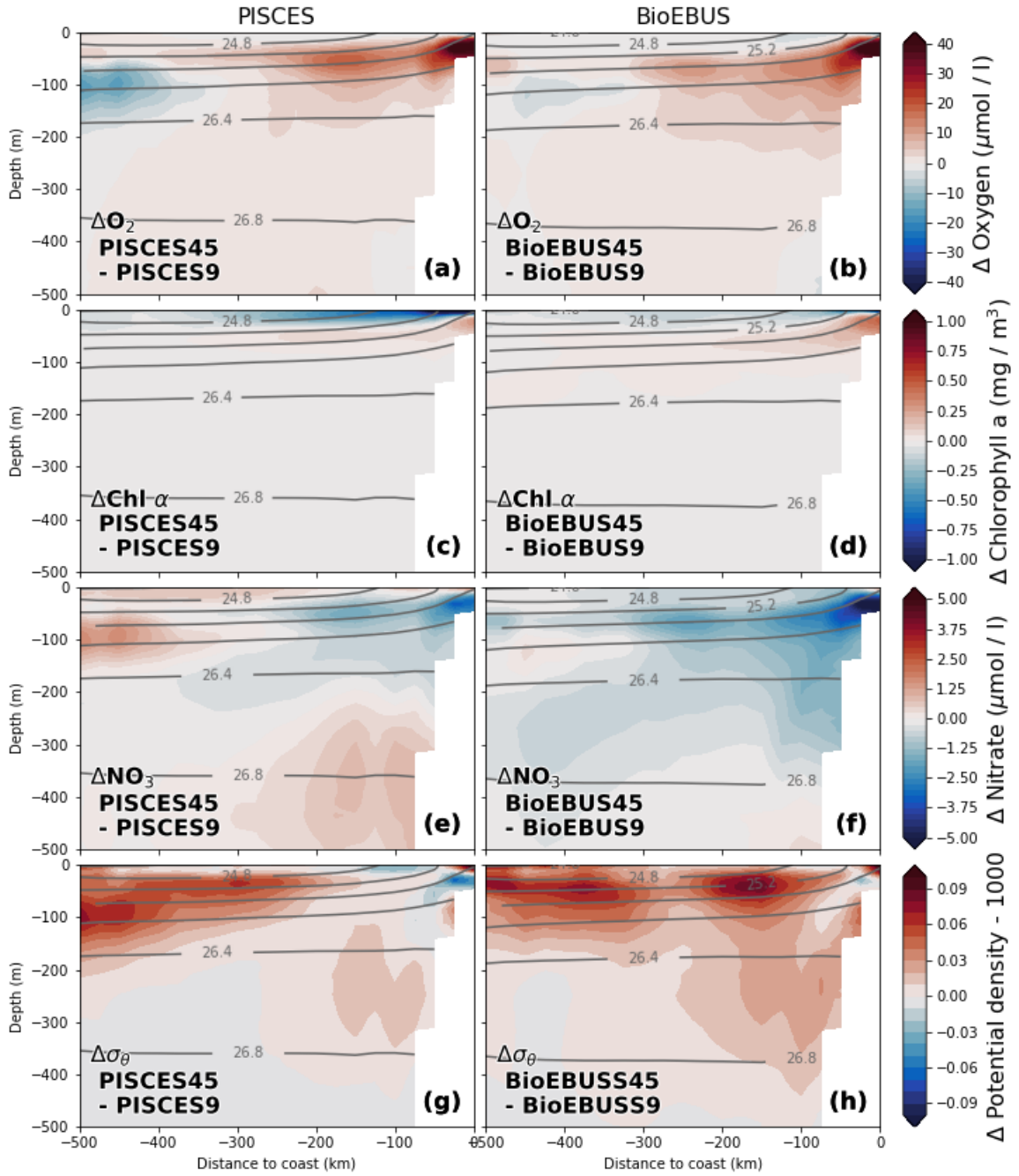


Figure 8: Relative changes in (a,b) Oxygen (c,d) Chlorophyll a and (e,f) Nitrate between the $1/9^\circ$ and $1/45^\circ$ simulations calculated as (a,c,e) $\Delta_{PISCES} = PISCES45 - PISCES9$ and (b,d,f) $\Delta_{BioEBUS} = BioEBUS45 - BioEBUS9$, respectively. All fields were averaged on depth levels in along-shore direction with 25 km cross-shore bins in a coastal band of 500 km width between $10.5^\circ S$ and $17.5^\circ S$ over the period 2015-2016. Grey lines represent potential density averaged over BioEBUS9 / BioEBUS45 and PISCES9 / PISCES45, respectively.

An oxygen increase ($+35 \mu\text{mol l}^{-1}$) is apparent at 14°S about 50 km offshore and at 16°S within 20 km from the coast (Fig. 9c,f) in both PISCES and BioEBUS simulations. In precisely the same locations a nitrate decrease in PISCES ($-3 \mu\text{mol l}^{-1}$) and BioEBUS ($-5 \mu\text{mol l}^{-1}$) is found (Fig. 9i,l). A decrease in oxygen ($-35 \mu\text{mol l}^{-1}$) occurs ~ 200 km offshore at 14°S in PISCES and ~ 100 km offshore near 17°S in BioEBUS. Again, nitrate changes of opposing sign ($+5 \mu\text{mol l}^{-1}$ PISCES / $+4 \mu\text{mol l}^{-1}$ BioEBUS) are present in the same locations. Thus, the changes in NO_3^- and O_2 at 75 m depth show a very high spatial correlation similar to the vertical sections and exhibit a ratio of approximately 8:1.

Summarizing, an increased horizontal resolution from $1/9^\circ$ to $1/45^\circ$ leads to an average increase in eddy kinetic energy by about a factor of 2 in our simulations. While the PISCES and BioEBUS simulations agree qualitatively on this result, they differ in the magnitude of the increase. Mean kinetic energy likewise increases, manifesting as an increase in velocity of the poleward undercurrent by 30% which is closer to observations. An increase in the cross-sectional area of the undercurrent seems to be related to changes in the model topography. The effect of horizontal resolution on the biogeochemical fields is greatest around the nutricline within 250 km from the coast, where an oxygen increase by $+20 \mu\text{mol l}^{-1}$, a nitrate decrease by $-2.5 \mu\text{mol l}^{-1}$ and a $\text{Chl}\alpha$ increase by $+0.3 \text{ mg m}^{-3}$ are present. High vertical and horizontal pattern correlation of the opposing changes in O_2 and NO_3^- is seen in the simulations with the $\Delta\text{O}_2 : \Delta\text{NO}_3^-$ ratio between these changes being approximately 8:1. While an offset exists between PISCES and BioEBUS especially for NO_3^- , the characteristic patterns of the changes in average vertical sections and horizontal fields are remarkably similar for the PISCES and BioEBUS, suggesting independence of the biogeochemical model used and thus encouraging some confidence in the robustness of the results.

4.4 Impact of biogeochemical model choice

The same method as above is applied to quantify the differences between the PISCES and BioEBUS biogeochemical models at both $1/9^\circ$ and $1/45^\circ$ horizontal resolution. Similarly,

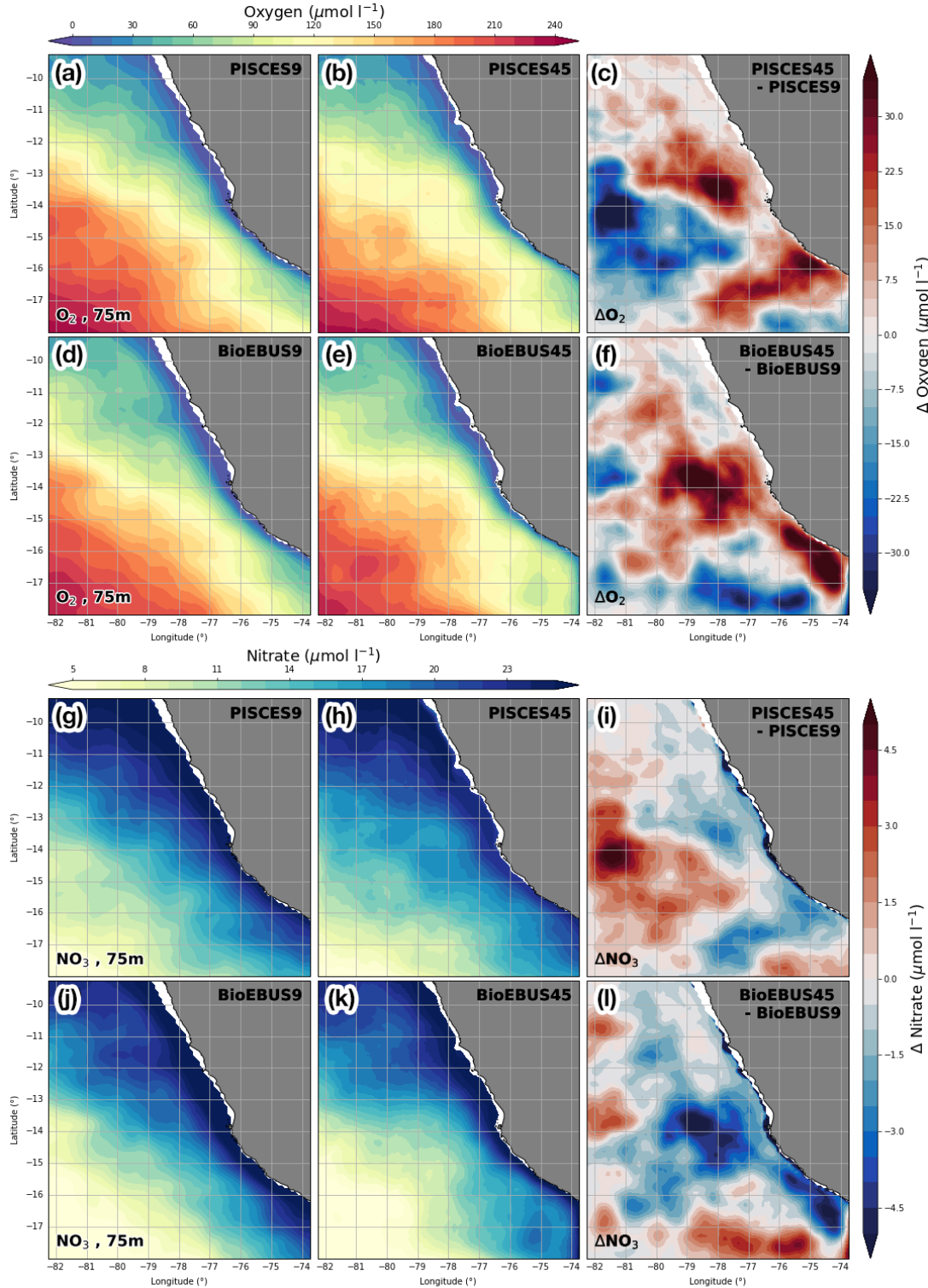


Figure 9: (a,b,d,e) Oxygen and (g,h,j,k) nitrate at 75 m depth averaged over the period 2015–2016 and their relative changes between the $1/9^\circ$ and $1/45^\circ$ simulations calculated as (c,i) $\Delta\text{PISCES} = \text{PISCES45} - \text{PISCES9}$ and (f,k) $\Delta\text{BioEBUS} = \text{BioEBUS45} - \text{BioEBUS9}$, respectively.

consistent vertical patterns of relative changes in the biogeochemical fields emerge when average cross-shore sections of the PISCES simulations are subtracted from the corresponding sections in the BioEBUS simulations, which can be understood as the effect of choosing BioEBUS over PISCES.

The choice of a particular biogeochemical model can have a similarly strong impact on the average cross-shore distributions of oxygen, chlorophyll α and nitrate as horizontal resolution (Fig. 10). A positive difference in oxygen ($+20 \mu\text{mol l}^{-1}$) between BioEBUS and PISCES, centered around the $\sigma_\theta = 25.6 \text{ kg m}^{-3}$ isopycnal is present within 100 km and 250 km from the coast in the coarse- and high-resolution simulations, respectively (Fig. 10a,b). O₂ concentrations in the oxygen minimum zone below 300 m depth are $2-5 \mu\text{mol l}^{-1}$ lower in BioEBUS than in PISCES, with largest difference of $5 \mu\text{mol l}^{-1}$ occurring at 500 m depth near the shelf. On average, positive and negative differences in O₂ approximately compensate each other. The difference in Chl α between the two biogeochemical models exhibits a horizontal dipole pattern with high ($+0.75 \text{ mg m}^{-3}$) values within 50 km from the coast, indicating a difference in the cross-shore gradient and suggesting that primary production occurs closer to the shore in BioEBUS than in PISCES (Fig. 10c,d). On average, Chl α concentrations in the upper 100 m are higher ($+0.3 \text{ mg m}^{-3}$) in BioEBUS than in PISCES. A substantial difference in the vertical NO₃⁻ gradient ($\pm 5 \mu\text{mol l}^{-1}/100 \text{ m}$) between the two biogeochemical models is apparent, with NO₃⁻ concentrations in the BioEBUS simulations being lower ($-5 \mu\text{mol l}^{-1}$) in the upper 100 m and higher ($+5 \mu\text{mol l}^{-1}$) at 200 m depth compared with the PISCES simulations, resulting in a distinct dipole pattern across the nutricline (Fig. 10e,f). The area of lower NO₃⁻ and higher Chl α in BioEBUS than in PISCES coincide. Subsurface potential density is on average lower (-0.02 kg m^{-3}) in BioEBUS than in PISCES, pointing to unintended physical differences between the simulations, e.g. (numerical) diffusion or surface heat flux (Fig. 10g,h). Differences in potential density on scales of $\mathcal{O}(10) \text{ km}$ between PISCES and BioEBUS which could be related to mesoscale differences between the simulations exhibit patterns that are correlated with differences in oxygen concentration (Fig. 10a,b,g,h).

4 Coupled Physical-Biogeochemical Model

In summary, the differences in the simulated biogeochemical fields due the use of either the PISCES or BioEBUS model are of similar magnitude as the impact of increased horizontal resolution. Oxygen locally exhibits positive and negative differences between PISCES and BioEBUS simulations which cancel out on average. A stronger cross-shore surface Chl α gradient and higher Chl α concentrations above the nutricline are present in BioEBUS compared with PISCES. Nitrate shows the most pronounced differences between the PISCES and BioEBUS simulations, which reveal a substantial bias in the vertical NO₃⁻ gradient. Lower NO₃⁻ concentrations above the nutricline in BioEBUS coincide with the area of higher Chl α concentrations.

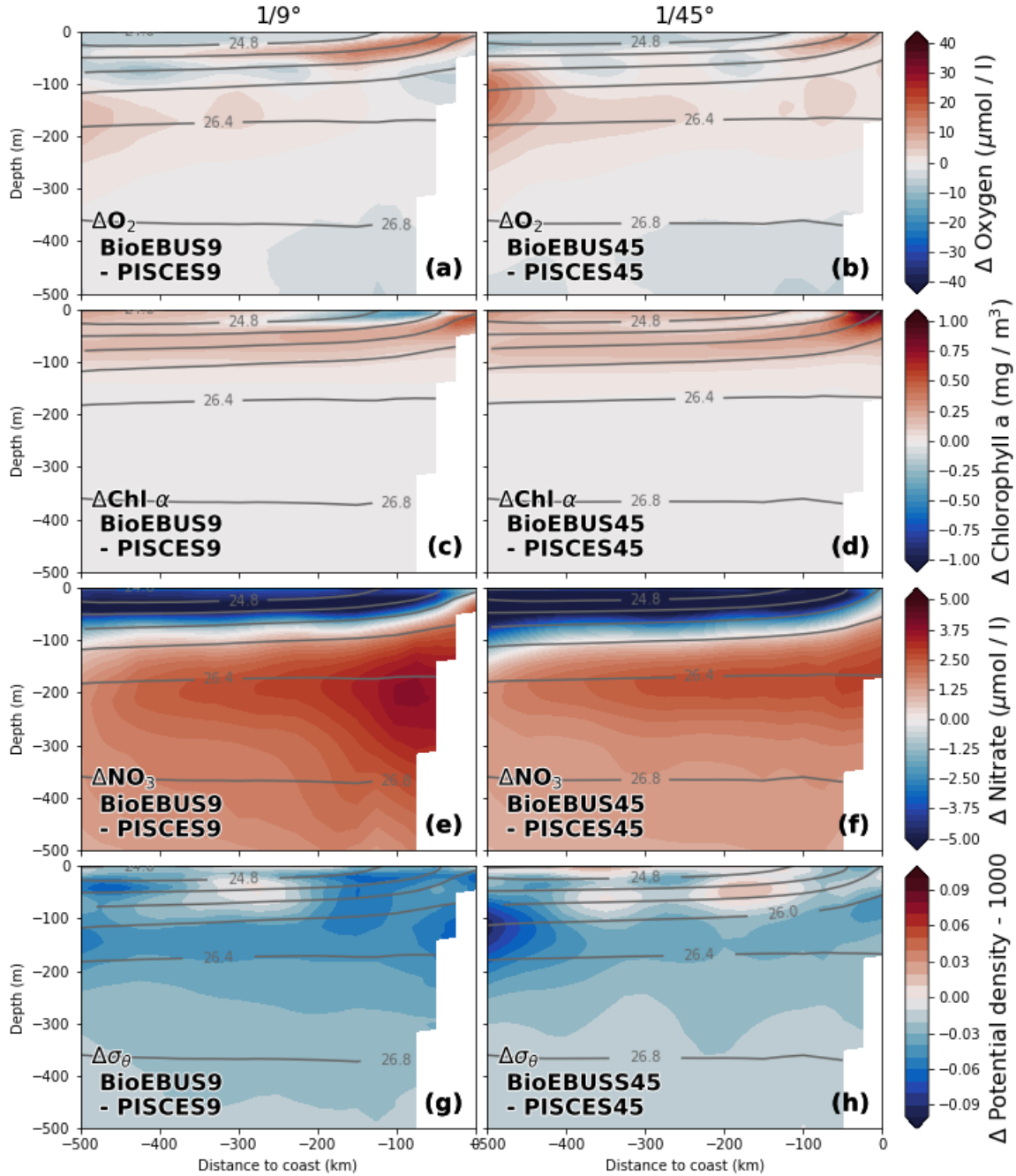


Figure 10: Relative change in (a,b) Oxygen (c,d) Chlorophyll a and (e,f) Nitrate between the BioEBUS and PISCES simulations so that positive changes represent higher values of the respective variables in the BioEBUS simulations (BioEBUS minus PISCES). Averaging procedure similar as in [Figure 6](#). Grey lines represent potential density averaged over BioEBUS9 / PISCES9 and PISCES45 / BioEBUS45, respectively.

5 Characterization of an observed cold filament

5.1 Oceanographic setting

The upwelling region along the coast is characterized by relatively steady equatorward winds that are largely parallel to the shore and sustain upwelling over the entire year (Strub *et al.*, 1998). The coldest and most persistent upwelling center along the coast is located near 15°S off Pisco (Zuta and Urquiza, 1972) and characterized by distinct maxima in mean and variance of the wind speed (Stuart, 1981; Rahn and Garreaud, 2013; Astudillo *et al.*, 2017) and wind stress curl (Bakun and Nelson, 1991). Sea-surface temperature near the coast is inversely correlated with the strength of these predominant along-shore winds and follows their seasonal cycle (Stuart, 1981; Dewitte *et al.*, 2011), consistent with the mechanism of wind-induced upwelling through Ekman transport and Ekman pumping (Sverdrup *et al.*, 1942). The wind-driven gyre circulation maintains a generally northward surface flow within the Humboldt current, but the near-surface limb of the poleward undercurrent centered at 150 m depth near the shelf may outcrop ~100 km from the coast (Penven *et al.*, 2005). The strongest upwelling-favorable winds near Pisco occur in Austral fall and winter (Dewitte *et al.*, 2011; Rahn and Garreaud, 2013) and are out of phase with the most intense phytoplankton blooms that occur in Austral summer, when a shallow mixed-layer concentrates phytoplankton near the well-lit surface and thus prevents dilution and light limitation (Echevin *et al.*, 2008). With respect to this seasonal cycle, the filament survey that was carried out on April 12-17, 2017 at the end of Austral summer falls in a period of moderate but increasing wind speed and mixed-layer depth. Moderate winds ($5 - 6 \text{ m s}^{-1}$) from south-southeast were observed close to the coast (~30 km) during transit of *R/V Meteor* from Callao to the study area near Pisco on April 11-12 (Fig. 11). The wind speed increased to 8 m s^{-1} at ~50 km distance to the first CTD station near the Paracas peninsula. Once the vessel escaped the immediate influence of the coast and started moving offshore on transect T1, the wind turned slightly onshore to southerly directions and highly variable winds with maxima of $> 12 \text{ m s}^{-1}$ were observed within ~50 km from the coast. The fluctuations in wind speed and direction in this near-

shore area seem to approximately correspond to a diurnal cycle and suggest the influence of the land-sea wind, which has been shown to be an important type of variability in the area ([Burt et al., 1973](#)). Offshore of the coastal wind speed maximum the winds diminished again to $\sim 8 \text{ m s}^{-1}$ from southeasterly directions. The highest wind speeds of the survey ($11\text{--}14 \text{ m s}^{-1}$) from southeasterly directions were observed on April 14-15 at 100-160 km distance from the coast on cross-shore transect T1 and the northern half of along-shore transect T2PHY. It is quite striking that the areas of high wind speed and high sea-surface temperature ($> 24^\circ\text{C}$) approximately coincide and that the transition from moderate (9 m s^{-1}) to high (14 m s^{-1}) winds occurs almost exactly at the upwelling front, which points to the possible relevance of SST-wind coupling ([Oerder et al., 2016](#)). A layer of clouds that is confined to the warm offshore waters downwind of transect T1 (Fig. 11, pink contour) supports this hypothesis. Between April 15-17 on a zigzag course that is formed by transects T2BIO, T3PHY and T3BIO southeasterly winds of $7\text{--}9 \text{ m s}^{-1}$ were present, only briefly increasing to $> 11 \text{ m s}^{-1}$ on April 16 over the warm water close to transect T1. Throughout the survey, winds were directed approximately parallel to the coastline. Changes in the mean wind speed during the survey are difficult to estimate due to the high spatial variability. However, two later crossings of transect T1 suggest that the mean wind decreased by $\sim 2 \text{ m s}^{-1}$ between April 14 and April 16-17.

The cold upwelling center near 15°S is readily discernible in satellite images of sea surface temperature (SST) and chlorophyll α (Chl α) taken on April 14th at 18:25 UTC (Fig. 12b). The dominant feature is a strong cross-shore temperature gradient between warm (24.5°C) offshore waters and the cold (17°C) upwelling region along the coast between Pisco and Nazca. Protruding offshore from the upwelling region are two cold filaments with temperatures of 21.5°C and $\sim 20.5^\circ\text{C}$ in their respective centers, separated by a $\sim 30\text{km}$ wide intrusion of 1°C warmer water between them. The along-shore temperature difference compared to the waters surrounding both filaments is 2.5°C . The location of the filaments in along-shore direction resembles the location of the two upwelling patches near Pisco and Nazca, suggesting that they carry recently upwelled water originating in these patches. The northern filament is extending southwestward from $15^\circ\text{S}, 77.75^\circ\text{W}$

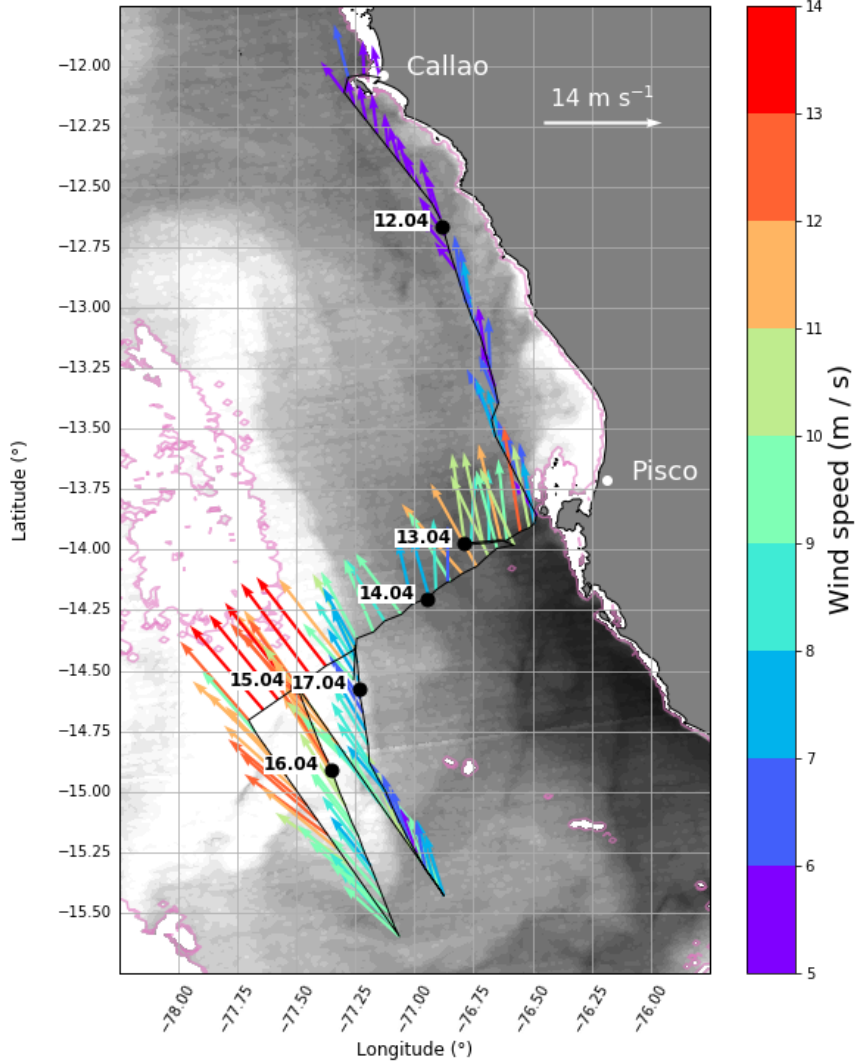


Figure 11: Direction and velocity of 1-minute wind measured at 35.5 m height between April 9 - 17, 2017. Color and length of arrow indicate wind speed, data is subsampled so that spacing between arrows is ~ 8 km. The black line indicates the cruise track, black circles mark the position of *R/V Meteor* at 00:00 UTC on the given dates. The grayscale image represents satellite sea-surface temperature (SST) on April 14 (see Fig. 12a), with black and white colors corresponding to $< 16^{\circ}\text{C}$ and $> 24.25^{\circ}\text{C}$, respectively. The light pink contour indicates missing data due to cloud cover.

to 15.5°S , 77.3°W , its width being $\sim 20\text{km}$ on average and less than 10km at its narrowest point near 15.5°S , 77°W . The southern filament is more than twice as wide, so that the along-shore extent of the two filaments combined is $> 100\text{km}$. Here we focus on the smaller northern filament, because numerous in-situ measurements exist there. The cross-shore gradient in SST is reflected by a similar gradient of Chl α concentration between the coastal upwelling (5 mg m^{-3}) and the offshore waters ($< 0.2 \text{ mg m}^{-3}$), suggesting an inverse correlation of SST and Chl α (Fig. 12b). This correlation does not exist in the bay of Pisco (13.5°S , 76.3°W), where very high Chl α concentrations of $> 10 \text{ mg m}^{-3}$ but similarly high SST ($> 24^{\circ}\text{C}$) are present. The maximum Chl α values associated with the northern and southern filaments are $\sim 1 \text{ mg m}^{-3}$ and $\sim 3 \text{ mg m}^{-3}$, respectively. Another Chl α maximum ($\sim 3 \text{ mg m}^{-3}$) is found along the main upwelling front $\sim 100 \text{ km}$ offshore, marked by a high SST gradient and a temperature of $\sim 22.5^{\circ}\text{C}$. The Chl α maximum of the northern filament is located at its northern edge as opposed to its core. It is indistinguishable from the Chl α maximum associated with the upwelling front offshore of transect T2PHY. The relative location of the associated Chl α maximum to the southern filament is unclear.

So far, the surface structure of the coastal upwelling and the associated filaments was discussed. In the following we will first describe the cross-shore structure of the upwelling region and then move on to a characterization of the observed filament in terms of both physical and biogeochemical variables based on 5 vertical transects.

The vertical cross-shore structure of the upwelling region from the coast to $\sim 160 \text{ km}$ offshore is seen Figure 14. Both maximum (25°C) and minimum (12°C) temperatures on the transect occur offshore, at the surface and at 100m depth, respectively (Fig. 14b). Maximum (35.5 g kg^{-1}) and minimum (34.75 g kg^{-1}) salinity are found at the same respective locations (Fig. 14d). These extreme values are separated by a sharp transition between $20 \text{ m} - 50 \text{ m}$ depth. The vertical gradient weakens towards the shelf as both variables show opposite cross-shore gradients at the surface and at depth. Below $\sim 80 \text{ m}$ depth

5 Characterization of an observed cold filament

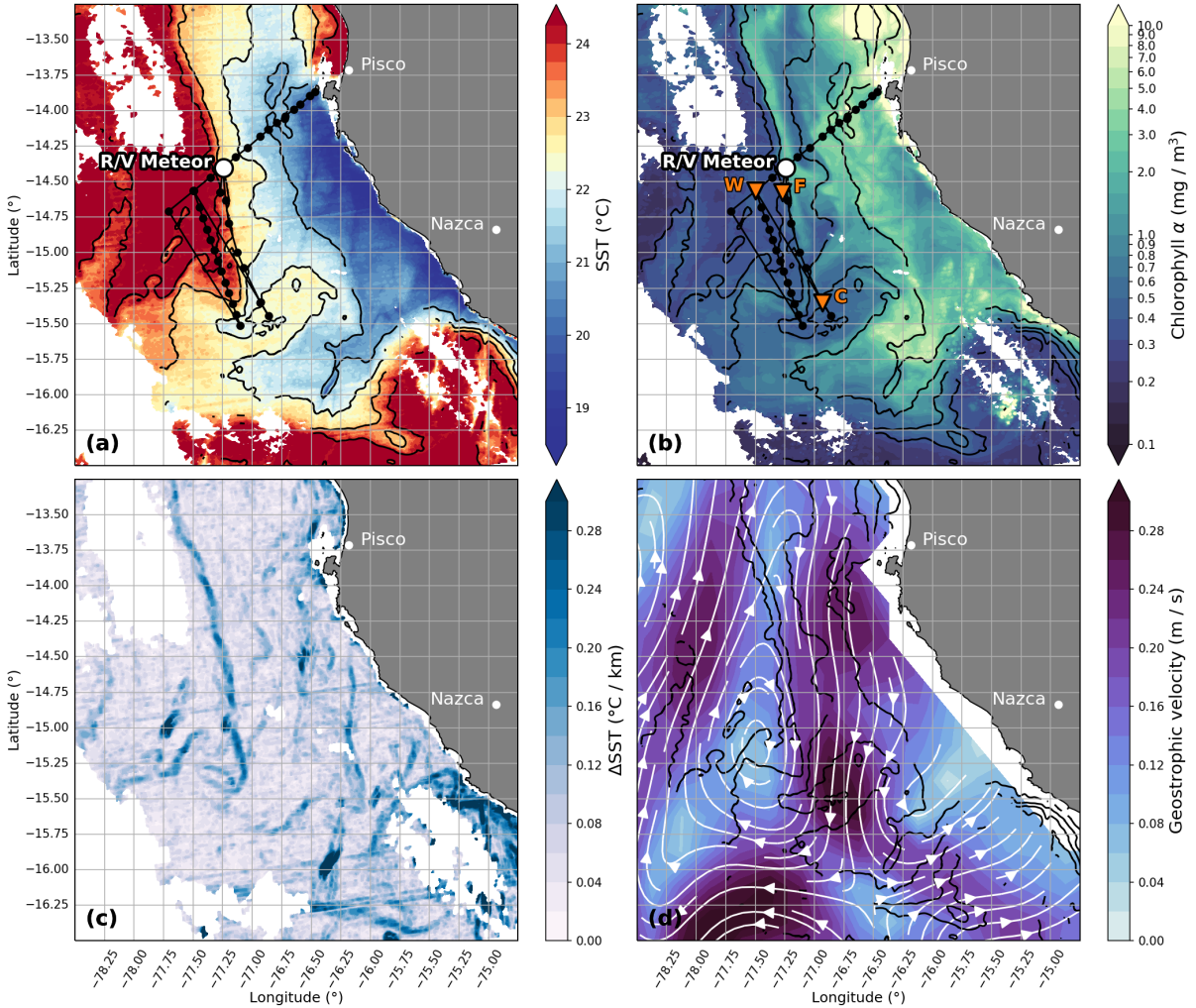


Figure 12: Satellite images of (a) SST and (b) Chlorophyll α from MODIS, taken at 18:25 UTC on April 14, 2017 (c) the absolute gradient of smoothed SST (3 km window) and (d) the geostrophic velocity on April 14, 2017 based on satellite altimetry with streamlines of the flow superimposed. The position of *R/V Meteor* at this time is marked by the white filled circle. Note the power law and logarithmic scaling for SST and Chl α , respectively. Black contours in (a,b,d) represent the 20.98 °C, 22.15 °C, 23.1 °C, and 24 °C isotherms of a smoothed SST field (2.5 km gaussian window). Black lines with filled circles indicate the cruise track and locations of CTD stations, orange triangles in (b) mark three CTD stations (W - warm, F - front, C - cold filament) where primary production was measured in addition to the regular parameters (Fig. 16). White areas in (a,b,c) were covered by clouds during overpass of the MODIS satellite and are therefore masked, grey areas are land.

both temperature and salinity are higher near the shelf (14°C , 35 g kg^{-1}) than in the open ocean (13°C , 34.75 g kg^{-1}). The lowest sea-surface temperature (SST) of 17°C occurs on the shelf in the upwelling patch near Pisco (Fig. 14b). SST in the survey area almost continuously increases offshore, accompanied by an increase in mixed-layer depth from 5 m to 30 m and a decrease in density from 1025.5 kg m^{-3} to 1024 kg m^{-3} . An exception from this average cross-shore gradient is a 10 km wide cold anomaly of 1°C at 40 km cross-shore distance, coinciding with both an upward displacement of the 1025 kg m^{-3} isopycnal and a deepening of the mixed-layer by 10m, respectively (Figs. 14b). The cold anomaly can be related to a small filament discernible in Figure 12a extending northward across transect T1 from the upwelling patch. The filament is associated with a small northward velocity anomaly in a predominantly southward current, resulting in high horizontal velocity shear ($0.6 \text{ m s}^{-1} / 20 \text{ km}$) on its offshore side (Fig. 14h). The prevailing southward flow of $0.2 - 0.3 \text{ m s}^{-1}$ within 120 km from the coast is in good agreement with geostrophic current estimates from satellite altimetry (Fig. 12d). The strongest cross-shore SST gradient ($0.2^{\circ}\text{C km}^{-1}$) occurs 20 km from the coast. A slightly smaller peak ($0.15^{\circ}\text{C km}^{-1}$) is found 110 km offshore, approximately at the outcrop of the 1024 kg m^{-3} isopycnal. This is the location of the main along-shore upwelling front separating cold coastal and warm offshore waters (Fig. 12a). Low SST gradients ($< 0.05^{\circ}\text{C km}^{-1}$) are present within 20 km on both sides of the front (Fig. 14b). The presence of several distinct peaks in stratification between 10 - 30 m depth could indicate that the vertical temperature drop by 0.2°C in the top 10 m is due to day-time restratification and that the night-time mixed-layer is deeper. The lowest sea-surface salinity (SSS) of 35 g kg^{-1} occurs at 20 km offshore, just eastward of the cold anomaly described above (Fig. 14d). SSS between 40 km and 100 km offshore is almost uniform at $\sim 35.25 \text{ g kg}^{-1}$ in the upper 30 m, one exception being a slight fresh anomaly of 0.05 g kg^{-1} along the 21°C isotherm. Another narrow ($\sim 1 \text{ km}$) fresh anomaly of the same magnitude appears just east of the main SST front 100 km along the transect. Below the mixed-layer (45 m) in the middle of the transect (70 km) there is a 30 m thick layer of relatively homogeneous temperatures between 17°C and 19°C , coinciding with a downward displacement of the 1025.5 kg m^{-3}

isopycnal by 10 m - 15 m and a local salinity maximum of 35.3 g kg^{-1} (Fig. 14b,d). The buoyancy frequency squared (N^2) exhibits a minimum ($< 1.5 \times 10^{-4} \text{ s}^{-1}$) in between a local stratification maximum ($N^2 \sim 3 \times 10^{-4} \text{ s}^{-1}$) below and the strongly stratified base of the mixed-layer ($N^2 > 9.5 \times 10^{-4} \text{ s}^{-1}$) above (Fig. 14f). The cross-shore gradients of temperature and salinity reverse below $\sim 80 \text{ m}$ depth so that both are higher near the shelf (14°C , 35 g kg^{-1}) than in the open ocean (13°C , 34.75 g kg^{-1}). Differences between isotherms and isopycnals increase with depth. While they coincide at the surface, there is a change of almost 1°C along the 1026 kg m^{-3} isopycnal. The observed properties along transect T1 can be related to different water masses that are present in the area. The salinity minimum below 60 m depth between 100-160 km offshore corresponds to Eastern South Pacific Intermediate Water (ESPIW), which is marked by a sharp corner in the T-S curve (Fig. 13) at a density of about $\sigma_\theta = 26.3$ (Schneider *et al.*, 2003). At the same density and 0.2 g kg^{-1} higher salinity Equatorial Subsurface Water (ESSW) can be identified, a poorly oxygenated water mass located near the shelf that is transported southward by the poleward undercurrent (Gunther, 1936; Fonseca, 1989; Fiedler and Talley, 2006; Silva *et al.*, 2009; Montes *et al.*, 2010). Two distinct salinity maxima are visible, the first of which at $\sigma_\theta = 24.1$ represents the relatively warm (23.5°C) offshore surface waters. The second maximum at $\sigma_\theta = 25.5$ corresponds to the weakly stratified subsurface water 60 - 80 km from the coast in transect T1 (Fig. 14). Its high absolute salinity of 35.5 g kg^{-1} and low stratification suggest a classification as South Pacific Eastern Subtropical Mode Water (SPESTMW) or Subtropical Surface Water (STSW), both of which originate at the southeastern margin of the subtropical gyre (Wyrtki, 1967; Karstensen and Quadfasel, 2002; Fiedler and Talley, 2006; Silva *et al.*, 2009). Low silica concentrations of $2\text{-}5 \mu\text{mol l}^{-1}$ (not shown) and relatively high oxygen concentrations for its density surface ($160 \mu\text{mol l}^{-1}$) further substantiate the hypothesis of South Pacific origin.

Due to coastal upwelling, nutrient-rich subsurface waters are brought to the surface. A sharp nutricline (the portion of the water column where nutrients increase maximally with depth) with a vertical gradient of up to $2 \mu\text{mol l}^{-1} \text{ m}^{-1}$ is apparent 140 km off-

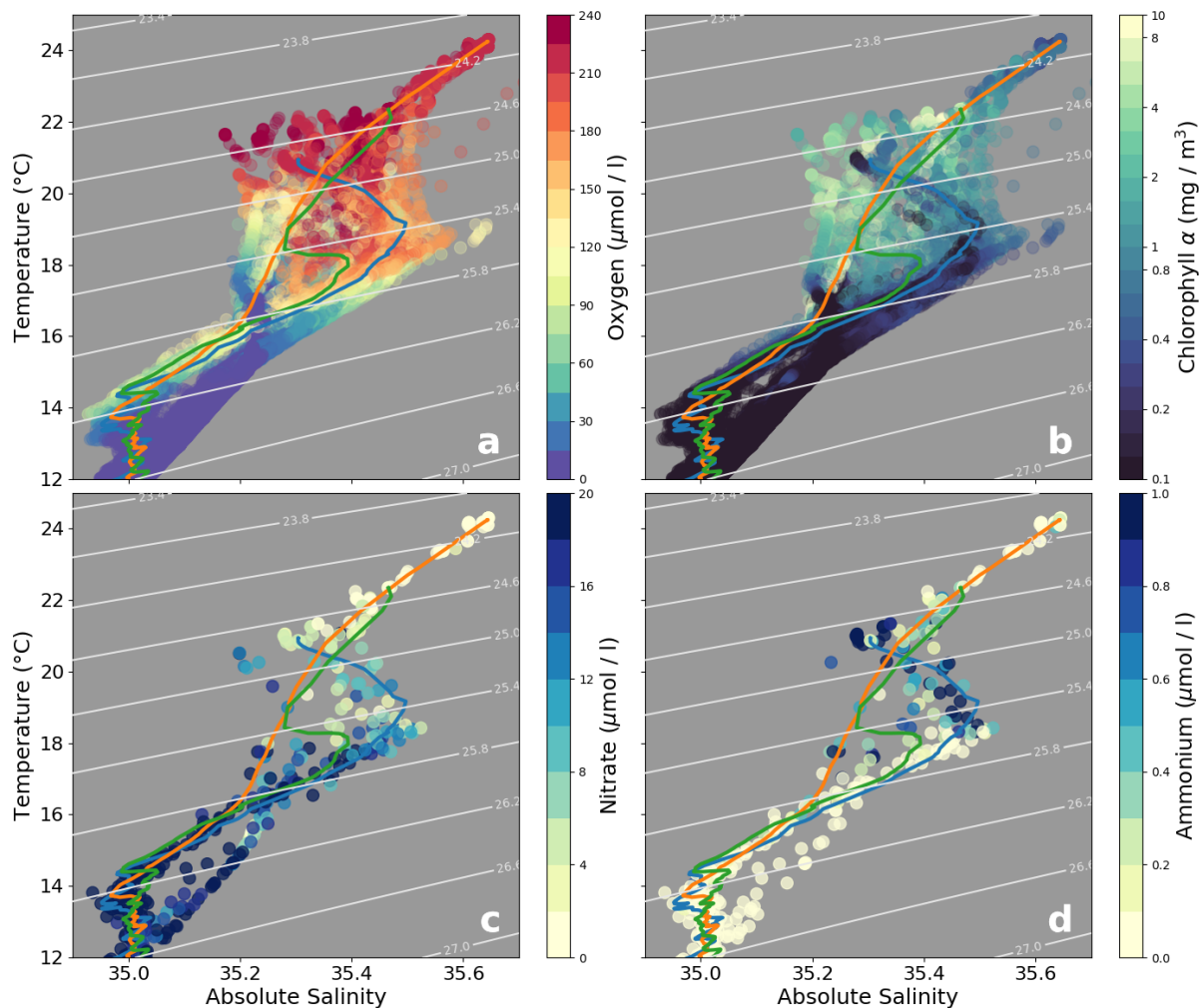


Figure 13: T-S diagram for all CTD data acquired in the study area around 15°S with colors mapped to (a) oxygen (b) chlorophyll α (c) nitrate and (d) ammonium concentrations. Lines correspond to vertical profiles at the (orange) "Warm" (green) "Front" and (blue) "Cold filament" stations where primary production was measured (Fig. 16a-c). Light grey lines are contours of potential density - 1000 kg m^{-3} .

shore. Towards the shore, the nutricline becomes less distinct and intersects the surface ~ 40 km from the coast. While the offshore surface waters are almost completely depleted of nutrients ($< 1 \mu\text{mol l}^{-1}$ nitrate + nitrite, $< 0.25 \mu\text{mol l}^{-1}$ ammonium), surface nitrate / nitrite concentrations are as high as $15 \mu\text{mol l}^{-1}$ / $1 \mu\text{mol l}^{-1}$ within 50 km of the coast (Fig. 14e,g,h). Two profiles within 20 km from the coast show a pronounced nitrate minimum ($< 2 \mu\text{mol l}^{-1}$) between 40 - 80 m depth that coincides with oxygen concentrations of $< 2 \mu\text{mol l}^{-1}$ and a nitrite maximum of $5 \mu\text{mol l}^{-1}$ (Fig. 14a,g,h). The nitrite maximum extends no further than 40 km offshore, where the oxycline drops and oxygenated waters ($> 100 \mu\text{mol l}^{-1}$) are found down to 80 m depth. Nitrite concentrations of up to $1.5 \mu\text{mol l}^{-1}$ are present within 60 km from the coast and locally along the nutricline further offshore. Ammonium concentrations in the mixed-layer are elevated ($0.5 - 1 \mu\text{mol l}^{-1}$) within 90 km from the coast (Fig. 14g). Between 40 km - 90 km offshore, the positive anomaly extends to 20 m below the mixed-layer and coincides with a local chlorophyll α minimum in the mixed-layer (Fig. 14c). Maximum ammonium levels on transect T1 ($2 \mu\text{mol l}^{-1}$) occur at this location. Note that only nitrate and no ammonium was measured at stations 1, 3 and 4 on this transect, station 1 being the one closest to the shore. Chlorophyll α concentration is very low ($< 0.1 \text{ mg m}^{-3}$) below 80 m depth everywhere along the transect (Fig. 14c). Close to the shelf, the low-chlorophyll α waters follow the slope of the isopycnals upwards to 20 m depth, coinciding with the distribution of anoxic waters ($< 2 \mu\text{mol l}^{-1}$). Above this depth, there are three distinct Chl α maxima along the transect: In the mixed-layer (A) between 10 - 45 km offshore ($\sim 5 \text{ mg m}^{-3}$), (B) between 80 - 110 km offshore ($> 10 \text{ mg m}^{-3}$) and (C) just below the mixed-layer at 40 m depth, between 120 - 160 km offshore ($> 10 \text{ mg m}^{-3}$). Both mixed-layer maxima correspond to local minima in the SST gradient (Fig. 14b). Maximum (A) goes along with a salinity minimum, which suggests that this water has its source in the coastal upwelling (Fig. 14-d). The chlorophyll α maximum on the cold side of the upwelling front, between the outcropping 1024 kg m^{-3} and 1024.5 kg m^{-3} isopycnals, coincides with an oxygen maximum ($> 250 \mu\text{mol l}^{-1}$). On the warm side of the front there is a pronounced chlorophyll α minimum ($< 0.2 \text{ mg m}^{-3}$) which marks the lowest chlorophyll α in the mixed-layer

along the transect. This results in a dipole pattern of Chl α across the front. Oxygen concentrations are highest at the surface ($\sim 240 \mu\text{mol l}^{-1}$) and decrease rapidly with depth towards anoxic levels ($< 2 \mu\text{mol l}^{-1}$) in the oxygen minimum zone between 150 m - 400 m (Fig. 14a). The oxygen maximum ($\sim 250 \mu\text{mol l}^{-1}$) is located in the mixed layer between 80 km and 100 km offshore, on the cold side of the main upwelling front. The front is marked by a local maximum of the SST gradient ($0.15^\circ\text{C km}^{-1}$), while ΔSST is very low ($< 0.05^\circ\text{C km}^{-1}$) in the area of the O₂ maximum on its inshore side, coinciding with high (10 mg m^{-3}) Chl α concentrations (Fig. 14a-c). The depth of the oxycline - approximately given by the $100 \mu\text{mol l}^{-1}$ contour - varies between 5 m near the coast and 90 m about 80 km offshore. The oxycline separates from the base of the mixed-layer ~ 30 km from the coast and follows a second stratification maximum downward (Fig. 14a,f). Further offshore it shallows again and eventually joins the mixed-layer approximately at the location of the main upwelling front ~ 100 km from the coast. The volume of relatively oxygen-rich ($> 120 \mu\text{mol l}^{-1}$) water between oxycline and mixed-layer in the middle of the section corresponds to the saline, weakly stratified subsurface waters described above.

In summary the vertical and cross-shore structure of all physical and biogeochemical parameters in the study area is dominated by the coastal upwelling bringing relatively cold, fresh, nutrient-rich and oxygen-depleted waters to the surface, which results in strong cross-shore gradients of the respective fields. Chlorophyll α in satellite images exhibits a similar gradient between high concentrations near the coast and low concentrations offshore, even though the small-scale variability seems to be related to SST fronts and filaments.

5.2 Cold filament

A cold filament originating in the upwelling patch near Pisco was observed during cruise M136. The filament can be identified in satellite SST images as early as March 22 and changed its position only on $\mathcal{O}(10)$ km until it was sampled on April 15 (not shown). The associated SST fronts separating the upwelling patch and the filament from the warmer

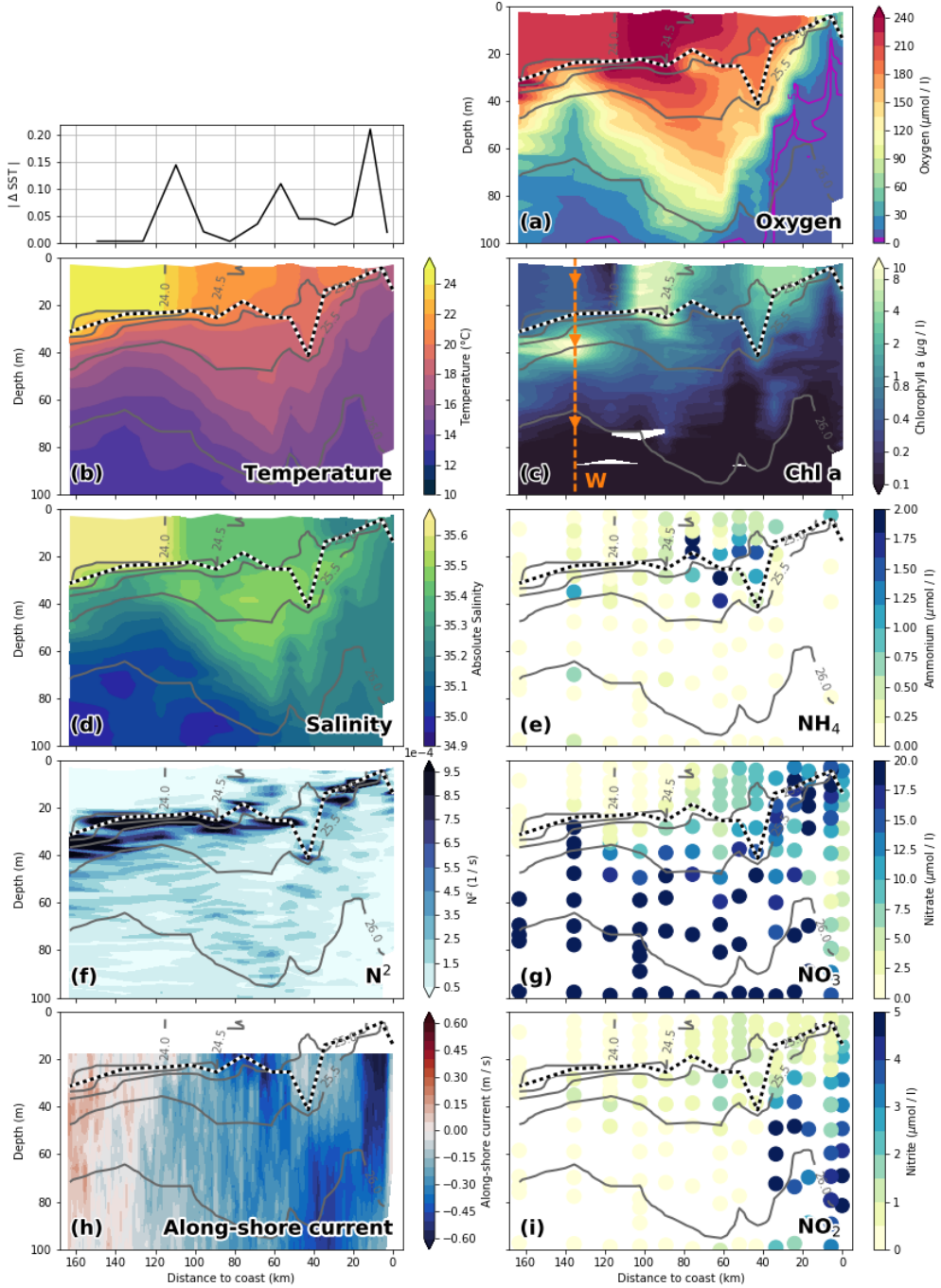


Figure 14: (a) Oxygen (b) Δ SST / temperature (c) chlorophyll α (d) absolute salinity (e) ammonium (f) buoyancy frequency squared (g) nitrate (h) along-shore current (positive northward, rotated 8° anti-clockwise from due north) and (i) nitrite on cross-shore transect T1. Grey lines are the 24, 24.5, 25, 25.5 and 26 kg m^{-3} contours of σ_θ (potential density - 1000). The dashed black-and-white line denotes the mixed-layer depth (MLD) being defined here as the maximum of the squared buoyancy frequency N^2 . The orange dashed line and triangles in (c) mark the "warm" primary production sampling site and depths (Fig. 16a).

offshore waters are present the entire time, but vary in strength. Measurements were taken along 4 along-shore transects across the filament two of which were regular CTD sections with a spacing of ~ 10 km between profiles (T2BIO, T3BIO). On the two remaining transects (T2PHY, T3PHY) only physical parameters were measured, but at much higher resolution with distances between profiles of only 500 m - 900 m. A description of the geographical setting of the study area and the location of the transects is given in section 3. The physical structure of the filament and the distribution of the biogeochemical parameters is characterized in the following.

High-resolution temperature and salinity measurements and the squared buoyancy frequency (N^2) during two crossings of the cold filament (T2PHY, T3PHY) are shown in Figure 15. The filament is located at ~ 110 km distance from transect T1 bounded by the outcropping 1025.5 kg m^{-3} isopycnal, defining its extent by the mixed layer salinity minimum (35.2 g kg^{-1}). Temperature ranges from 24.5°C in the mixed-layer at the northern end of both transects to 16°C at 50 m depth below the maximum. Salinity varies from 35.6 g kg^{-1} in the mixed-layer to 35.25 g kg^{-1} at 50 m depth. Both sea-surface temperature (SST) and salinity (SSS) decrease with distance from the cross-shore transect towards the filament, where the respective minima (20.5°C , 35.2 g kg^{-1}) are found. An exception to this large-scale gradient is a cold (1°C) / fresh (0.2 g kg^{-1}) anomaly at ~ 40 km along transect T2PHY, which is associated with a decrease in mixed-layer depth (MLD) by 20 m (Fig. 15a,c). This is the shallowest MLD (8 m) present on both transects. Satellite images reveal that this anomaly is part of a hook-shaped instability of the front at the northern edge of the filament, bending northeastward towards section T2PHY (Fig. 12). The anomaly is associated with an onshore current of $\sim 0.2 \text{ m s}^{-1}$ 20-35 m depth. Two distinct local maxima in ΔSST are visible in transect T2PHY. The SST gradient at the instability is considerably higher ($0.4^\circ\text{C km}^{-1}$) than at the main front ($0.3^\circ\text{C km}^{-1}$) just north of the SST minimum. Both ΔSST maxima coincide with (MLD) minima (~ 10 m). On transect T3PHY, two minima in SST are present. The minimum associated with the cold filament at 100 km along the transect is 10 km in width and associated with an in-

crease in MLD by ~ 10 m. The second cold anomaly is only 2-3 km wide, coincides with an MLD increase of ~ 5 m and shows higher salinity than the main filament. While satellite images at the time are inconclusive, this could indicate that the anomaly is also caused by a frontal instability like on transect T2PHY. At the northern end of both sections, close to the cross shore transect, the vertical salinity maximum is located at the surface. As the mixed-layer salinity decreases approaching the filament, the maximum shifts down to 50 m depth, just below the mixed layer. The subsurface salinity maximum coincides with a region of low stratification ($N^2 < 1 \times 10^{-4} \text{ s}^{-1}$) and relatively homogeneous temperature ($17^\circ\text{C} - 19^\circ\text{C}$), similar in its characteristics to the weakly stratified subsurface layer on transect T1 described in [Section 5.1](#). Minimum and maximum stratification are found in the mixed-layer ($N^2 < 0.5 \times 10^{-4} \text{ s}^{-1}$) and at the base of the mixed-layer ($N^2 > 5 \times 10^{-4} \text{ s}^{-1}$), respectively. In the mixed-layer, isopycnals are almost vertical and there is little small-scale horizontal variability of the physical parameters due to insufficient stratification. Below the ML, there is strong variability of all physical parameters on scales of $\mathcal{O}(1 \text{ km})$ with vertical isopycnal displacements of up to 10 m, concomitant with similar variability in MLD. On scales of $\mathcal{O}(10) \text{ km}$ along both transects, the depth of the mixed-layer varies from 8 m to 38 m. An offshore current of $0.3 - 0.4 \text{ m s}^{-1}$ is found below the filament (Fig. [15g,h](#)). Although the velocity measurements located within the ML are sparse, they are well correlated with the temperature and salinity data, density surfaces and the base of the mixed-layer. It is therefore justified to assume the velocity measurements located within the ML are representative for the 18 m of the water column above where no measurements are available due to the blanking distance of the vmADCP. The direction of the average flow below the ML corresponds favorably with the geostrophic velocity estimated from satellite altimetry (Fig. [12d](#); [15f,h](#)). Offshore velocities below the filament and especially in the ML are by a factor of 2 higher than geostrophic velocity estimates, pointing to ageostrophic currents associated with the filament. Local maxima in offshore velocity correspond to temperature and salinity minima and MLD maxima in narrow bands of ~ 10 km width at 80 km / 110 km distance along transect T3PHY (Fig. [15b,d,h](#)). Low salinity anomalies (35.3 g kg^{-1}) below the ML at ~ 40 m depth in

conjunction with weak stratification (Fig. 15c-f) could indicate water that was subducted by submesoscale frontal processes. A considerable velocity shear of 0.4 m s^{-1} over only 15 m depth is present at 5-25 km distance along transect T2PHY, coinciding with the area of most stable stratification and thus revealing a strong decoupling of the ML from subsurface waters in this area (Fig. 15e,g). Moreover, these opposing velocities suggest a flow of warm water in the mixed layer on top of colder water on the offshore side of transect T2PHY that acts to restratify the surface layer, a process known to be associated with submesoscale instabilities (*Thomas et al., 2008*). This interpretation is supported by discontinuities in the SST front at the location of the instability (Fig. 12c). In contrast, a lower velocity shear of only $0.1\text{-}0.2 \text{ m s}^{-1}$ across the mixed-layer base is seen in the filament (Fig. 15e,g).

High variability of all biogeochemical parameters (nitrate, ammonium, chlorophyll α , oxygen) is found on two transects across the cold filament (T2BIO, T3BIO; Fig. 17; 18). On transect T2BIO, 3 profiles with nutrients measured from water samples are located within the filament, all of which consistently show elevated nutrient concentrations compared to the surrounding waters. Nitrate levels are as high as $5 \mu\text{mol l}^{-1}$ at the filament's edge, which is comparable to the value found on the cross-shore transect T1 at ~ 70 km offshore. At the southernmost station of transect T1BIO, nitrate concentrations are slightly lower ($< 4 \mu\text{mol l}^{-1}$), while ammonium concentrations are maximum ($2 \mu\text{mol l}^{-1}$). Ammonium levels in the mixed-layer are above $1.2 \mu\text{mol l}^{-1}$ inside the filament. Outside the filament, nutrient profiles are similar to transect T1 (Fig. 14e,g). Nitrate concentrations are low ($< 0.2 \mu\text{mol l}^{-1}$) in the mixed-layer and high ($> 20 \mu\text{mol l}^{-1}$) below ~ 60 m depth (Fig. 14e). Ammonium shows generally low ($< 0.2 \mu\text{mol l}^{-1}$) values and only occasional peaks ($\sim 1 \mu\text{mol l}^{-1}$) below the mixed-layer (Fig. 14g). For example, ammonium concentrations of $0.5\text{-}1 \mu\text{mol l}^{-1}$ within 20 meters below the mixed-layer are present at some stations along the transect (i.e. 50 km and 80 km). These profiles also show chlorophyll α maxima at the same or shallower depths. High chlorophyll α (8 mg m^{-3}) is found just outside the filament, at the local maximum in SST gradient located 75 km along the

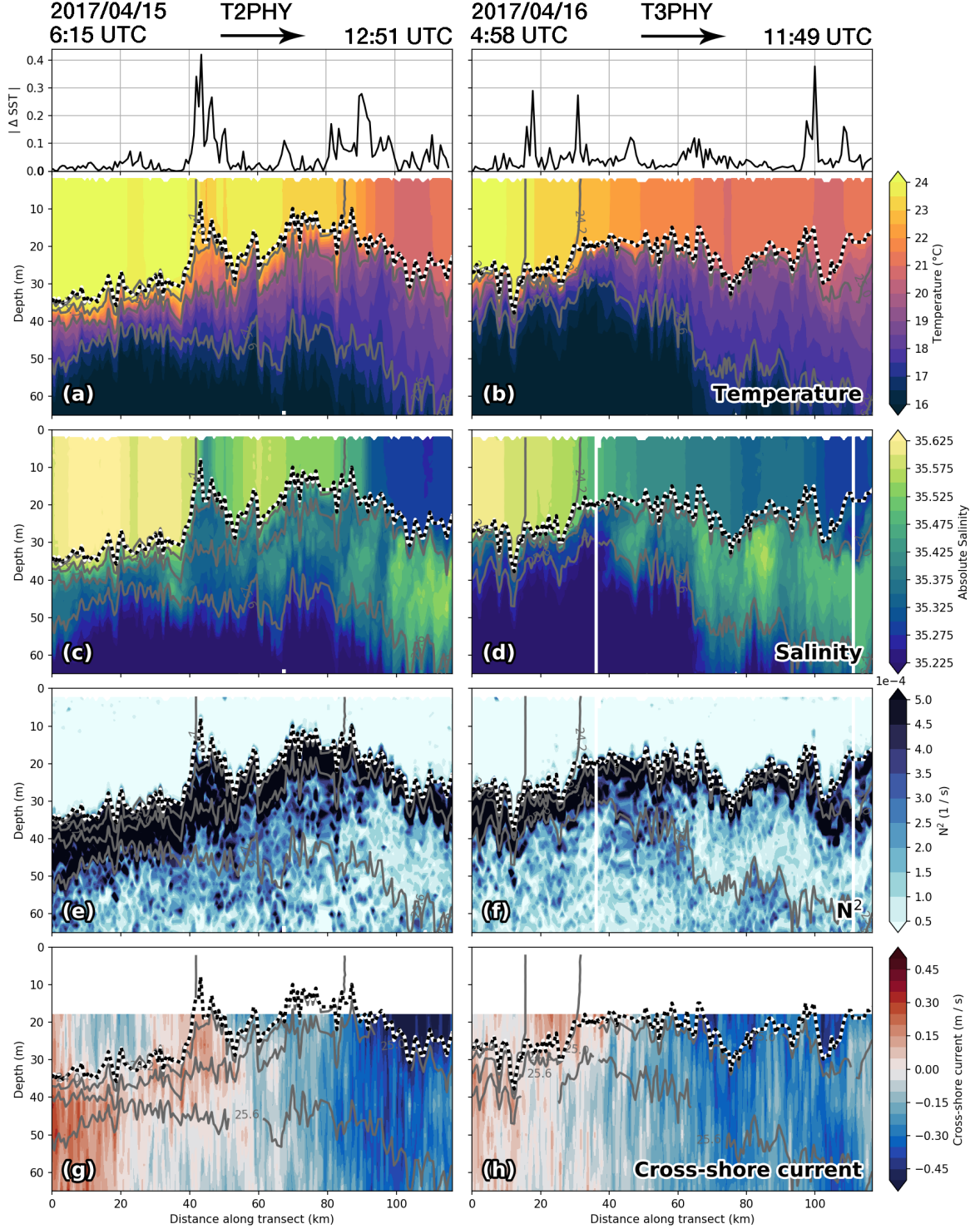


Figure 15: (a,b) Temperature (c,d) salinity (e,f) buoyancy frequency squared and (g,h) cross-shore currents (positive onshore, rotated 35° clockwise from due north) on along-shore transects (left panels) T2PHY and (right panels) T3PHY. Grey lines are the 24, 24.25, 25 and 25.6 kg m⁻³ contours of potential density - 1000. The dashed black-and-white line denotes the mixed-layer depth (MLD) here defined as $T(\text{mld}) = T(\text{surface}) - 0.2^\circ\text{C}$.

transect (Fig. 17c). A subsurface ammonium maximum ($> 1 \mu\text{mol l}^{-1}$) with 30 m vertical extent is found below this mixed-layer chlorophyll α maximum (Fig. 17g). Inside the filament, chlorophyll α concentrations are very low ($< 0.1 \text{ mg m}^{-3}$). The boundary between these two extreme values of mixed-layer chlorophyll α is approximately given by the outcropping 1024.5 kg m^{-3} isopycnal. Within 50 km on the warm side of the SST front, a subsurface chlorophyll α maximum ($> 10 \text{ mg m}^{-3}$) is found at ~ 40 m depth, along the 1025.5 kg m^{-3} isopycnal. Apart from the described features, Chl α concentrations between $0.5 - 1 \text{ mg m}^{-3}$ are present at depths shallower than 60 m, below which Chl α rapidly decreases to $< 0.1 \text{ mg m}^{-3}$. While oxygen in the mixed-layer is high ($> 210 \mu\text{mol l}^{-1}$) everywhere along the transect, there is a distinct maximum ($\sim 240 \mu\text{mol l}^{-1}$) at the edge of the filament, coinciding with the Chl α maximum described above (Fig. 17-a). The coincidence of Chl α and O₂ maxima in the mixed-layer is also apparent along transect T1, suggesting that this may be a more general feature. The oxycline on transect T2BIO - approximately given by the $100 \mu\text{mol l}^{-1}$ contour - closely follows the base of the mixed-layer until ~ 70 km distance from the cross-shore transect (Fig. 17-a). At this location the oxycline suddenly drops by 30 m over a distance of 20 km, beyond which relatively high oxygen concentrations extend as far as 60 m below the mixed-layer. On transect T3BIO the oxycline also deepens with distance from the cross-shore transect, but does so gradually and is generally deeper and less distinct (Fig. 18-a). This agrees well with the cross-shore variation of oxycline depth seen in transect T1 (Fig. 14-a), where the distance of ~ 30 km between transects T2BIO and T3BIO translates to a deepening of the oxycline by 10 m - 20 m and a notably reduced vertical O₂ gradient. It should also be noted that this layer of relatively oxygen-rich water is weakly stratified ($N^2 < 1.5 \times 10^{-4} \text{ s}^{-1}$) and found at the same location as the subsurface salinity maximum described above. The characteristics of this water are similar to those of the homogeneous subsurface layer described in Section 5.1.

Chlorophyll α measurements on along-shore transects across the filament seem to suggest that primary production is elevated only at the edge of the filament but low in its core (Figs. 17-c; 18-c), seemingly contradicting previous studies ([Chavez et al., 1991](#); [Strub](#)

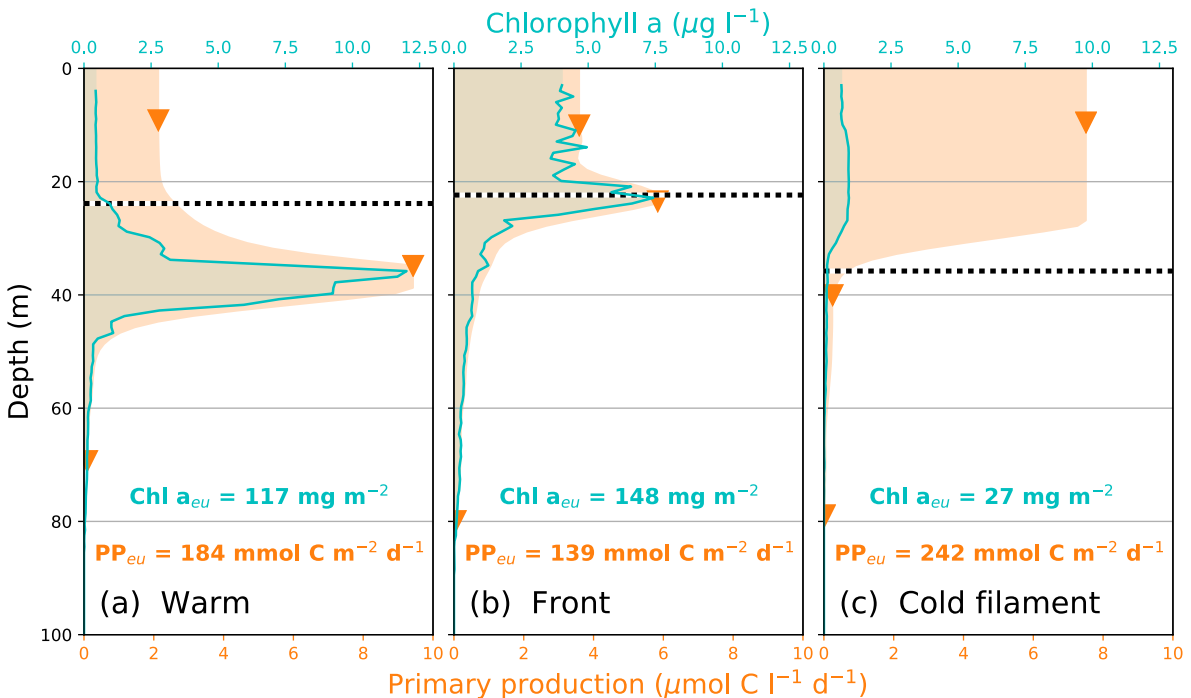


Figure 16: Primary production (orange), chlorophyll α concentration (cyan) and mixed-layer depth (black, dashed) for three stations located (a) in warm offshore waters (b) at the upwelling front and (c) in the cold filament, respectively. The mixed-layer depth is here defined as the maximum of the squared buoyancy frequency N^2 . Exact locations of stations are marked by the orange triangles in Figure 12b. The vertical integrals over the euphotic zone of primary production (PP_{eu}) and chlorophyll α ($\text{Chl } \alpha_{eu}$) for each station are given below the curves, the orange shading representing estimated PP profiles that were used for the integration. The profiles were constructed by regressing a smoothed (3 m gaussian window) Chl α curve onto observed PP and limiting the thus estimated PP curve to the observed maximum at each station. Constant PP in the top 10 m is assumed and any contribution to the vertical integral below the deepest measurement neglected.

et al., 1991) that identify filaments as maxima of Chl α . Measurements of primary production (PP) inside the filament (Fig. 16-c), at the upwelling front (Fig. 16-b) and in the warm offshore waters (Fig. 16-a) reveal that such a conclusion would be premature. As described above, maximum chlorophyll α concentrations of $\sim 1 \text{ mg m}^{-3}$ inside the filament are only 10 - 20 % of those at the upwelling front (7.5 mg m^{-3}) and in the warm waters (12 mg m^{-3}), respectively. However, differences in maximum primary production between the filament ($7.5 \mu\text{mol C l}^{-1} \text{ d}^{-1}$), the upwelling front ($3.6 \mu\text{mol C l}^{-1} \text{ d}^{-1}$) and the warm water station ($9.4 \mu\text{mol C l}^{-1} \text{ d}^{-1}$) are much smaller than Chl α measurements alone would suggest. It is especially noteworthy that the filament exhibits higher maximum PP than the upwelling front, which dominates the offshore Chl α variability in satellite images (Fig. 12-b; 16-b,c). While surface Chl α is much higher at the upwelling front ($5 \mu\text{mol l}^{-1}$) than at the other two stations ($0.5 - 1 \mu\text{mol l}^{-1}$), the surface $PP : \text{Chl } \alpha$ ratio is also the lowest by far with 5 - 10 times less PP per unit Chl α (Fig. 16a-c). When depth-integrated Chl α is considered, the differences are even more striking as the water column in the filament only contains 20 - 25% of the Chl α (27 mg m^{-3}) that is present at the warm-water station (117 mg m^{-3}) and the upwelling front (148 mg m^{-3}). Despite this, depth-integrated PP in the filament ($242 \text{ mmol C m}^{-2} \text{ d}^{-1}$) is 25 % *higher* compared with the warm-water station ($184 \text{ mmol C m}^{-2} \text{ d}^{-1}$) and 40 % higher than at the upwelling front ($139 \text{ mmol C m}^{-2} \text{ d}^{-1}$). The maximum of PP in the filament occurs at 10 m depth within a deep mixed-layer (35 m), while at the upwelling front and in the warm water the maximum is located below the mixed-layer at 25 m and 36 m depth, respectively. The fraction of the vertically integrated PP that occurs below the mixed-layer is $> 50 \%$ at the warm water station, $\sim 30 \%$ at the upwelling front and $< 1 \%$ in the cold filament, further distinguishing the three regimes. It should be noted that the vertical integral of PP is strongly dependent on the assumed vertical profile especially below the mixed layer. If e.g. a linear interpolation is used, the resulting integrated PP at both the warm water station and the upwelling front is higher than in the cold filament and likely overestimated. We therefore used a linear regression of PP on a slightly smoothed Chl α profile to interpolate between the measurements, resulting in a more realistic PP distribution

5 Characterization of an observed cold filament

exponentially decaying with depth. Independent of this interpolation technique is the result that substantial depth-integrated primary production comparable to the other two stations occurred in the filament despite only 20- 25% of the depth-integrated chlorophyll α , and that the vast majority of this primary production is confined to the mixed-layer.

It can be summarized that the observed cold filament contains relatively cold, fresh and nutrient-rich waters originating in the coastal upwelling, which results in a distinct along-shore variability of the physical and biogeochemical fields. Enhanced nitrate concentrations and offshore velocities of up to 0.5 m s^{-1} within the filament suggest the offshore transport of nutrients. Even though nutrients are abundant, chlorophyll α concentrations are very low inside the filament and highest at the boundary separating it from the nutrient-depleted, warm offshore waters. High ammonium concentrations coinciding with low chlorophyll α concentrations are observed in the core of the filament, suggesting that remineralization of organic matter dominates primary production in the recently upwelled water. Despite the low Chl α concentrations, depth-integrated primary production is 40% higher than at the upwelling front and 25% higher than offshore, pointing to a high uncertainty associated with the use of chlorophyll α as a proxy for primary production.

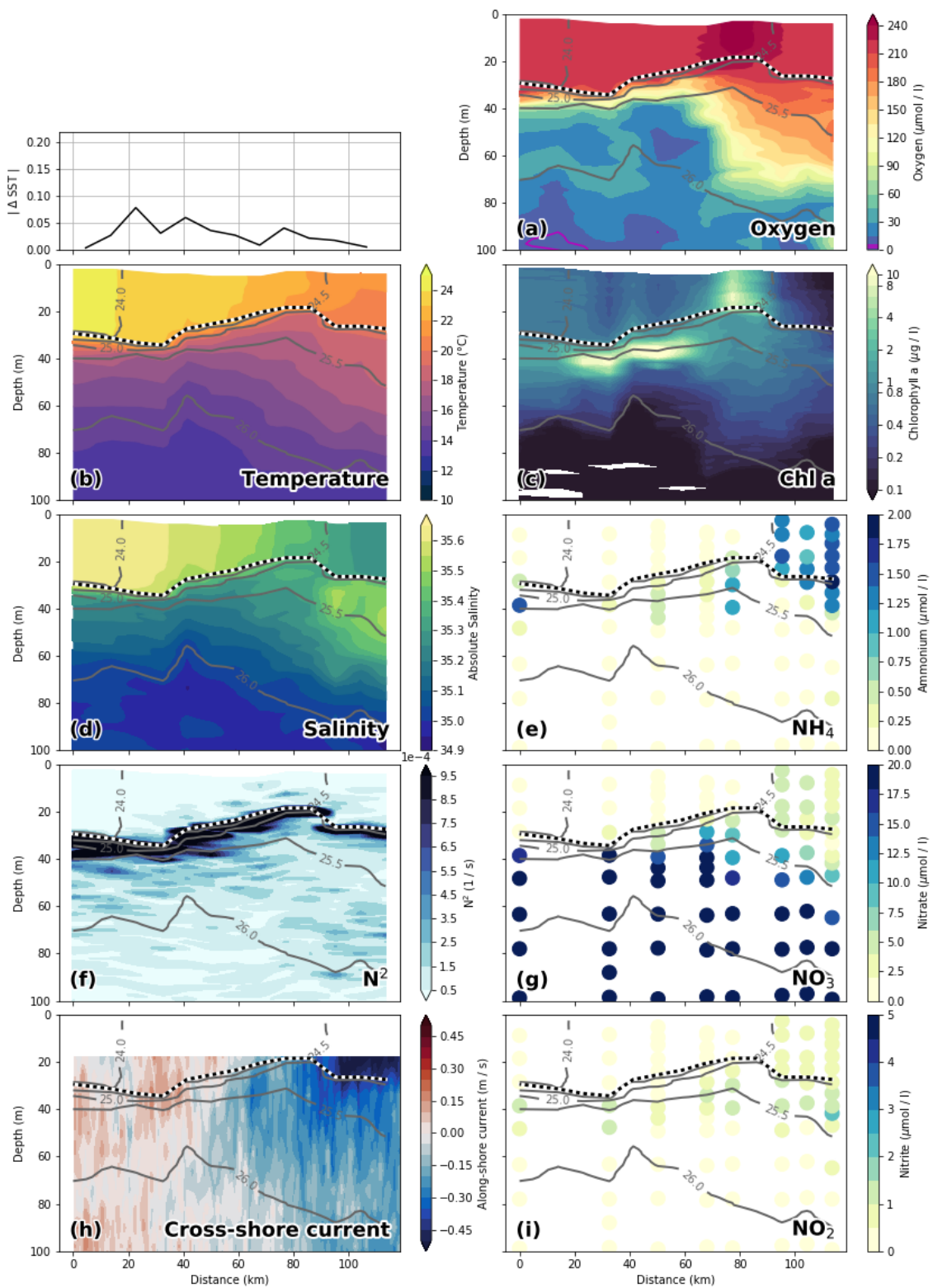


Figure 17: Along-shore transect T2BIO. Same elements as in Figure 14.

5 Characterization of an observed cold filament

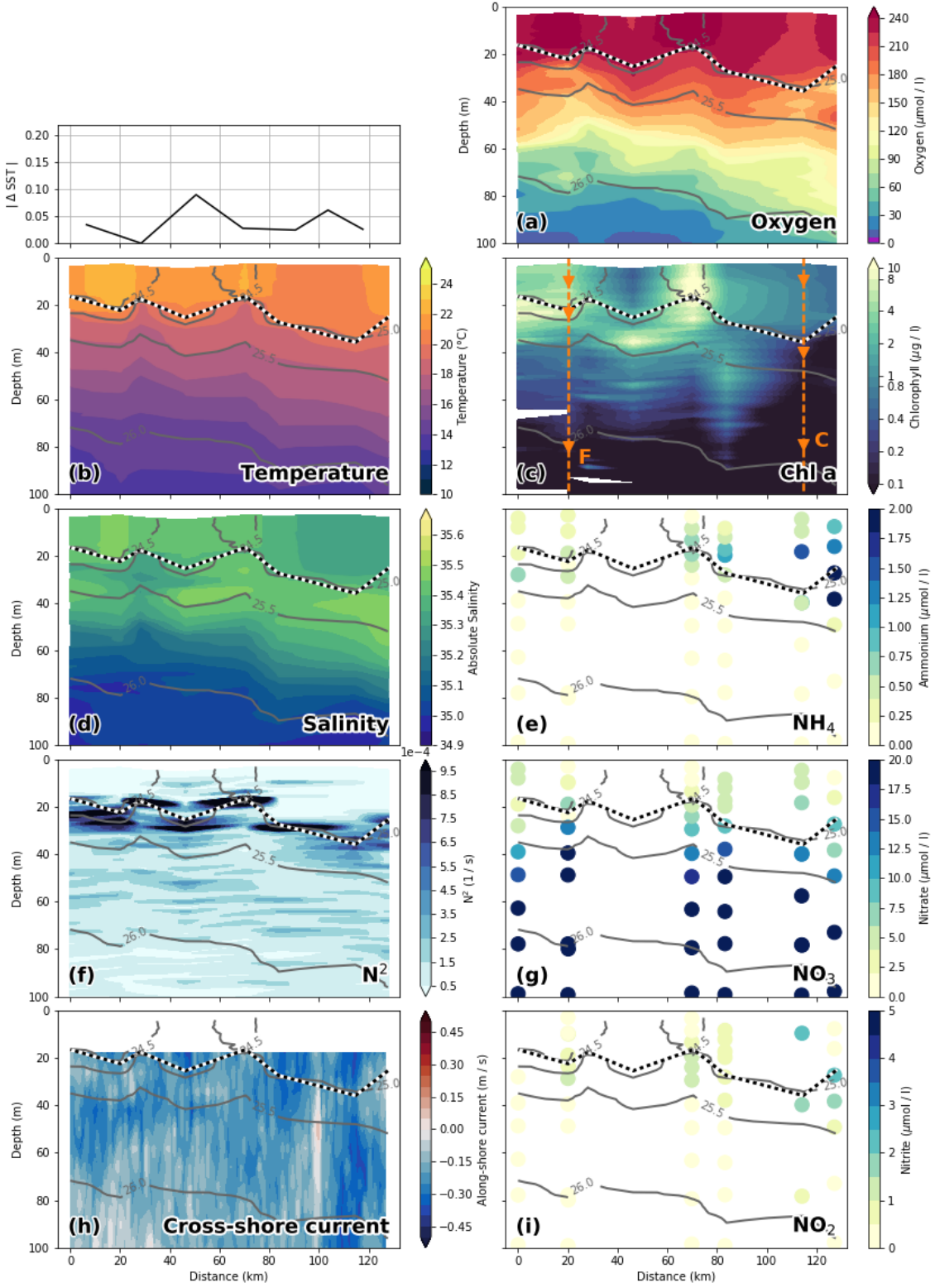


Figure 18: Along-shore transect T3BIO. The dashed orange lines and orange triangles in (c) mark the "C - cold" and "F - front" stations where primary production was measured (Fig. 16) and the respective sampling depths. All other elements as in Figure 14.

6 Representation of filaments in biogeochemical model simulations

To gain trust in quantifications of submesoscale effects based on models and assess the associated uncertainties as well as possible systematic biases, it is necessary to evaluate the biogeochemical models on synoptic timescales and verify that they can reproduce observed patterns in the biogeochemical fields. Filaments of different lateral scale, horizontal and vertical structure and offshore extent exist in the models which makes quantitative comparison difficult. Moreover, the position and shape of the filaments is determined by the mesoscale eddy field which differs between observations and simulations. We therefore picked filaments in the $1/45^\circ$ simulations (PISCES45, BioEBUS45) that were as close as possible in space and time to the observations, which were then taken to be as representative as possible.

6.1 PISCES

A filament that was present on April 5, 2017 in the PISCES45 simulation is visible in surface maps of temperature (Fig. 19-a), chlorophyll α (Fig. 19-b) and nutrients (Fig. 19-d,e). The dominant feature is the large cross-shore temperature gradient between the cold (16°C) coastal upwelling region and warmer (23°C) offshore waters (Fig. 19-a). Two separate filament structures originating in the upwelling patches near Pisco and Nazca are present. Chlorophyll α concentrations range between 8 mg m^{-3} near the coast and 0.1 mg m^{-3} offshore (Fig. 19-b). Ammonium ranges between $2 \mu\text{mol l}^{-1}$ within the coldest water of the upwelling patch to $< 0.2 \mu\text{mol l}^{-1}$ offshore (Fig. 19-d).

In the following, the physical and biogeochemical variability on a vertical cross-shore transect is analyzed in order to characterize the general structure of the upwelling (T1PISCES; Fig. 20; dashed line in Fig. 19). Temperature within the mixed-layer decreases with distance from the coast from 16°C on the shelf to 24.5°C offshore (Fig. 20-b). One exception is a local temperature minimum at ~ 80 km offshore, coinciding with a locally increased

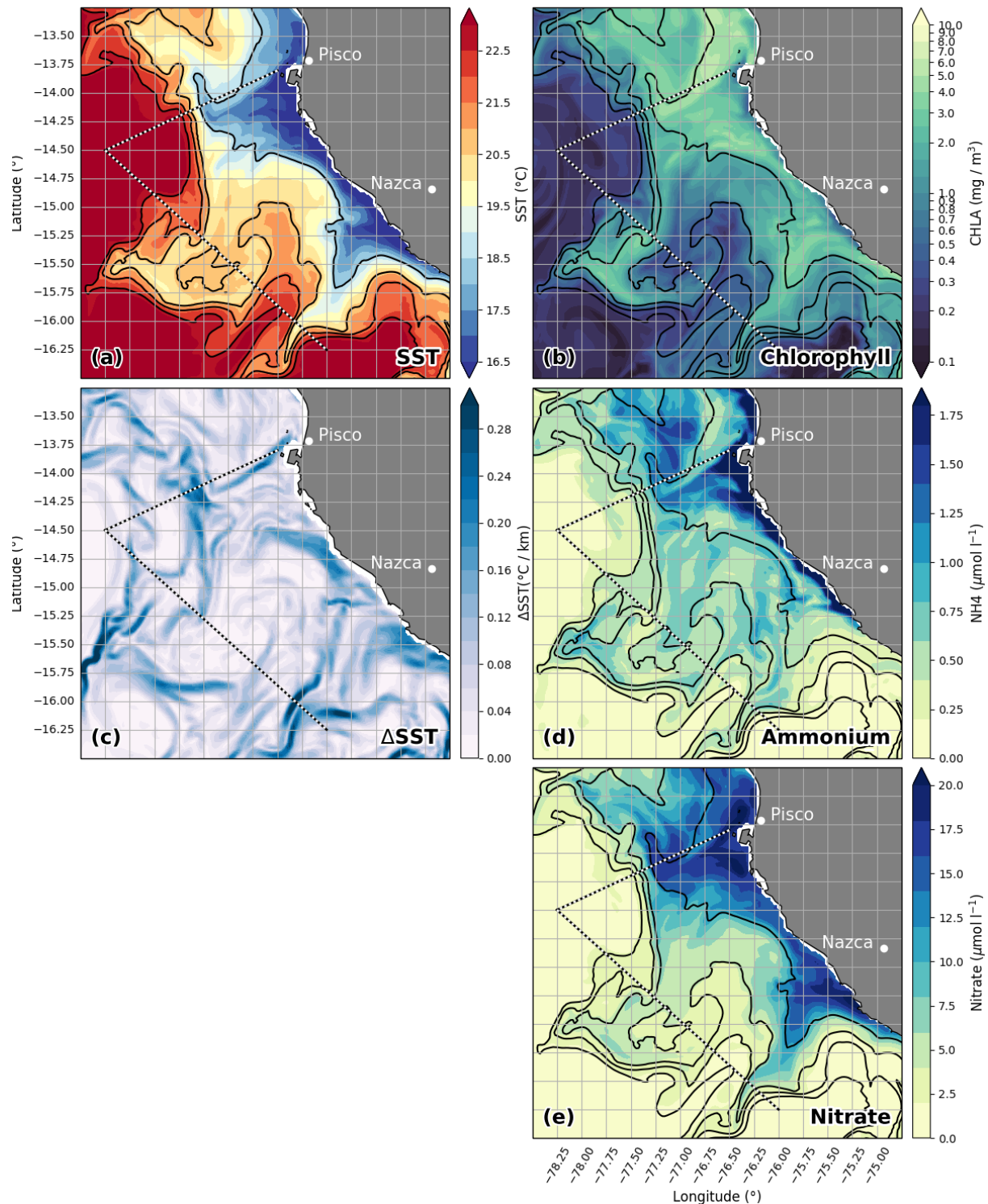


Figure 19: 4-hour averaged surface fields of (a) temperature (b) chlorophyll α (c) absolute SST gradient (d) ammonium and (e) nitrate on April 5, 2017 in the PISCES45 simulation. Black contours in (a-e) represent isotherms.

mixed-layer depth by ~ 10 m and a pronounced minimum in stratification at the base of the mixed-layer (Fig. 20-f). This local temperature minimum corresponds to the small filament structure that extends northward from the upwelling patch near Pisco at 14°S / 77.25°W (Fig. 19-a). A strong horizontal velocity shear (0.6 m s^{-1} / 20 km) between northward flow offshore and southward flow inshore is present across the axis of the filament. The upwelling front is located 100 km offshore and marked by a ΔSST maximum of $0.2 \text{ }^{\circ}\text{C km}^{-1}$ (Fig. 20-b, top panel; 19c). The along-shore current is southward inshore of the front with a maximum (-0.3 m s^{-1}) at 100 m depth and predominantly northward on its offshore side with a maximum (0.45 m s^{-1}) at the surface. Southward velocities (0.1 m s^{-1}) are present in the ML at a local minimum in ΔSST 150 km offshore, resulting in a velocity shear of 0.2 m s^{-1} / 20 m across the base of the ML (Fig. 20-h). The temperature at 100 m depth is 15°C at 200 km offshore and 13°C on the shelf. Salinity shows its maximum (35.55 g kg^{-1}) in the offshore surface waters and decreases both with depth and towards the coast, the minimum is found at 100 m depth, 150 km offshore (Fig. 20-d). The vertical salinity gradient increases with distance from the coast from a 0.05 g kg^{-1} change over the top 100 m on the shelf to 0.5 g kg^{-1} offshore. A local salinity maximum of 35.55 g kg^{-1} is found at 125 km from the coast, just offshore of the main upwelling front. The maximum southward velocities (0.35 m s^{-1}) at 60 km and 90 m depth coincide with a local salinity minimum (35 g kg^{-1}), indicating the influence of ESSW that is advected southward near the shelf. Chlorophyll α decreases offshore from 7 mg m^{-3} on the shelf to $< 0.1 \text{ mg m}^{-3}$ at 175 km cross-shore distance (Fig. 20-c). The near-shore maximum coincides with pronounced surface minima in NO_3^- and NH_4^+ (Fig. 20-e,g). Chl α concentrations below 40 m are very low ($< 0.1 \text{ mg m}^{-3}$) within 75 km from the coast, but up to 0.5 mg m^{-3} offshore, following the 25.5 kg m^{-3} isopycnal downward to a depth of > 80 m. Below the small filament 80 km offshore, high concentrations of $> 1 \text{ mg m}^{-3}$ extend as far down as 60 m. Nitrate concentrations are maximum ($> 20 \mu\text{mol l}^{-1}$) at 100 m depth everywhere along the transect and minimum ($< 2 \mu\text{mol l}^{-1}$) offshore at the surface (Fig. 20-e). Surface NO_3^- concentrations are elevated ($10 - 20 \mu\text{mol l}^{-1}$) within 100 km from the coast. Ammonium concentrations are elevated ($1.5 - 2.5 \mu\text{mol l}^{-1}$) between 20 m -

250 m depth within 50 km from the coast, the maximum being reached at ~ 40 m depth in the tongue that extends offshore along the 1025.5 kg m^{-3} isopycnal (Fig. 20-g). The maximum surface ammonium concentration of $1.9 \mu\text{mol l}^{-1}$ is reached within 5 km of the coast, another local maximum is located at 50 km - 100 km cross-shore distance. Oxygen concentrations are maximum ($> 240 \mu\text{mol l}^{-1}$) between 100 km - 175 km offshore, within 20 m below the mixed-layer (Fig. 20-a). Minimum O_2 concentrations ($< 15 \mu\text{mol l}^{-1}$) are found within 75 km of the coast, below 25.5 kg m^{-3} isopycnal. The area characterized by upward sloping isopycnals towards the shore coincides with the chlorophyll α minimum of the transect and high NO_3^- concentrations (Fig. 20-c, e).

Now the along-shore variability in a vertical transect across two filaments is analyzed (T2PISCES; Fig. 21; dashed line in Fig. 19). A large filament originating in the upwelling patch near Pisco bends southward in an anticyclonic structure at its tip and therefore crosses the transect twice at 120 km and 220 km distance, indicated by the outcrop of the 24.5 kg m^{-3} isopycnal. Another small filament originating near Nazca is seen at ~ 270 km, also marked by the outcropping 24.5 kg m^{-3} isopycnals.

Surface minima of temperature and salinity and maxima of chlorophyll α , nitrate and ammonium are associated with both filaments (Fig. 21b-e,g). The small filament is colder (19°C) and less saline (35.2 g kg^{-1}) in its center than the large filament (20°C , 35.25 g kg^{-1}) and associated with a stratification minimum at the base of the mixed-layer, which is not the case for the larger filament (Fig. 21f). Nitrate concentrations in the small filament are higher ($7 \mu\text{mol l}^{-1}$) compared with the large filament ($5 \mu\text{mol l}^{-1}$), while both filaments show similar ammonium concentrations of $\sim 0.7 \mu\text{mol l}^{-1}$ (Fig. 21e,g). Elevated chlorophyll α concentrations associated with both filaments are found at their edges, marked by the three locations where the 24.5 kg m^{-3} isopycnal outcrops (Fig. 21c).

The subsurface structure beneath the filaments is characterized by isopycnals doming ~ 40 m upwards, associated with a horizontal temperature minimum and homogeneous salinity of $\sim 35.1 \text{ g kg}^{-1}$ (Fig. 21b; 21d). The doming isopycnals are flanked by opposing cross-shore currents that have their maxima (0.4 m s^{-1}) at 100 m depth and are spaced

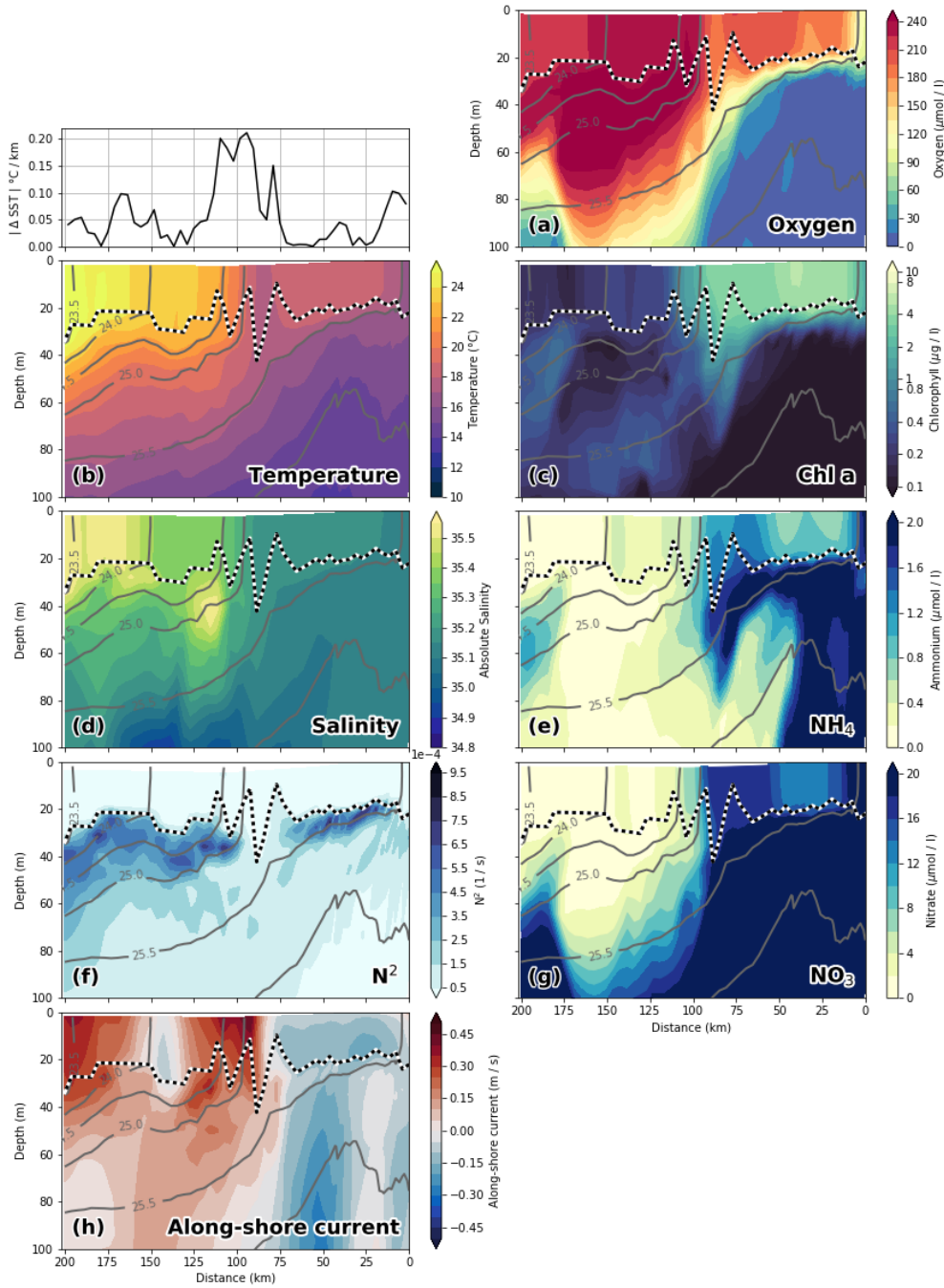


Figure 20: 4-hour averaged fields of (a) Oxygen (b) ΔSST / temperature (c) chlorophyll α (d) absolute salinity (e) ammonium (f) buoyancy frequency squared (g) nitrate and (h) along-shore current (positive northward, rotated 8° anti-clockwise from due north) on cross-shore transect T1PISCES. Grey lines are the 23.5, 24, 25.5, 25, 25.5 and 26 kg m^{-3} contours of σ_θ (potential density - 1000). The dashed black-and-white line denotes the mixed-layer depth (MLD) being defined here as the maximum of the squared buoyancy frequency N^2 .

~80 km apart, indicating the presence of an anticyclonic subsurface eddy. Both current bands extend to the surface, but only the offshore current exhibits another maximum of similar strength (0.45 m s^{-1}) in the mixed-layer, coinciding with the filament that is visible in Figure 19 and explaining its anticyclonic structure. The area of homogeneous salinity between 30 m - 90 m depth coincides with high nitrate ($20 \mu\text{mol l}^{-1}$), low oxygen ($< 15 \mu\text{mol l}^{-1}$) and high ammonium ($> 2 \mu\text{mol l}^{-1}$) concentrations (Fig. 21-a,e,g). A reduction in both nutricline and oxycline depth can be seen below the two filaments (Fig. 21-a,e). An ammonium maximum centered on the nutricline is found in places where the nutricline is shallower than 70 m depth, coinciding with subsurface Chl α maxima of $\sim 3 \text{ mg m}^{-3}$ (Fig. 21-c,e,g). The highest ammonium concentration of $3.4 \mu\text{mol l}^{-1}$ that is reached in the PISCES45 simulation is located within this shallow subsurface maximum at $\sim 30 \text{ m}$ depth. The deep ammonium maximum below the filament reaches from the mixed-layer down to 250 m depth (not shown) and the water exhibits similar salinity (35.1 g kg^{-1}), temperature ($14 - 18^\circ\text{C}$), oxygen ($< 15 \mu\text{mol l}^{-1}$) and Chl α ($< 0.2 \text{ mg m}^{-3}$) characteristics as the water on the shelf (Figs. 21; 20). It is therefore likely that this feature is not a result of local processes associated with the filament itself but was advected from its source on the shelf. The presence of an anticyclonic eddy supports this hypothesis, since mesoscale eddies are known to be effective in trapping coastal water and transporting it offshore (Thomsen et al., 2016b; José et al., 2017).

6.2 BioEBUS

Two filament structures extend from the upwelling patches off Pisco and Nazca on March 4, 2017 in the BioEBUS45 simulation, within a large cross-shore temperature gradient between 18°C near the coast and 24°C offshore (Fig. 22a). The northern filament reaches less than 100 km offshore, therefore we focus on the one originating at the coast near Nazca, which is closer in scale to the one observed. Chlorophyll α concentrations of 10 mg m^{-3} at the coast and $\sim 0.4 \text{ mg m}^{-3}$ offshore are present (Fig. 22b), with the maxima decreasing to $\sim 3 \text{ mg m}^{-3}$ within 30 km from the coast. The surface waters are almost completely depleted of nitrate and nitrite ($< 0.1 \mu\text{mol l}^{-1}$) over most of the model domain

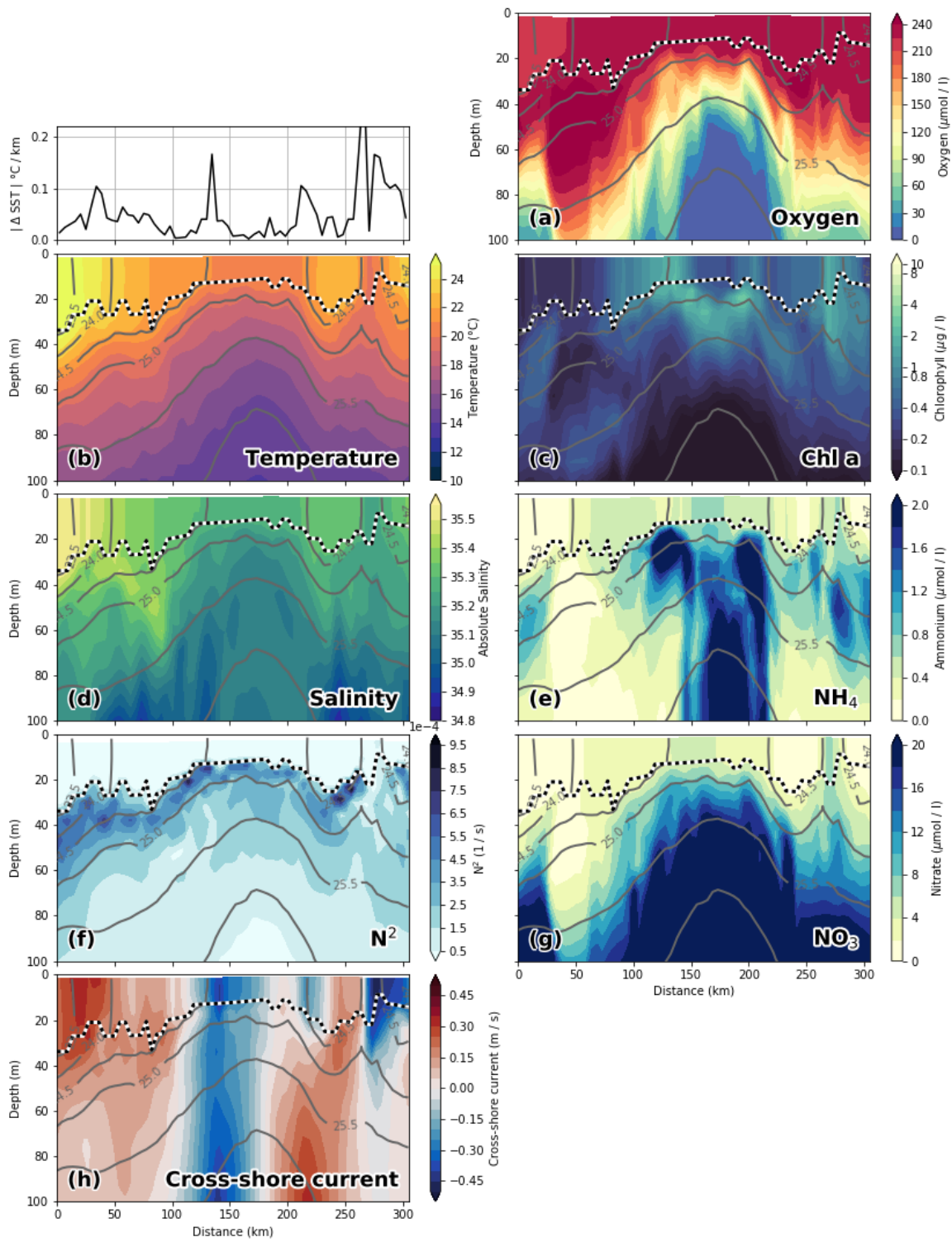


Figure 21: Along-shore transect in PISCES45 (T2PISCES). All elements as in Figure 20.

(Fig. 22e). Surface nitrate concentrations $> 10 \mu\text{mol l}^{-1}$ are only present in the upwelling patches and extend no further than $< 10 \text{ km}$ from the coast. Ammonium ranges between $< 0.02 \mu\text{mol l}^{-1}$ within the cold, recently upwelled water to $0.12 \mu\text{mol l}^{-1}$ within the southern filament (Fig. 22d).

In order to describe the general structure of the upwelling, a vertical cross-shore transect is analyzed (T1BioEBUS; Fig. 23; dashed line in Fig. 22). Surface temperature ranges from 18°C in the upwelling patch on the shelf to 24.5°C offshore (Fig. 23b). A high maximum stratification of $> 9.5 \times 10^{-4} \text{ s}^{-1}$ is found at the base of the mixed-layer (Figs. 23f). This maximum is only present offshore and the maximum stratification is weaker ($4.5 - 6.5 \times 10^{-4} \text{ s}^{-1}$) within 100 km from the coast. Surface oxygen concentrations of $> 240 \mu\text{mol l}^{-1}$ near the coast and a shallow oxycline with depths ranging from 20 m at the coast to 70 m offshore are present (Figs. 23a). Oxygen-depleted waters ($< 15 \mu\text{mol l}^{-1}$) are found on the shelf within 100 km from the coast (Fig. 23a). High chlorophyll α concentrations ($\sim 10 \text{ mg m}^{-3}$) are locally confined to a 30 km wide coastal band and Chl α concentrations of $> 0.3 \text{ mg m}^{-3}$ are present down to 100 m depth everywhere along the transect (Fig. 23c). The nutricline coincides with the oxycline and the 1025.5 kg m^{-3} isopycnal and lies at $\sim 80 \text{ m}$ depth offshore (Figs. 23g). The mixed-layer is largely depleted of nitrate and nitrite with combined concentrations of $< 0.1 \mu\text{mol l}^{-1}$ along most of the section. However, the nutricline outcrops $< 5 \text{ km}$ from the shore and surface nitrate concentrations increase to $\sim 15 \mu\text{mol l}^{-1}$ at the coast (Fig. 23g,h). Nitrite concentrations are elevated ($1 - 4 \mu\text{mol l}^{-1}$) on the shelf below the nutricline (Fig. 23h). This maximum extends $\sim 100 \text{ km}$ offshore and its boundary coincides with the $60 \mu\text{mol l}^{-1}$ oxygen contour. Local nitrite maxima ($1 - 1.5 \mu\text{mol l}^{-1}$) are found further offshore around the nutricline. Surface nitrite shows concentrations of $< 0.1 \mu\text{mol l}^{-1}$ over most of the section and only increases to $\sim 2 \mu\text{mol l}^{-1}$ within 10 km from the shore. Ammonium exhibits a distinct maximum of $0.2 \mu\text{mol l}^{-1}$ at 15 m depth 20 km from the coast, just below the surface Chl α maximum where ammonium concentrations are $< 0.04 \mu\text{mol l}^{-1}$ (Fig. 23-e). A tongue of elevated ammonium levels extends offshore from this maximum along the 1025.5 kg m^{-3}

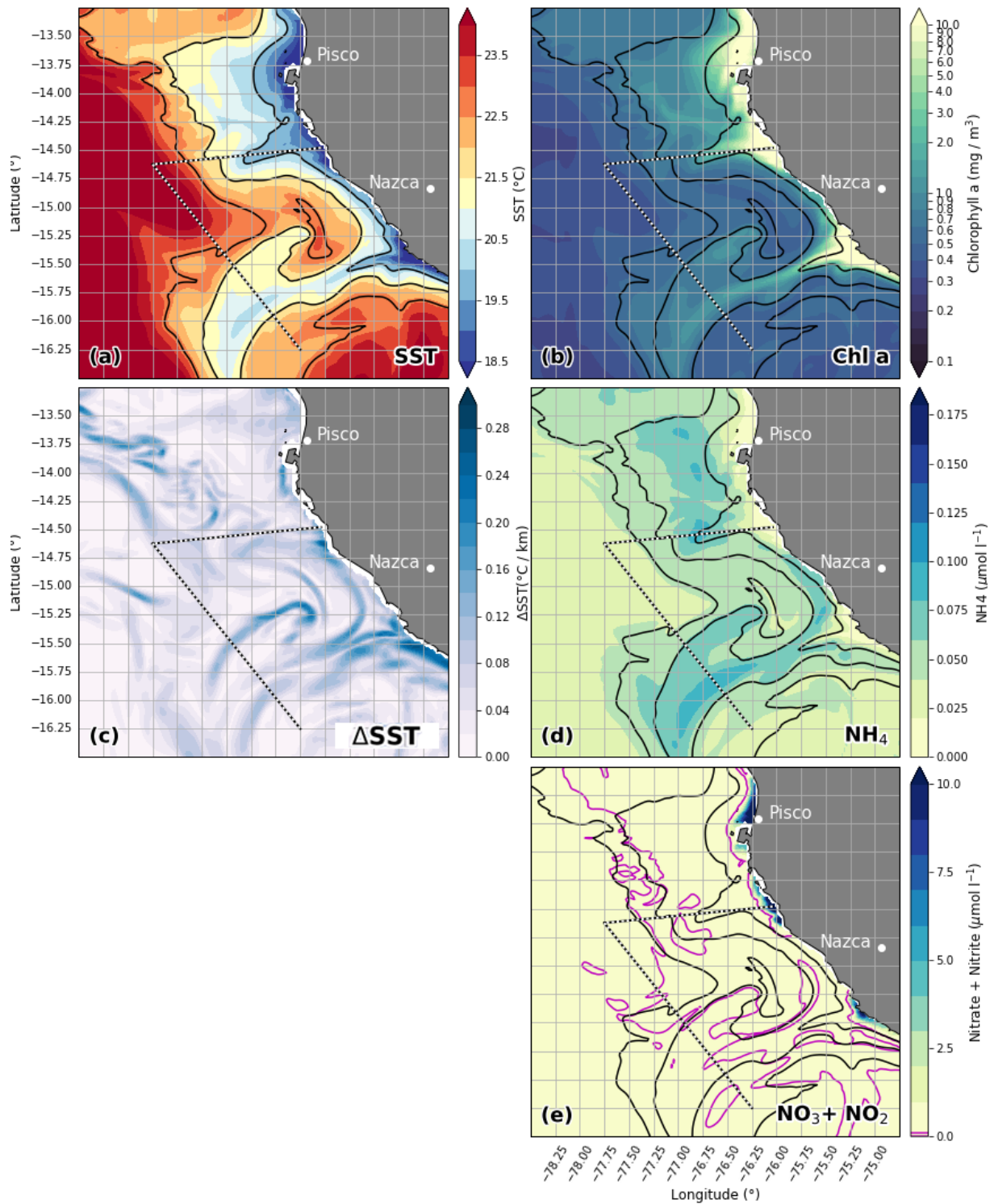


Figure 22: Daily average surface fields in BioEBUS45 on March 4, 2017. The magenta line indicates concentrations of $< 0.1 \mu\text{mol l}^{-1}$ for NO_3^- and NO_2^- combined. All other elements as in Figure 19.

isopycnal, where a local maximum ($0.12 \mu\text{mol l}^{-1}$) with a distinct surface expression of $0.1 \mu\text{mol l}^{-1}$ is found 80 km from the coast. Surface ammonium concentrations increase with cross-shore distance towards this local maximum and decrease beyond that (Figs. 23-e; 22-d).

Now the along-shore variability associated with the filament is analyzed (T2BioEBUS; Fig. 24; dashed line in Fig. 22). Surface minima of temperature (20°C) and salinity (35.1 g kg^{-1}) and maxima of chlorophyll α (1 mg m^{-3}) and ammonium ($0.1 \mu\text{mol l}^{-1}$) are associated with the filament (Fig. 24b-e,g; 22-a,b,d). The filament exhibits no substantial nitrate or nitrite maxima and their concentrations combined are $< 0.5 \mu\text{mol l}^{-1}$. A chlorophyll α maximum of 1.5 mg m^{-3} is located in the center of the filament (Fig. 21-c; 24-c). The subsurface structure below the filament is characterized by doming isopycnals, concomitant with a salinity minimum (34.9 g kg^{-1}) and a shallowing of the oxycline and nutricline by 20 - 30 m (Fig. 24-a,g,h). The shallower nutricline is still located 10 m below the mixed-layer, therefore this shallowing does not affect surface concentrations of NO_3^- and NO_2^- . A subsurface ammonium maximum of $0.1 - 0.15 \mu\text{mol l}^{-1}$ is present at 20 - 40 m depth below the filament, extends ~ 20 km to its sides and has surface expression of $0.1 \mu\text{mol l}^{-1}$ (Fig. 24-e). Nitrite levels below the filament are elevated ($2.5 \mu\text{mol l}^{-1}$) between the nutricline and 100 m depth and similar to the conditions on the shelf, coinciding with an offshore current of $0.2 - 0.4 \text{ m s}^{-1}$ and thus suggesting offshore advection of near-shore characteristics (Figs. 23-h; 24-h).

6.3 Comparison and synthesis of observed and modeled filament characteristics

The filaments that were observed in the PISCES45 (Fig. 19) and BioEBUS45 (Fig. 22) simulations are similar in size and structure to the observed cold filament, which had an offshore extent of 150 km - 200 km (Fig. 12). Similar to the satellite images, the simulated surface fields of SST and Chl α show two separate filament structures, originating in the upwelling patches off Pisco and Nazca (Fig. 19-a,b; Fig. 22-a,b).

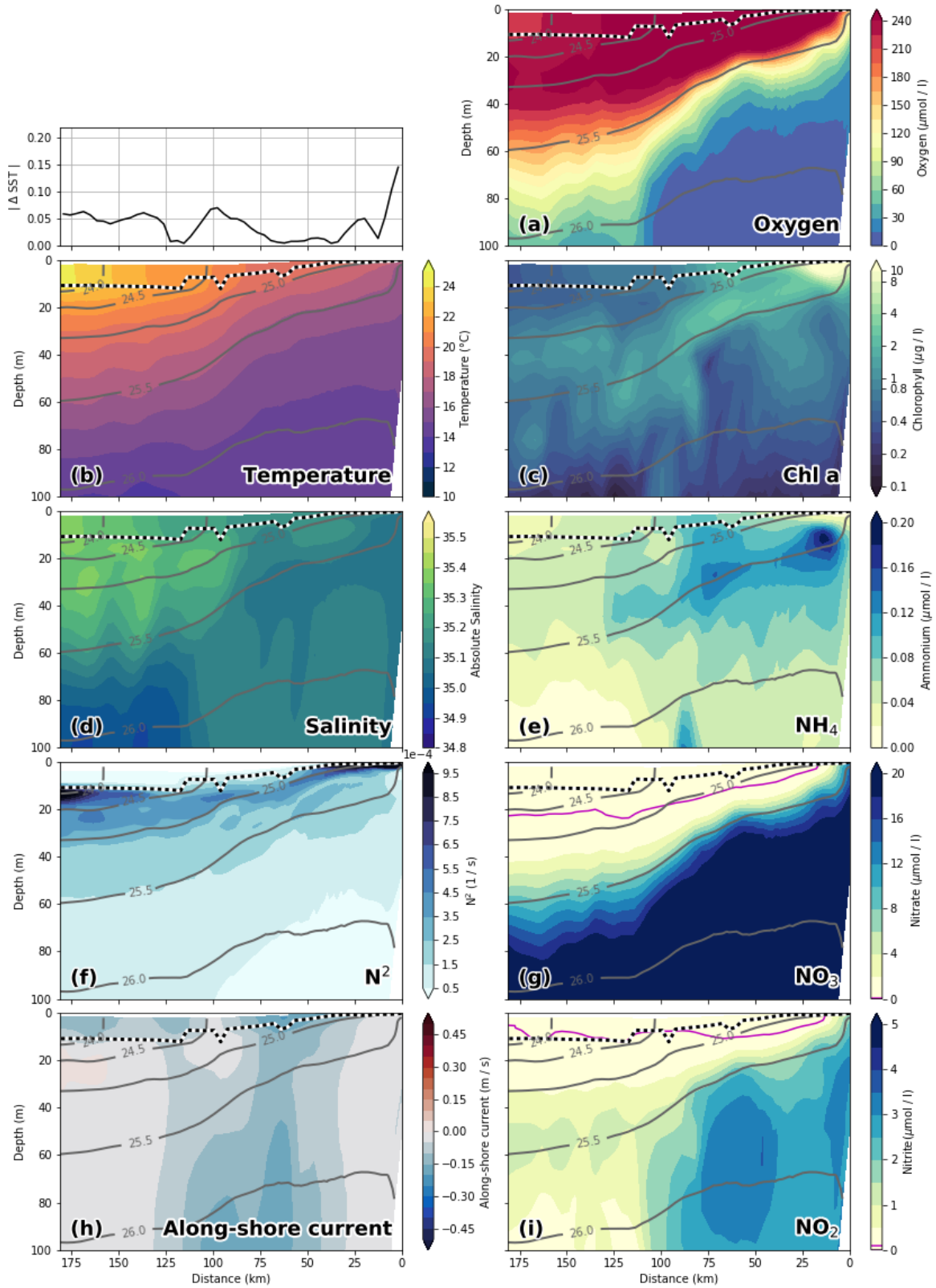


Figure 23: Across-shore transect in BioEBUS45 (T1BioEBUS), 1-day average. The magenta contour line in (g) / (h) marks $\text{NO}_3^- / \text{NO}_2^-$ concentrations $< 0.1 \mu\text{mol l}^{-1}$. All other elements as in Figure 20.

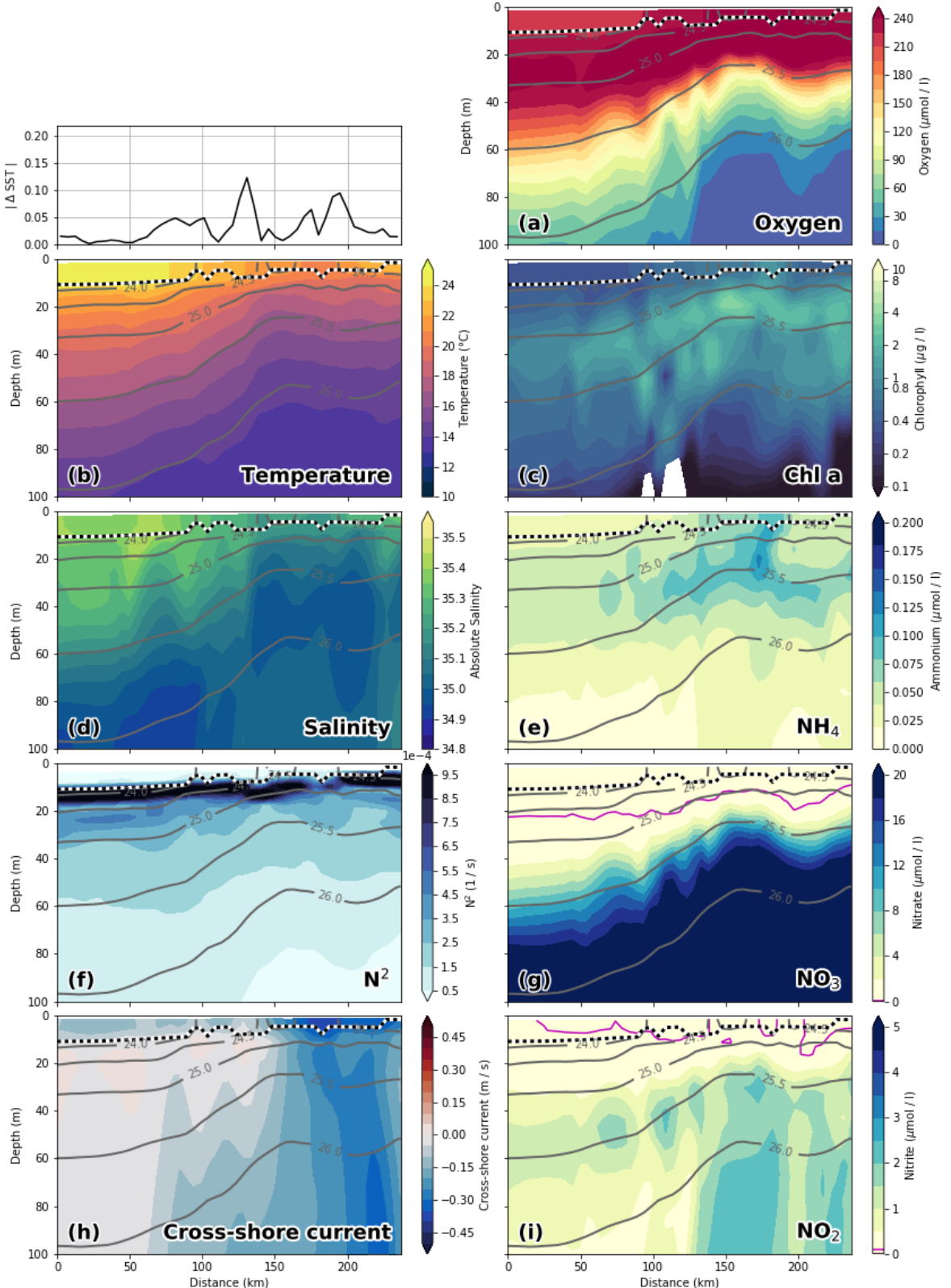


Figure 24: Along-shore transect in BioEBUS45 (T2BioEBUS), 1-day average. The magenta contour line in (g) / (h) marks $\text{NO}_3^- / \text{NO}_2^-$ concentrations $< 0.1 \mu\text{mol l}^{-1}$. All other elements as in [Figure 20](#).

The temperature and salinity distributions and horizontal gradients are similar overall to observations in both simulations. The location of the upwelling front 100 km offshore and the corresponding ΔSST maximum of $0.2 \text{ }^{\circ}\text{C km}^{-1}$ agree well with satellite images and in-situ measurements. However, the vertical gradients and thus the stratification is too low by almost a factor of two. This is indicated by the maximum buoyancy frequency squared (N^2) being $5.5 \times 10^{-4} \text{ s}^{-1}$ in the PISCES45 simulation (Fig. [20]-f) compared to $> 9.5 \times 10^{-4} \text{ s}^{-1}$ in the observations (Fig. [14]-f). N^2 values comparable to those observed ($> 9.5 \times 10^{-4} \text{ s}^{-1}$) are present locally in BioEBUS45 and not in PISCES45, but stratification is still too low overall (Fig. [20]-f). The higher N^2 values in BioEBUS45 are likely related to the seasonal cycle and mismatch of one month, as in a similar filament in April 2016 (not shown) N^2 values are similar to the PISCES simulation. The mixed-layer depth in PISCES45 is $\sim 20 \text{ m}$ (Fig. [20]), very close to observed values offshore of $\sim 100 \text{ km}$ (Fig. [14]). Small-scale variability, like the local deepening of the mixed-layer by $\sim 10 \text{ m}$ within the narrow filament structure 80 km offshore in T1PISCES (Fig. [20]-b), very similar to the structure 40 km offshore in the cross-shore transect T1 (Fig. [14]-b), is reproduced. However, the observed mixed-layer depth decreases to only $\sim 5 \text{ m}$ in the coastal upwelling patch, which is not seen in the PISCES45 simulation (Fig. [20]). In BioEBUS45, the mixed-layer depth on the chosen sections is between 5 m - 10 m everywhere (Fig. [23]), which can be largely explained by the mismatch of one month and a pronounced seasonal cycle since in a similar filament in April 2016 MLD values are similar to the PISCES simulation (not shown). However, the MLD might also be influenced by the different mixed-layer parameterizations in PISCES45 and BioEBUS45.

The southward velocities of $\sim 0.3 \text{ m s}^{-1}$ inshore of the upwelling front that are associated with the surfacing undercurrent are similar to observations in PISCES45 (Fig. [20]-h; [20h]). In BioEBUS45 this flow is weaker (0.2 m s^{-1}) and even slightly northward near the coast, which is likely related to mesoscale differences between both simulations and the observations (Fig. [23]-h).

The modeled oxycline depth of 30 m - 110 m (Figs. [20]-a; [23]-a) agrees reasonably well with the observed depths of 30 m - 90 m (Figs. [14]-a; [17]-a; [18]-a) and shows variability on

similar scales. However, a very shallow oxycline is observed in the upwelling patch within 20 km from the shore (Fig. 14a), where O_2 concentrations drop to $< 45 \mu\text{mol l}^{-1}$ just a few meters below the surface and $< 5 \mu\text{mol l}^{-1}$ at 20 m depth. This is not reproduced in either of the two simulations, where O_2 concentrations at the coast are $100 \mu\text{mol l}^{-1}$ and $> 240 \mu\text{mol l}^{-1}$ in PISCES45 and BioEBUS45, respectively. Oxygen concentrations of $< 5 \mu\text{mol l}^{-1}$ are only reached at the core depth of the oxygen minimum zone (200 m - 300 m) in the simulations (not shown). The effect of filaments on the oxycline depth seems to be different in observations and models. Below a filament, observations show a deepening oxycline (Fig. 17a) while in the simulations the oxycline shallows (Fig. 21-a; 24a). Advection along opposite cross-shore gradients in the observations (Fig. 14a) and simulations (Fig. 20a; 23a) is a plausible explanation for this difference.

Chlorophyll α concentrations of $> 0.2 \text{ mg m}^{-3}$ are found down to 80 m / 100 m depth in the observations / simulations, showing overall good agreement with a small bias towards greater depths similar to oxygen (Fig. 20c; 20c; 23c). Maximum surface Chl α of $> 10 \text{ mg m}^{-3}$ in the observations and $8 \text{ mg m}^{-3} / 10 \text{ mg m}^{-3}$ in the PISCES45 / BioEBUS45 simulations also matches reasonably well. However, the cross-shore and vertical gradients of surface Chl α reveal notable differences between the observations and the PISCES45 and BioEBUS45 simulations: Local maxima of up to 10 mg m^{-3} are present along the nutricline and at the upwelling front $> 100 \text{ km}$ offshore in the observations, while Chl α concentrations in the simulations are inversely related with SST, decrease almost continuously offshore and with depth and no such maxima are seen (Fig. 14c; 12b; 19b; 22c). This is most obvious in BioEBUS45, where high Chl α concentrations are only present in a narrow coastal band of $\sim 30 \text{ km}$ and decrease rapidly with cross-shore distance. Lastly, it is a common feature in satellite images of chlorophyll α that concentrations remain relatively low ($< 1 \text{ mg m}^{-3}$) in recently upwelled waters near the coast (30 - 50 km) and only increase to $> 3 \text{ mg m}^{-3}$ outside the upwelling patches (Fig. 12). This is to some degree apparent in the PISCES45 simulation, but only within a much narrower ($\sim 10 \text{ km}$) region along the coast (Fig. 19b). In BioEBUS45 actually the highest Chl α concentrations are found precisely at these locations, in strong disagreement with

the observations (Fig. 22b).

The observed nutricline - here defined as the $10 \mu\text{mol l}^{-1}$ nitrate contour - is located between 20 m - 50 m depth in the open ocean and intersects the surface near the coast where upwelling occurs (Fig. 14g). The modeled nutricline is locally 100 m deep in the open ocean in PISCES45 and also reaches the surface near the coast. Surface nitrate concentrations of $< 0.1 \mu\text{mol l}^{-1}$ in BioEBUS45 over most of the model domain reveal a substantial negative bias compared with observed values of $< 20 \mu\text{mol l}^{-1}$ (Fig. 14g; 24e; 22e). This is especially striking near the coast where elevated nitrate concentrations extend no further than 10 km offshore, and in the center of the filament where in contrast to observations no surface nitrate maxima are discernible and concentrations are often $< 0.1 \mu\text{mol l}^{-1}$ (Figs. 23e; 24e). Surface nitrate maxima of $\sim 5 \mu\text{mol l}^{-1}$ associated with filaments in PISCES45 are comparable in magnitude to the observations.

Observed nitrite concentrations are highest ($5 \mu\text{mol l}^{-1}$) in the oxygen-depleted waters ($< 2 \mu\text{mol l}^{-1}$) on the shelf between 40-80 m depth and within 40 km from the coast. Nitrite concentrations of up to $1.5 \mu\text{mol l}^{-1}$ are present within 60 km from the shore and locally along the nutricline. The BioEBUS45 simulation reproduces the pattern of elevated nitrite on the shelf below ~ 20 m depth, although maximum concentrations of $3.5 - 4 \mu\text{mol l}^{-1}$ are slightly lower compared with the observed $5 \mu\text{mol l}^{-1}$. The offshore extent of this maximum is given by the location where the oxycline drops to these depths, which is twice as far from the coast as in the observations at 100 km. Also seen in the simulation are local maxima of $1.5 - 2 \mu\text{mol l}^{-1}$ along the nutricline further offshore. Elevated surface nitrite concentrations within tens of kilometers from the shore are not present, which is likely related to the general low bias at the surface in the BioEBUS45 simulation.

Besides the fact that filaments are local ammonium maxima in observations and both biogeochemical models, also strong discrepancies exist between observations and simulations. Surface ammonium concentrations in the PISCES45 simulation are $\sim 2 \mu\text{mol l}^{-1}$ near the coast and decrease offshore, in good agreement with the observed maxima. Surface ammonium concentrations in BioEBUS45 are $< 0.02 \mu\text{mol l}^{-1}$ near the coast and $0.2 \mu\text{mol l}^{-1}$ at

local maxima between 50 km - 150 km offshore, an order of magnitude lower compared with the measurements. While a continuous decrease in cross-shore direction of surface ammonium is suggested by transect T1 (Fig. 14), the absolute maximum of all measurements is not found near the coast but in the center of the filament ~150 km offshore. Observed surface ammonium is inversely related with chlorophyll α (Fig. 14-c,g; 17-c,g; 18-c,g). This applies along the axis of the filament in particular, where ammonium (Chla) concentrations inside the filament are higher (lower) on transect T3 (Fig. 18-c,g) than on transect T2 (Fig. 17-c,g) and thus ammonium increases offshore. While inverse relationship between ammonium and Chl α is seen to varying degrees in both simulations, only BioEBUS45 clearly shows increasing (decreasing) ammonium (Chl α) concentrations along the filament axis (Fig. 19-b,d; 20-c,g; 22-b,d; 23-c,g). Higher subsurface than surface ammonium concentrations are seen in both simulations (Fig. 20-g; 23-g) with maxima frequently located near the nutricline, in agreement with some of the observations (Fig. 14-g). In the filament, however, observed ammonium concentrations were very high ($1 - 2 \mu\text{mol l}^{-1}$) within the mixed-layer and low ($< 0.2 \mu\text{mol l}^{-1}$) just beneath (Fig. 17-g). This very distinct vertical structure of ammonium is never present in the simulations, which may be related to the insufficient stratification and excessive diffusion across the base of the mixed-layer. The subsurface ammonium maximum in PISCES45 reaches all the way down to the seafloor within 100 km from the coast, weaker maxima around the nutricline in addition to the deep maxima are present further offshore (Fig. 20-g; 21-g). The maximum ammonium concentration in the PISCES45 simulation of $3.4 \mu\text{mol l}^{-1}$ is found offshore, 10 m below the mixed-layer. The subsurface ammonium maximum in the BioEBUS45 simulation is centered around the nutricline at 20 m - 60 m depth (Figs. 23-g; 24-g), resembling observed patterns (Fig. 14-g). In contrast, large volumes of high ammonium waters over several hundred meters depth like in the PISCES45 simulation are in strong disagreement with the observations presented here.

It can be concluded that the high-resolution ($1/45^\circ$) simulations exhibit filaments that are similar in lateral scale, horizontal and vertical structure and offshore extent to those

observed. Biogeochemical variables and especially nutrients however show substantial differences in both magnitude and gradients. Enhanced surface nitrate concentrations associated with filaments are seen in PISCES45 but not in BioEBUS45, where the surface is depleted of nitrate further than 20 km from the coast. While both models show enhanced ammonium concentrations at filament locations, these are unrealistically deep and too high in PISCES45 and an order of magnitude too small in BioEBUS45. Disregarding the error in absolute values, both vertical and the cross-shore gradients of ammonium appear more realistic in BioEBUS than in PISCES. The observed cross-shore gradient of surface Chl α is approximately reproduced in models, but small scale features like frontal maxima and near-shore minima in the upwelling patches are missing.

7 Discussion

In the previous chapters we characterized the physical and biogeochemical variability associated with a cold filament near 15°S off Peru (Sec. 5) and compared it with the representation in two submesoscale-permitting biogeochemical model simulations (Sec. 6). We will now put our biogeochemical observations in a broader context of the existing research on the Peru upwelling near 15°S and go on to discuss the variability of primary production and the possible explanations for the low chlorophyll α and simultaneously high primary production that was observed in the core of the filament (Sec. 7.1). The first main question of how the biogeochemistry of filaments is represented in the submesoscale-permitting models is addressed (Sec. 7.2) and causes of the apparent differences between the PISCES and BioEBUS simulations are elucidated. Finally, the effect of submesoscale processes on the biogeochemistry of the Peru upwelling will be discussed (Sec. 7.3), which answers the second main question.

7.1 Variability of chlorophyll and primary production in the Peru upwelling

The early studies that focused on the persistent upwelling near 15°S were described in section 2 and we will use them here to relate our measurements to earlier observations in the same area. Nitrate concentrations of $\sim 20 \mu\text{mol l}^{-1}$ within the coastal upwelling center and $5 \mu\text{mol l}^{-1}$ offshore were commonly observed, in good agreement with our observations and thus indicating that typical biogeochemical conditions were present during the filament survey in our study. High surface ammonium concentrations ($1.2 - 3 \mu\text{mol l}^{-1}$) at 50 - 200 km offshore distance were also reported by several authors (Whitledge, 1981; Macisaac *et al.*, 1985; Kalvelage *et al.*, 2013) indicating that the NH_4^+ maxima seen in our study are not an exception but apparently a rather common phenomenon in the area. It is especially noteworthy that the NH_4^+ maximum observed by Kalvelage *et al.* (2013) (their supplementary Figure 1f) is located at 16°S / 77.5°W about 200 km offshore of Pisco, precisely where the cold filament in our study was observed.

7.1 Variability of chlorophyll and primary production in the Peru upwelling

We outlined in section 2 the three main explanations that were proposed over the years to contribute to high-nutrient, low-chlorophyll (HNLC) conditions in the upwelling and generally in the eastern tropical Pacific, which were: (1) A time lag of phytoplankton growth after upwelling ([Armstrong et al., 1967](#); [Boyd and Smith, 1983](#); [Macisaac et al., 1985](#)), (2) grazing pressure by herbivorous zooplankton ([Minas et al., 1974](#); [Walsh, 1976](#); [Whitledge, 1981](#)) and (3) nutrient limitation of phytoplankton growth by a lack of silica ([Nelson et al., 1981](#)) or iron ([Hutchins et al., 2002](#); [Bruland et al., 2005](#)).

The observed cold filament described in this study (Sec. 5) also exhibited high nitrate and low chlorophyll concentrations in its core but enhanced Chl α at the front separating it from the warm offshore waters (Fig. 17). The same pattern was observed by [Hosegood et al. \(2017\)](#) in a similar filament (150 km offshore extent, 0.4 m s^{-1} offshore velocity) off Mauritania, suggesting that it may be a more general feature of cold filaments. Furthermore, high surface ammonium concentrations ($1 - 2 \mu\text{mol l}^{-1}$) were present in the filament, suggesting that remineralization of organic matter dominates primary production in the recently upwelled water. However, high primary production ($240 \text{ mmol C m}^{-2} \text{ d}^{-1}$) observed at the same location indicates that limitation of phytoplankton growth by a lack of iron or silica is not the reason for the low chlorophyll α concentrations, since neither nutrient was added during the incubations. A relatively long timescale of phytoplankton growth or zooplankton grazing therefore remain as the two possible explanations for the observed low Chl α concentrations. Arguments in favor of one or the other hypothesis will be presented in the following.

We first consider the possibility that the low Chl α concentrations are due to slow initial phytoplankton growth after upwelling. [Macisaac et al. \(1985\)](#) found the duration of a phytoplankton bloom in the PCUS to be 8–10 days. Maximum offshore velocities of up to $\sim 45 \text{ km d}^{-1}$ in the cold filament (Fig. 15g) indicate a minimum advection timescale from the coastal upwelling to the sampling location of ~ 3 days, suggesting that our measurements may still reflect an early stage of the bloom. In this case, we would expect Chl α and PP to increase during the days following the sampling of the filament. In Satellite estimates of primary production during the week before (Fig. 25a) and after (Fig. 25b)

the filament sampling, an increase in PP by $\sim 50\%$ at the location of the cold filament is discernible, indicating that Chl α concentrations continued to increase after our measurements. However, the westward movement of distinct features between both images in combination with high offshore velocities (0.5 m s^{-1}) in the filament also suggest offshore advection of phytoplankton instead of phytoplankton growth as a possible explanation for this increase.

The second possible explanation for the Chl α minimum in the filament is zooplankton grazing. High rates of zooplankton grazing are concomitant with substantial amounts of ammonium excretion that can be an important source of nitrogen for regenerated production (*Pérez-Aragón et al.*, 2011). Ammonium is preferred by phytoplankton over nitrate as a nitrogen source (*Dugdale and Goering*, 1967) and is usually taken up at the rate at which it is produced by remineralization (*Glibert*, 1982). However, remineralization rates often exceed uptake rates in coastal waters (*Harrison*, 1978). Further offshore, it is conceivable that due to high physical variability imposed by fronts and filaments, nutrient regeneration and uptake by producers and consumers become decoupled in space and time, allowing for an accumulation of ammonium to occur when regeneration locally exceeds the demand by phytoplankton (*Alcaraz et al.*, 1994). The high ammonium concentrations observed in the filament can therefore be seen as circumstantial evidence in favor of the zooplankton grazing hypothesis. An objection to this reasoning might be that zooplankton occurs in high abundances only in the near-shore region on the shelf. However, evidence to the contrary is presented in several studies: *Boyd and Smith* (1983) analyzed surface zooplankton abundances off Peru and found that zooplankton maxima were located offshore and downstream of areas with enhanced Chl α concentration, suggesting a temporal evolution of phytoplankton growth and zooplankton grazing. *Mackas et al.* (1991) and *Keister et al.* (2009) studied filaments off California and identified changes in zooplankton community structure and spreading of zooplankton biomass into the open ocean associated with the filaments, which in some cases resulted in even higher zooplankton biomass offshore than on the shelf. *Ayón et al.* (2008) note in their review of zooplankton research off Peru that maxima in zooplankton abundance and biomass are often found in

7.1 Variability of chlorophyll and primary production in the Peru upwelling

our study area between 14°S - 16°S and that species composition and biomass can vary on short timescales due to advection. Summarizing, the literature suggests it is plausible that the Chl α minimum and NH $_4^+$ maximum observed in the filament are related to zooplankton grazing and excretion, respectively. The timescale of phytoplankton growth and offshore advection may also contribute to the observed variability of Chl α and NH $_4^+$. This warrants a more thorough investigation of zooplankton abundance and community structure within filaments.

Primary production was measured during the filament survey (Sec. 3) at three stations: In the cold filament, at the upwelling front and in the warm offshore waters, each station representing a distinctly different dynamical regime (Fig. 16). Surface PP between 2.6-9.9 $\mu\text{mol C l}^{-1} \text{d}^{-1}$ is observed at these stations, slightly lower than but with a similar spread as the results of Dengler (1985) who identified a range of 4-16 $\mu\text{mol C l}^{-1} \text{d}^{-1}$ during April-June 1976 in the same upwelling center near 15°S. Chlorophyll α and PP at the three stations exhibited strong differences in the vertical profiles, with the maximum PP occurring at the surface in the cold filament and just below the mixed-layer at the warm water station, while the upwelling front resembled a mixture of both types. The different vertical distributions can be related to the surface nitrate concentrations of 6 $\mu\text{mol l}^{-1}$ in the filament, 3 $\mu\text{mol l}^{-1}$ at the upwelling front and $\sim 1 \mu\text{mol l}^{-1}$ in the warm offshore waters. When nutrients in the mixed-layer are consumed, maximum primary production shifts deeper in the water column where nutrients are still available, resulting in the presence of a deep chlorophyll maximum (Richardson et al., 2002). Despite the low Chl α concentrations, vertically integrated PP is 25-40% higher in the filament compared with the other two stations. With the ratio of primary production per unit chlorophyll between the three stations being so distinctly different, some speculation regarding the underlying cause is warranted. Two possible explanations are that either (1) there is more old biomass and therefore Chl α present at the upwelling front than in the filament which does not contribute to primary production or (2) differences in the chlorophyll α to carbon ratios of phytoplankton exist between the three stations. Veldhuis and Kraay (2004) found chlorophyll to carbon ratios to be strongly depth-dependent, showing up

to 300% more biomass per unit chlorophyll at the surface than at 150 m depth. This could mean that biomass in the filament (Fig. 16) is much higher than Chl α would suggest and explain the lower Chl α : PP ratios at the surface compared with the subsurface (Fig. 16a,c). An exception is the upwelling front, where Chl α : PP ratios at the surface and at depth are similar. Furthermore, this finding suggests that biomass at the warm water station is relatively low, since most of the depth-integrated Chl α and PP is found below the mixed-layer. Possible reasons for the low Chl α concentrations in the filament despite high primary production have already been discussed. An interesting consequence of the low Chl α concentrations in the filament which has not been mentioned yet is that phytoplankton self-shading is likely reduced in the filament, leading to a relatively deep penetration of light and a potentially more efficient use of the incident photosynthetically active radiation (PAR).

There are two potential points of criticism of our method to determine primary production from incubations. Firstly, the same level of shading (20%, 10%, 1%) was used for each sampling level (10 m, deep chlorophyll max, 1% Chl α) independent of actual sampling depth and the profiles of photosynthetically active radiation (PAR) and chlorophyll. This likely overestimates PP at locations of high surface chlorophyll concentrations (e.g. the upwelling front), because the samples received more light during the incubations on deck than what would have been available *in-situ*. However, this effect would only further increase the higher PP that is seen in the filament compared to the other two stations and is therefore not likely to substantially change the main result, since low Chl α concentrations and thus favorable light conditions were present there. Secondly, since zooplankton is eliminated from the incubations grazing does not occur and the measured primary production rates could be overestimated in regions with high zooplankton abundances. As it was discussed above that the presence of zooplankton even far offshore is likely within the filament, a thorough investigation of zooplankton abundance and community structure is warranted.

Our findings highlight the uncertainty that is inherent in VGPM (vertically generalized production model) estimates of primary production based on satellite ocean-color data

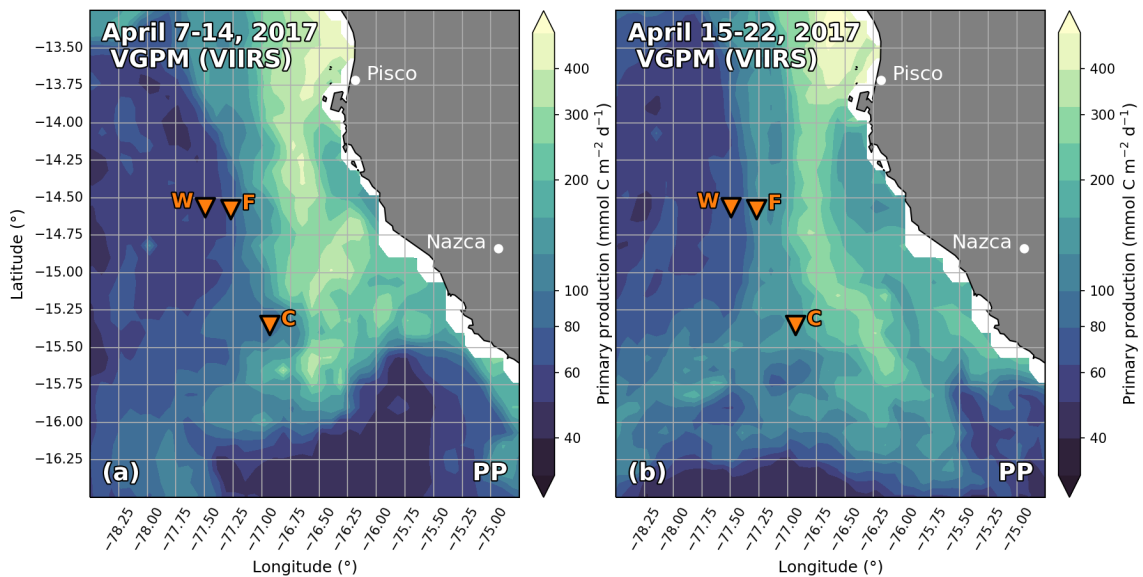


Figure 25: Estimates of vertically integrated primary production from satellite Chl α based on the VGPM model of [Behrenfeld and Falkowski \(1997\)](#) and Chl α data from the VIIRS satellite, weekly composites of (a) April 7-14, 2017 and (b) April 15-22, 2017. Orange triangles mark stations (W - warm, F - front, C - cold filament) where primary production was measured during the filament survey (Fig. 16). The respective times of sampling at these stations were: W - 2017/04/15, 2:16 UTC, F - 2017/04/17, 6:26 UTC and C - 2017/04/16, 15:20 UTC.

(Friedrichs *et al.*, 2009). It was recognized by Behrenfeld and Falkowski (1997) that knowing the small-scale, intermittent temporal and horizontal Chl α variability is crucial for estimating the vertically integrated primary production over the euphotic zone (PP_{eu}), more so than knowing the vertical profile. While our results show that indeed horizontal Chl α variability can be very high on scales of $\mathcal{O}(10)$ km and is therefore important for the estimation of PP_{eu} , we also find pronounced differences in the vertical profiles of PP that strongly influence the vertical integral. Our results show a high degree of intermittency associated with the coastal upwelling in conjunction with submesoscale physical processes and agree in the sense that the temporal variability is crucial for estimating PP_{eu} . Comparing our PP measurements with satellite estimates based on the VGPM model of Behrenfeld and Falkowski (1997) (Fig. 25) we find that PP at the upwelling front is similar to our measurements (~ 130 mmol C m $^{-2}$ d $^{-1}$) while PP in the warm offshore waters (70-80 mmol C m $^{-2}$ d $^{-1}$) and in the cold filament (100-150 mmol C m $^{-2}$ d $^{-1}$) is underestimated by 75-125%. However, PP rates of similar magnitude as in the cold filament in our measurements are present ~ 50 km further inshore in the satellite estimates. These differences highlight the difficulties in accounting for dynamic phytoplankton growth in satellite estimates that rely on Chl α and the limitations associated with the resulting products. It is also apparent that the satellite estimates do not accurately account for the PP associated with deep chlorophyll maxima offshore of the upwelling front, although at the respective station our measurements are also slightly uncertain due to likely phytoplankton self-shading in the narrow subsurface peak that would lead to an overestimation of PP (Fig. 16a). The uncertainties in estimating vertical profiles of Chl α from surface values were mentioned by Richardson *et al.* (2002) and a classification in profiles with deep and shallow Chl α maxima based on SST was proposed, a conclusion that our results support with the addition that the upwelling front does not clearly belong in either class but is a mixture of the two. However, the uncertainty associated with the unknown Chl α :C ratio when estimating PP from Chl α still remains. Using satellite estimates of PP to assess the effect of filaments on primary production is thus expected to be associated with large uncertainties.

7.1 Variability of chlorophyll and primary production in the Peru upwelling

Our measured rates of primary production in the filament do not distinguish between regenerated production from ammonium and new production from nitrate ([Dugdale and Goering, 1967](#)). However, the fact that nitrate concentrations in the filament ~ 150 km offshore are only 20 - 50% of those measured near the coast and NO_3^- appears to decrease with offshore distance on cross-shore transect T1BIO (Fig. 14) is an indicator that a substantial amount of *PP* is fueled by newly upwelled nitrate. We can test the plausibility of this hypothesis with a simplistic estimate of nitrate uptake: Salinities that match those in the filament core (35.2 g kg^{-1}) occur ~ 20 km from the coast on cross-shore transect T1BIO (Fig. 14), where NO_3^- concentrations of $\sim 12 \mu\text{mol l}^{-1}$ are found, yielding an approximate difference of $7 \mu\text{mol l}^{-1}$. We can then estimate the nitrate uptake dividing the observed primary production of $7.5 \mu\text{mol C l}^{-1} \text{ d}^{-1}$ inside the filament by a C:N ratio of 6.625 ([Redfield, 1963](#)) and obtain $1.13 \mu\text{mol N l}^{-1} \text{ d}^{-1}$. At this rate, reducing NO_3^- concentrations in the upwelling to those observed 150 km offshore in the filament would take ~ 6.2 days. Velocities of $\sim 25 \text{ km d}^{-1}$ observed in the filament indicate that 6 days is a reasonable timescale for offshore advection of a water parcel from the coast within the filament. Admittedly, large uncertainties are associated with this rather crude estimate since it is likely that (1) primary production in the upwelled water did not remain constant, (2) the ratio of C and N uptake does not correspond exactly to the Redfield ratio, (3) the water parcel did not travel offshore in a straight line and (4) was subject to mixing with the surrounding water. Nevertheless, it serves its purpose to illustrate that advected NO_3^- from the upwelling patch near the coast is in principle sufficient to support the observed phytoplankton growth inside the filament. It is therefore reasonable to assume that the primary production occurring within the filament is largely new production.

New production and export of organic matter are closely linked and thought to compensate each other in a steady state, although this balance holds only for a one-dimensional ocean and is not valid on small temporal and spatial scales ([Stukel et al., 2017a](#)). Submesoscale dynamics are expected to enhance the export of organic matter below the euphotic zone by means of subduction ([Lévy et al., 2012](#)). Recent studies indicate that export of organic matter by subduction at oceanic fronts is of similar magnitude as the

gravitational export by sinking particles and likely not detected by common measurement methods like sediment traps and ^{238}U - ^{234}Th disequilibrium (*Omand et al.*, 2015; *Stukel et al.*, 2017a,b). This points to a high potential impact of submesoscale processes on oxygen in the shallow OMZ off Peru, since remineralization of organic matter drives oxygen loss at the subsurface. The abundance of particles measured by an underwater vision profiler (UVP) and the relative abundance of small and large particles could be used as an indicator for export of organic matter. Work in progress suggests that high particle abundances extend further down below the filament than in the surrounding area, and that the relative abundance of small particles is higher (not shown), which could indicate a higher contribution of subduction relative to sinking. However, a detailed analysis of this dataset is beyond the scope of this thesis and will be carried out in future work. The UVP data will then also be used for information on zooplankton abundance, biomass and community structure in order to identify possible patterns associated with filaments and assess the influence of zooplankton grazing and excretion on surface chlorophyll and ammonium concentrations as well as primary production.

Summarizing, our results suggest that the low chlorophyll α concentrations despite substantial primary production in the core of the observed cold filament are either due to relatively slow phytoplankton growth in the upwelled water or zooplankton grazing pressure. We identified a highly variable relationship of surface chlorophyll α and depth-integrated primary production, which highlights the inherent uncertainty of primary production estimates based on ocean-color measured from satellites. The relative contributions of new- and regenerated production to the total primary production, as well as the export production associated with the cold filament are still unclear and will be assessed in future work.

7.2 Impact of the model formulation on the biogeochemistry of filaments

Filaments of similar lateral scale, horizontal and vertical structure and offshore extent as in the observations are present in the submesoscale-permitting model simulations. Bio-

geochemical variables and especially nutrients however exhibit substantial differences to observations in both magnitude and gradients. Most notably, the BioEBUS model fails to reproduce the offshore nitrate maxima that characterize the observed cold filament and exhibited an unrealistic cross-shore gradient of chlorophyll α . The PISCES model performs well overall in representing the along-shore variability in nitrate and Chl α associated with observed filaments, but the simulations exhibit large volumes of high-ammonium waters extending over the whole water column along the shelf which is not observed. These differences to observations in the variability of the biogeochemical fields at the scale of filaments can be related to large-scale biases in the biogeochemical models (Sec. 4.4) that project onto smaller scales. In the following, we will investigate the underlying reasons for these large-scale biases first in the BioEBUS and then in the PISCES simulation. We will conclude with an assessment of the overall performance of both models in representing the biogeochemistry of observed cold filaments off Peru.

The key role of relatively slow phytoplankton growth in maintaining high-nutrient, low-chlorophyll conditions in the PCUS and thereby facilitating an export of upwelled nutrients into the open ocean was discussed in section 7.1. We asserted that it is crucial for biogeochemical models to correctly represent this growth timescale in order to obtain realistic near-surface distributions of Chl α and nutrients. In the following we will present evidence that an overestimated maximum phytoplankton growth rate is responsible for the large-scale biases in nitrate, chlorophyll α and ammonium that are seen in the BioEBUS simulations.

Large differences between the PISCES45 and BioEBUS45 simulations are readily apparent in surface fields of primary production (PP), new production (NP) and the relative share of new production in the total primary production (Fig. 26). Primary production rates in PISCES45 are of $\mathcal{O}(10)$ $\mu\text{mol C l}^{-1} \text{d}^{-1}$ and thus similar to observations (Fig. 16) while these rates are an order of magnitude too high in BioEBUS45 (Fig. 26a,b). New production mainly occurs within 20 km from the coast in BioEBUS45, resembling the surface nitrate distribution (Fig. 26d; 22). An exception is a local maximum at 15.25°S / 76.25°W

that is associated with the filament. The narrow band of high NP near the coast can explain the fact that the near-surface is almost completely nitrate-depleted outside of this coastal band, since the nitrate supplied through upwelling is immediately used for phytoplankton growth. Offshore of the coastal NP maximum, the ratio of $NP : PP$ is low (10% - 20%) pointing to a fast recycling loop maintaining the high primary production at the surface essentially without supply of nutrients from the coastal upwelling (Fig. 26b,f). Moreover, this suggests that the associated rapid uptake of ammonium is responsible for the low overall ammonium concentrations that are seen in the BioEBUS simulations (Fig. 23e; 24e). In contrast, new production in PISCES45 is not restricted to the coast and can locally contribute >50% of the total primary production within filaments as far as 150 km offshore (Fig. 26e).

The apparent differences in primary production between the two models can be related to the chosen model parameters. BioEBUS has the maximum growth rate set to a value of 0.8356 d^{-1} for large phytoplankton and to 0.557 d^{-1} for small phytoplankton. While the growth rate for small phytoplankton is similar to the value of 0.6 d^{-1} in PISCES, large phytoplankton grows considerably faster in BioEBUS. The difference does not seem dramatic at first glance, but one has to keep in mind that the growth is exponential and a difference of only 0.24 d^{-1} leads to - excluding grazing and mortality - a relative doubling of the phytoplankton standing stock in BioEBUS compared to PISCES within 5 days. Other relevant parameters that could contribute to apparent differences are the half-saturation constants for nitrate, nitrite and ammonium ([Eppley et al., 1969](#)) which have not been compared yet. The maximum phytoplankton growth rate used in our BioEBUS simulations originates in [Koné et al. \(2005\)](#) who followed an approach of model validation and tuning of biogeochemical parameters on the basis of satellite chlorophyll data. One needs to proceed with caution along such a path, since model biases of Chl α in EBUS are often related to physical biases of upwelling strength and location along the coast (Fig. 27) due to errors in the wind forcing ([Capet et al., 2004](#)) and an attempt to correct for these dynamical deficiencies by tuning the biogeochemistry can entail undesired consequences throughout the biogeochemical cycles. Based on the results presented in this study, we

7.2 Impact of the model formulation on the biogeochemistry of filaments

would advocate for a different approach and propose to mainly use observed primary production rates as a guideline for all parameters related to phytoplankton growth.

Filaments in the PISCES simulation exhibit ammonium concentrations of the same magnitude as in the observations. However, the surface distribution resembles that of nitrate and decreases continuously offshore (Fig. 19) suggesting upwelling of ammonium and offshore transport within the filament. Vertical sections reveal the presence of a deep ammonium reservoir along the shelf (Fig. 20) extending from the surface down to 300 m depth (not shown). While deep ammonium plumes extending offshore from the shelf have been observed between 12°S - 14°S off Peru by *Kalvelage et al.* (2013) (their supplementray Figure 1f), these maxima cover a smaller depth range and do not extend to the surface. We can therefore conclude that the upwelling of ammonium in the PISCES simulation is unrealistic. This has implications for the rates of new- and regenerated production calculated by the model, which in this case would not be meaningful as the ammonium that is supplied from depth by coastal upwelling should rather be considered as a form of new production. This reveals that either too much remineralization of sinking organic matter occurs at depth, or that a process acting as an ammonium sink at depth is not represented in the PISCES model. Excess remineralization at depth could be caused by a rather crude parameterization of the interaction of detritus with the seafloor in PISCES. Since no sediment model is included, particles that sink to the bottom can not accumulate but are instantly dissolved and subject to remineralization (*Aumont et al.*, 2015a). This is in contrast to BioEBUS, where detritus can accumulate in the sediment without further interaction with the overlying water column (*Gutknecht et al.*, 2013). Moreover, the deep ammonium maximum approximately coincides with the vertical extent of the oxygen minimum zone, suggesting that its presence could be related to the different representation of redox-sensitive processes due to a simplified nitrogen cycle in PISCES. Anammox (anaerobic oxidation of nitrite and ammonium) is such a process that would act as a sink to ammonium at depth but is not included in PISCES. It seems likely that a combination of these two effects is responsible for the excess ammonium along the shelf in the PISCES simulations.

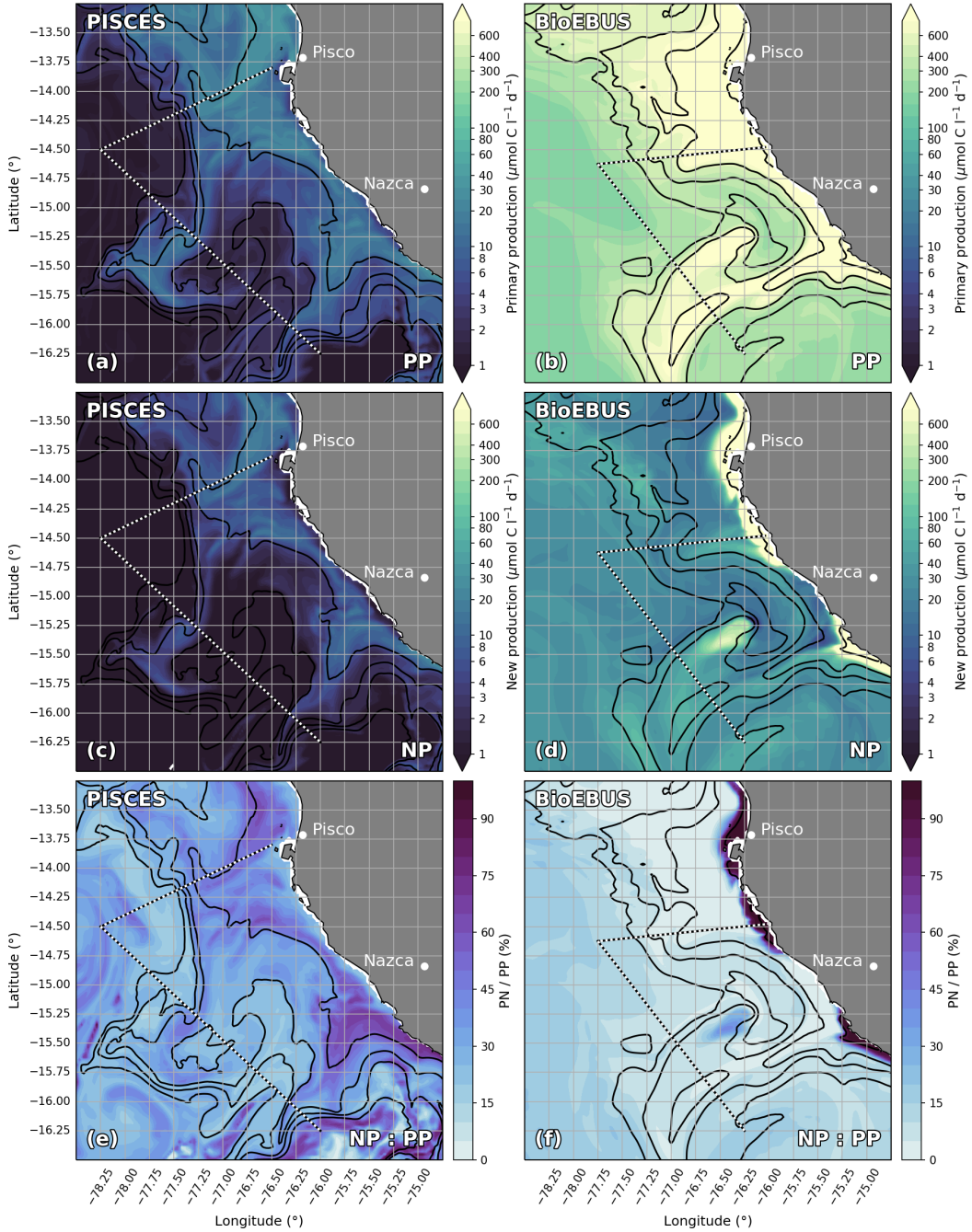


Figure 26: Surface fields of (a,b) Primary production (b,c) new production and (d,e) the relative fraction of new production (NP / PP) in the (a,c,e) PISCES and (b,d,f) BioEBUS simulations at the same time as in [Figure 19](#) and [Figure 22](#), respectively. Primary production in the BioEBUS model was converted to $\mu\text{mol C l}^{-1} \text{d}^{-1}$ by multiplication of the native $\mu\text{mol N l}^{-1} \text{d}^{-1}$ units with 6.625 ([Redfield, 1963](#)) which corresponds to the C:N ratio BioEBUS. New production represents uptake of NO_3^- in PISCES and combined uptake of NO_3^- and NO_2^- in BioEBUS.

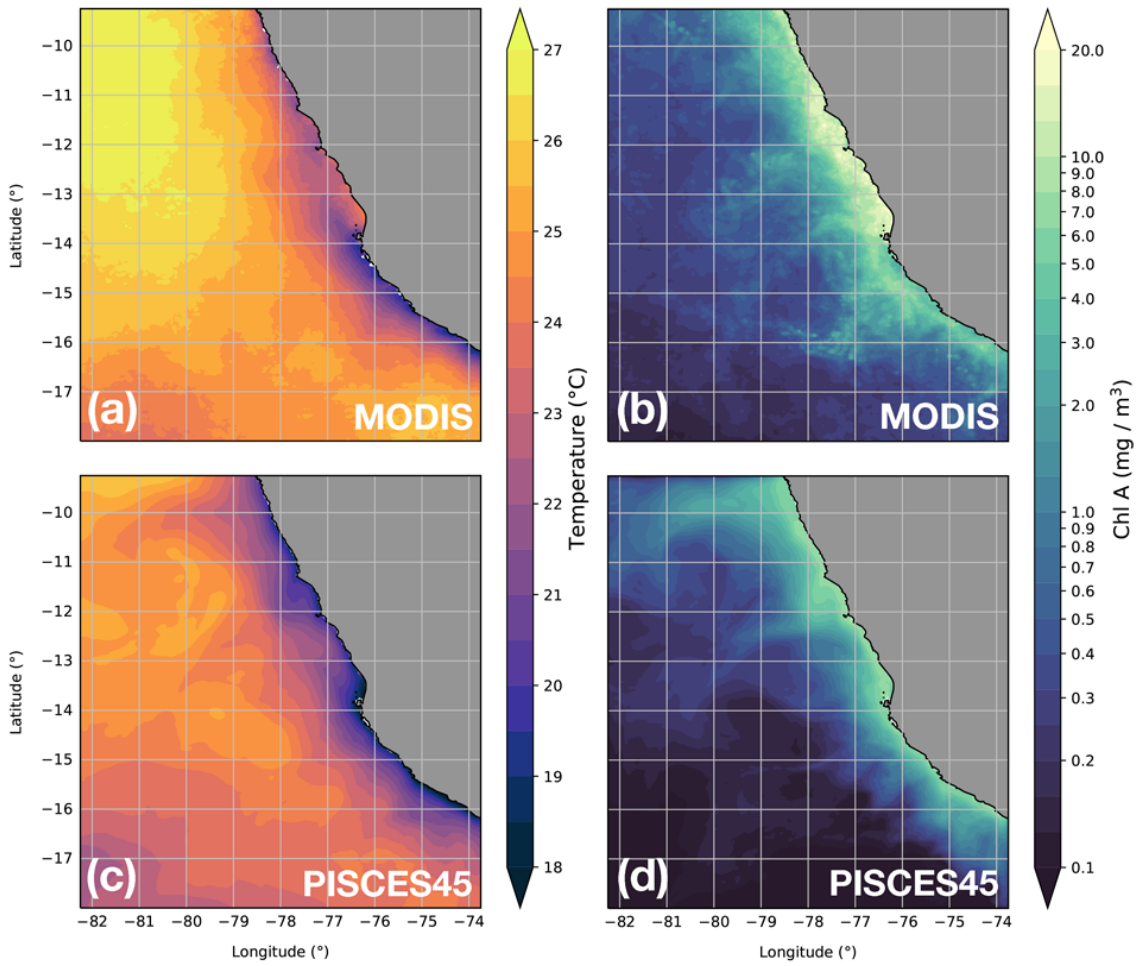


Figure 27: Surface fields of (a,c) temperature and (b,d) chlorophyll α from (a,b) MODIS satellite observations and (c,d) the PISCES45 model simulation averaged over January–March 2017.

Summarizing, the PISCES model is able to represent the enhanced nitrate concentrations associated with observed filaments while the BioEBUS model does not exhibit this characteristic pattern, which is likely related to the phytoplankton growth rate. In BioEBUS, uptake rates of nitrate and ammonium are an order of magnitude too high, resulting in surface nitrate depletion over most of the model domain, an unrealistic cross-shore chlorophyll α gradient and ammonium concentrations an order of magnitude too low. Due to the pronounced biases in the biogeochemical fields and the resulting misrepresentation of

7 Discussion

filaments compared with observations, the BioEBUS model in its present configuration cannot be used with confidence to assess net effect of filaments on the biogeochemistry off Peru. In PISCES, surface ammonium concentrations are comparable to observations, but the horizontal distribution resembles that of nitrate suggesting upwelling of ammonium from a deep reservoir along the shelf, which appears unrealistic. However, this bias does not seem to negatively impact the distribution of nitrate, primary production or chlorophyll, justifying the use of these simulations to asses the impact of submesoscale effects on the biogeochemistry of the PCUS.

7.3 Effect of submesoscale processes on the biogeochemistry of the Peru upwelling system

Eddies have been shown to reduce primary production in the highly productive eastern boundary upwelling systems by exporting upwelled nutrients offshore and downward below the euphotic zone (*Rossi et al.*, 2008, 2009; *Lévy*, 2003; *Lathuilière et al.*, 2010; *Gruber et al.*, 2011; *Nagai*, 2015). It was acknowledged by *Nagai* (2015), who described the subduction and lateral export associated with filaments in their model, that due to the relatively coarse horizontal resolution (5 km) their calculations of the associated offshore and downward eddy-fluxes do not take into account the pronounced nutrient injections near filaments and fronts that occur in the submesoscale range (*Lapeyre and Klein*, 2006; *Lévy*, 2003; *Lévy et al.*, 2012; *Mahadevan*, 2015). *Lévy* (2003) investigated the effect of filaments and fronts in an idealized submesoscale-permitting (2 km) model and found that the effect of submesoscale frontal processes on primary production strongly depends on the amount of available nutrients within the euphotic zone. If the surface is largely depleted of nutrients, vertical nutrient injection and rapid uptake of the supplied nutrients by primary production are the dominant effects. In the presence of a large scale horizontal nutrient gradient in the euphotic zone which is characteristic for coastal upwelling regions, the effect of fronts and filaments changes with time: As long as nutrients are abundant, phytoplankton blooms and nutrients are subducted, the downward export of nutrients acting to reduce the primary production. However, once the bloom declines and nutrients are depleted, vertical nutrient injection is again dominant.

Our submesoscale-permitting simulations have a horizontal resolution that is effectively by more than a factor of 2 higher than in the studies by *Gruber et al.* (2011) and *Nagai* (2015) because the first baroclinic Rossby radius of deformation - the length scale below which ageostrophic effects become important - decreases with latitude and their domain is located off California (28°N - 48°N). We therefore assume submesoscale frontal processes and the associated vertical velocities (*Thomas et al.*, 2008; *McWilliams et al.*, 2009; *McWilliams et al.*, 2015) to better resolved in our simulations compared with the studies by *Gruber et al.* (2011) and *Nagai* (2015). The impact of increased horizontal

resolution on the long-term averaged biogeochemical fields was investigated in section 4.3 based on the difference between the coarse- ($1/9^\circ$) and high-resolution ($1/45^\circ$) simulations. In a first-order assessment, this difference can be taken to represent the influence of submesoscale frontal processes and the associated horizontal and vertical eddy-fluxes that are additionally resolved in the high-resolution simulations, an assumption that is justified by the pronounced increase in eddy kinetic energy by a factor of 2 from coarse to high resolution (Fig. 7). To recapitulate, the effect of submesoscale-permitting resolution in the PISCES simulations is greatest near the coast at ~ 25 m depth and in a tongue that extends from this maximum ~ 250 km offshore along the nutricline, where a decrease in nitrate ($-2.5 \mu\text{mol l}^{-1}$) and an increase in oxygen ($+20 \mu\text{mol l}^{-1}$) are apparent (Fig. 8a,b,e,f). A decrease in chlorophyll α ($0.3 - 1 \text{ mg m}^{-3}$) with the same offshore extent is seen at the surface. Further offshore at 100 m depth, an increase in nitrate ($+2 \mu\text{mol l}^{-1}$) and a decrease in oxygen ($-15 \mu\text{mol}$) is found. The horizontal patterns of the changes in oxygen and nitrate reveal that they are largest in regions of increased eddy kinetic energy (Fig. 7; 9). Furthermore, the vertical and horizontal patterns of the opposing changes in oxygen and nitrate concentrations exhibit a high spatial correlation.

A similar approach was chosen by Gruber *et al.* (2011), who compared an eddy-permitting (5 km) simulation with a "non-eddy" simulation of similar resolution but with non-linear terms in the model equations set to zero. Comparing change in nitrate between these two simulations with the change in nitrate between the PISCES45 and PISCES9 simulations, the main patterns of decreased nitrate concentrations within ~ 300 km from the coast and increased nitrate concentrations further offshore is in good agreement (Fig. 28a,b). The patterns of the changes in density also agree and can be explained by lateral eddy-fluxes that induce a shoreward heat transport which flattens the isopycnals (Gruber *et al.*, 2011) (Fig. 29b). The increase in density that occurs in our simulations between 200–300 m depth near the shelf is likely related to the stronger undercurrent in the PISCES45 simulation (Fig. 6a,b) which is excluded by the analysis of Gruber *et al.* (2011). The vertical and horizontal eddy-fluxes responsible for eddy-induced changes in the simulations of Gruber *et al.* (2011) are shown in Figure 29. The maximum downward and offshore

7.3 Effect of submesoscale processes on the biogeochemistry of the Peru upwelling system

eddy-fluxes occur 100 km and 250 km offshore at 25 m and 100 m depth, respectively.

As the lateral export of nitrate from the near-shore region to the open ocean appears to be similar in our simulations to the results of [Gruber et al. \(2011\)](#), a reduction in primary production is expected. Although primary production was unfortunately not saved during the period analyzed here, a decrease of surface Chl α concentrations that dominates the increase at the subsurface suggest that primary production was reduced in the PISCES45 simulation.

The timescale of phytoplankton growth was found to be realistic in the PISCES simulations, while primary production in BioEBUS is likely overestimated by an order of magnitude (Sec. 7.2). Accordingly, the impact of submesoscale-permitting resolution on surface Chl α concentrations appears to be much more pronounced in PISCES than in BioEBUS, indicating that the nutrient uptake is fast enough in BioEBUS to occur before subduction (Fig. 8c,d). This would mean that Chl α instead of nitrate is subducted, which is consistent with higher Chl α concentrations seen at the subsurface in BioEBUS. The increase in oxygen that is seen within 250 km from the coast in PISCES45 shows high spatial correlation with the decrease in nitrate, suggesting that lateral eddy-fluxes are responsible for this change as well (Fig. 9a,b,e,f). Furthermore, our results agree with the prediction by [Lévy \(2003\)](#) that submesoscale frontal processes export nutrients downward and offshore in regions with relatively high surface nutrient concentration such as EBUS and thus act to reduce primary production.

Our main caveat is the relatively coarse vertical resolution of 32 levels in all our simulations, similar to the configurations used by [Gruber et al. \(2011\)](#) and [Nagai \(2015\)](#). This low vertical resolution appears to limit the ability of the model to represent sharp vertical density gradients. We have shown in section 6.3 that the N^2 maximum at base of the mixed-layer is about 50% lower in the simulations compared with observations. This is reflected in almost horizontal isopycnals at this depth in the observations (Fig. 17), while isopycnals in the simulations have a steeper slope and extend to greater depths, providing a more direct path to the subsurface and thus favorable conditions for subduction (Fig. 21). The representation of filaments and the subduction that occurs along these isopycnals

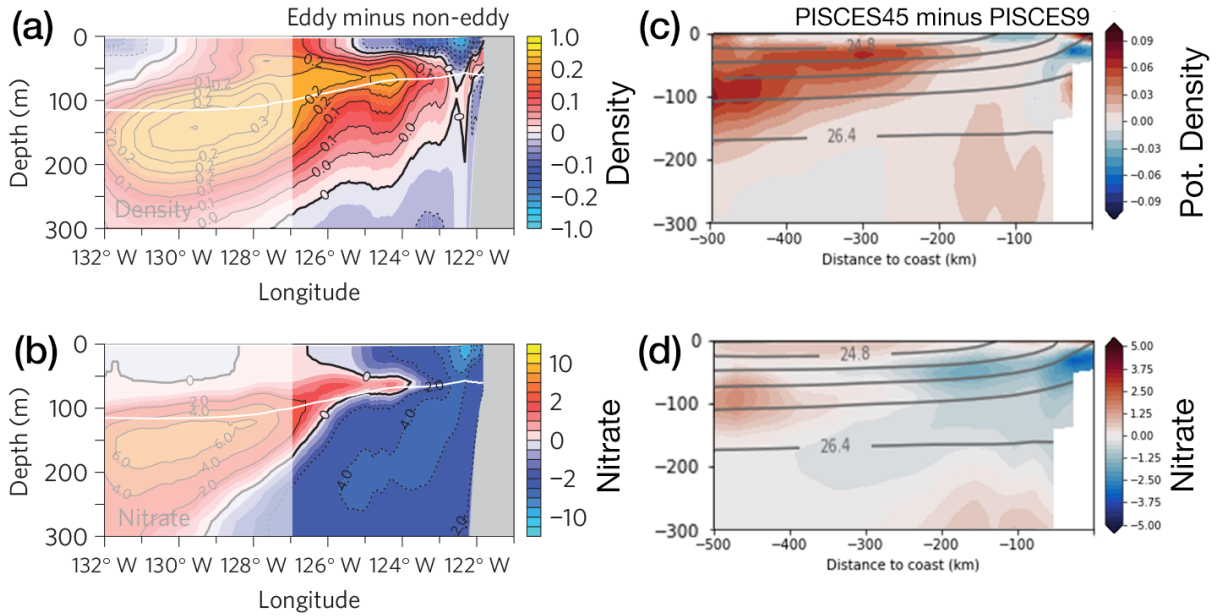


Figure 28: (a) Density and (b) nitrate differences between the eddy and non-eddy simulations of [Gruber et al. (2011)]. (c) Potential density and (d) nitrate differences between the PISCES45 and PISCES9 simulations in this study, similar as in Figure 8 but scaled to the same depth as panels (a,b). The area in panels (a,b) which has a greater offshore extent than panels (c,d) is shaded transparent white. Panels (a,b) taken from [Gruber et al. (2011)].

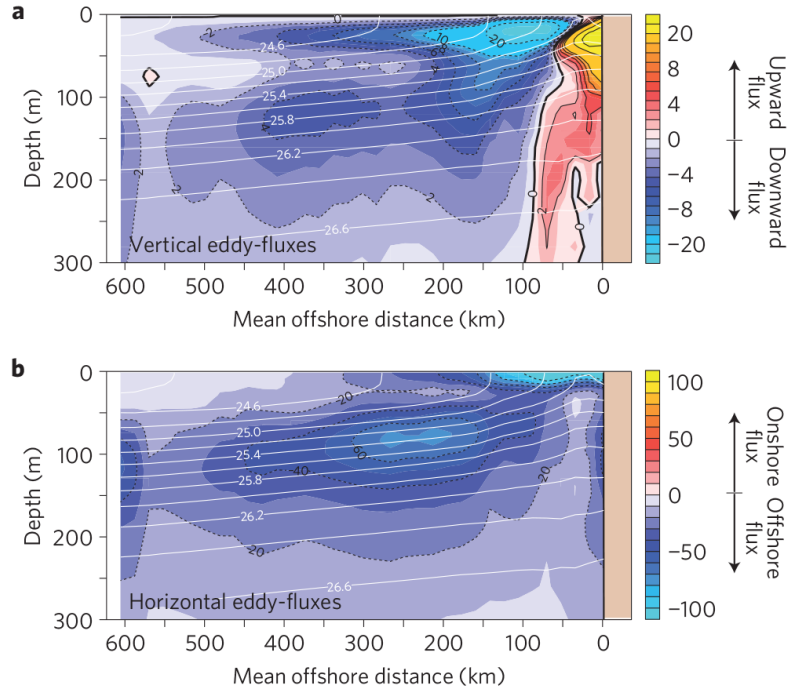


Figure 29: (a) Vertical and (b) horizontal eddy-fluxes of total nitrogen in a model of the California upwelling system. Figure taken from [Gruber et al. \(2011\)](#)

could therefore be strongly affected by this bias. We expect a higher near-surface stratification and a more effective decoupling of the mixed-layer decrease subduction and an increase the offshore transport of biogeochemical tracers near the surface. This prediction is supported by the strong separation of physical and biogeochemical parameters across the N^2 maximum that is seen beneath the observed cold filament (Fig. 15; 17). Less subduction and a longer residence time of upwelled nutrients in the mixed layer would result in more primary production, possibly alleviating the reducing effect that has been found in previous studies.

Summarizing, our results suggest that the effect of submesoscale frontal processes on the biogeochemistry of the PCUS is increased subduction and offshore transport of nitrate that leads to reduced primary production. Changes in oxygen resemble the pattern of changes in nitrate, suggesting a ventilation of the shallow OMZ off Peru by horizontal and vertical eddy-fluxes. However, we expect these results to be dependent on the vertical

model resolution and its ability to resolve sharp density near-surface gradients. Further analysis needs to be carried out in order to disentangle the physical and biogeochemical drivers of these changes and investigate their interaction.

8 Summary and Outlook

This thesis focused on physical-biogeochemical coupling at cold filaments and the effect of submesoscale processes on the biogeochemistry of the Peru upwelling system. The aim was to answer the two main questions:

1. How does the observed biogeochemistry of cold filaments off Peru compare with their representation in submesoscale permitting coupled physical-biogeochemical model simulations?
2. What is the role of filaments for primary- and export production and the export of nutrients, chlorophyll and oxygen into the shallow coastal OMZ off Peru?

We first identified the characteristic biogeochemical variability associated with an observed cold filament (Sec. 5). The observed filament contains relatively cold, fresh and nutrient-rich waters originating in the coastal upwelling, which results in a distinct along-shore variability of the physical and biogeochemical fields. Enhanced nitrate concentrations and offshore velocities of up to 0.5 m s^{-1} within the filament suggest the offshore transport of nutrients. Even though nutrients are abundant, chlorophyll concentrations are very low inside the filament and highest at the boundary separating it from the nutrient-depleted, warm offshore waters. High ammonium concentrations coinciding with low chlorophyll α concentrations are observed in the core of the filament, suggesting that remineralization of organic matter dominates primary production in the recently upwelled water. Despite the low Chl α concentrations, substantial primary production is observed inside the filament, pointing to a high uncertainty associated with the use of chlorophyll α as a proxy for primary production.

Next, we assessed the representation of filaments in submesoscale-permitting biogeochemical model simulations (Sec. 6). The simulations exhibit filaments that are similar in lateral scale, horizontal and vertical structure and offshore extent to those observed. Biogeochemical variables and especially nutrients however show substantial differences in both magnitude and gradients. Enhanced surface nitrate concentrations associated with filaments are seen in PISCES45 but not in BioEBUS45, where the surface is depleted of

nitrate further than 20 km from the coast. While both models show enhanced ammonium concentrations at filament locations, these are unrealistically deep and too high in PISCES45 and an order of magnitude too low in BioEBUS45. Disregarding the error in absolute values, both vertical and cross-shore gradients of ammonium appear more realistic in BioEBUS than in PISCES. The observed cross-shore gradient of surface Chl α is well reproduced in PISCES45, but small scale features like frontal maxima are missing and near-shore minima in the upwelling patches are too confined to the coast. The importance of sufficiently slow phytoplankton growth for maintaining realistic concentrations of upwelled nutrients offshore is stressed.

We then discussed possible explanations for the biogeochemical variability associated with the observed cold filament (Sec. 7.1). Our results suggest that the low chlorophyll α concentrations despite substantial primary production in the core of the observed filament are either due to relatively slow phytoplankton growth in the upwelled water or zooplankton grazing pressure. We identified a highly variable relationship of surface chlorophyll α and depth-integrated primary production, which highlights the inherent uncertainty of primary production estimates based on ocean-color measured by satellites. The relative contributions of new- and regenerated production to the total primary production, as well as the export production associated with the cold filament are still unclear and will be assessed in future work.

Next, the impact of the model formulation on the representation of the biogeochemical variability associated with cold filaments was discussed (Sec. 7.2). The PISCES model is able to represent the enhanced nitrate concentrations associated with observed filaments while the BioEBUS model does not exhibit this characteristic pattern, which is likely related to the phytoplankton growth rate. In BioEBUS, uptake rates of nitrate and ammonium are an order of magnitude too high, resulting in surface nitrate depletion over most of the model domain, ammonium concentrations an order of magnitude too low and an unrealistic cross-shore chlorophyll α gradient. In PISCES, surface ammonium concentrations are comparable to observations, but the horizontal distribution resembles that of nitrate suggesting upwelling of ammonium from a deep reservoir along the shelf,

which appears unrealistic. However, this bias does not severely limit the ability of the PISCES model to be used for investigating the impact of submesoscale processes on the biogeochemistry of the PCUS.

As a final result of this thesis, we assessed the overall effect of submesoscale processes on the biogeochemistry of the Peru upwelling system (Sec. 7.3). The simulations suggest that the effect of submesoscale frontal processes on the biogeochemistry of the PCUS is increased subduction and offshore transport of nitrate that leads to reduced primary production. Changes in oxygen resemble the pattern of changes in nitrate, suggesting a ventilation of the shallow oxygen minimum zone off Peru by horizontal and vertical eddy-fluxes.

Further analysis is needed in order to disentangle the physical and biogeochemical drivers of these changes and investigate their interaction. Several opportunities have presented themselves for substantiating our results with further analysis of observations and model simulations which were beyond the scope of this thesis. An outlook on this analysis and possible future studies that would increase the understanding of submesoscale processes in upwelling systems will be given in the following.

The observed cold filament was identified as a hotspot of primary production and presumably new production (Sec. 5), but the extent to which the filament contributes to the export of organic matter by subduction has not been quantified. However, this parameter is of particular interest for the shallow OMZ off Peru since it determines remineralization and therefore oxygen consumption at depth. We will try to obtain an estimate of the export of organic matter within the filament from particle abundances measured by an underwater vision profiler (UVP). Furthermore, we will determine if the relative abundances of small and large particles can be used as an indicator for the relative contributions of subduction and sinking. If this is the case, a more extensive UVP dataset could be used for upscaling our export estimates to a larger region. The UVP data will also be used for information on zooplankton abundance, biomass and community structure in order to identify possible patterns associated with filaments and assess the influence of zooplankton

grazing and excretion on surface chlorophyll and ammonium concentrations. Moreover, underway pCO₂ measurements were acquired during the filament survey and an analysis of this data could provide valuable insights into the impact of filaments on the air-sea gas exchange of CO₂. The effect of submesoscale processes on the biogeochemistry of the PCUS was investigated in this study by simply subtracting the mean fields from the 1/45° and 1/9° model simulations. While this is a valid approach for a first-order assessment, the mean circulation also contributes to the changes that are seen in the biogeochemical fields. To remove this influence and substantiate our results, we will calculate the vertical and horizontal eddy-fluxes similar to [Gruber et al. \(2011\)](#) and [Nagai \(2015\)](#).

While the submesoscale-permitting biogeochemical model simulations generally succeeded in representing the physical-biogeochemical variability associated with cold filaments, a number of ways to improve the model configuration were identified that will now be discussed briefly.

Our simulations suggest that the effectiveness of subduction is sensitive to the vertical model resolution and its ability to represent sharp density gradients at the base of the mixed-layer in (Sec. 7.3). This hypothesis should be tested by drastically increasing the number of vertical levels especially in the upper 50 - 100 m. [Stewart et al. \(2017\)](#) recently demonstrated that increasing the vertical resolution in a global 1/10° z-coordinate model yields among other things an increase in EKE by up to 200%. These results are promising in the sense that the computational cost for increasing the vertical resolution scales linearly and is therefore much lower compared to an increase in horizontal resolution. To our knowledge, no similar studies with sigma-coordinate models are published. Moreover, the model domain of the inner 1/45° nest was found to be relatively small especially in along-shore direction compared to the temporal and spatial scales of some relevant processes. At a speed of 15 cm s⁻¹ the undercurrent passes through the whole model domain within 2 - 3 months and flushes the area near the shelf with the biogeochemical properties present at the open boundary to the coarse-resolution model. This effect could severely limit the ability of the high-resolution simulations to deviate substantially from the coarse-resolution simulations. Increasing the along-shore extent of high-resolution

domain should improve this shortcoming. In addition, it would be useful to align the grid in along-shore direction so that the cross-shore extent is constant throughout the domain. Another difficulty was the dominant impact of mesoscale variability, which differed between the PISCES and BioEBUS simulations and complicated the comparison of the biogeochemical models. To simplify such model comparisons in the future, the two biogeochemical models should be coupled to the same physical simulation, with the side effect of reducing the computational cost. Furthermore, to address the biases that were identified in the biogeochemical models (Sec. 7.2) we propose to (1) decrease the maximum phytoplankton growth rate in BioEBUS to obtain realistic nutrient concentrations offshore and (2) implement a sediment model in PISCES to reduce remineralization of organic matter and therefore ammonium concentrations near the bottom.

The main shortcoming of many high-resolution regional ocean models remains the wind forcing, since satellite wind measurements are not available near the coast and the interpolated coarse-resolution fields cannot reproduce the coastal wind drop-off that is seen in *in-situ* measurements ([Penven et al., 2001](#); [Capet et al., 2004](#); [Veitch et al., 2009](#)). This overestimation of the near-shore winds has a strong influence on the upwelling circulation, SST and biogeochemical processes ([Capet et al., 2004](#)). Comparing satellite SST with our model simulations, a cold bias near the coast at 13.5°S is readily apparent (Fig. 27a,c) that is likely related to an unrealistic upwelling location. The wind forcing therefore has immense potential for improving the representation of coastal upwelling systems in regional ocean models. Furthermore, mesoscale coupling of wind and sea-surface temperature (SST) is known to impact surface wind-stress and consequently the wind-driven ocean currents in the PCUS ([Oerder et al., 2016](#)). Sea-surface temperature in the study area near 15 °S exhibits a clear correlation with the wind speed and cloud cover (Fig. 11), indicative of a strong coupling between the oceanic and atmospheric boundary layers even below the mesoscale. Moreover, coupling between wind and SST has been shown to dampen near-surface eddy kinetic energy and reduce primary production ([Eden and Dietze, 2009](#); [Renault et al., 2016](#)). [Colas et al. \(2012\)](#) demonstrated the importance of the air-sea coupling for sensible and latent heat fluxes in the PCUS and predicted a large

8 Summary and Outlook

upscaling potential of these effects from regional to global scales and a possible impact on the persistent warm bias found in climate models. The effect of air-sea interaction on surface fluxes of momentum and heat should therefore be taken into account in future studies of submesoscale processes. The most obvious way to improve the wind forcing and at the same time include air-sea interaction would be the use of regional coupled ocean-atmosphere models. In the light of the substantial improvements of circulation, surface fluxes and biogeochemistry that are expected, the additional computational cost may be well justified.

Ultimately, the aim of integrated observational and modeling efforts such as this one is to help foster a greater understanding of the multi-scale physical-biogeochemical coupling so that parameterizations of the biogeochemical and physical fluxes associated with these processes can be used to improve more coarsely resolved climate and Earth system models, which exhibit persistent biases in eastern boundary upwelling systems. Furthermore, regional coupled biogeochemical models need to be improved for reliably downscaling global climate projections and assess the impact on rich marine ecosystems that require protection in order to provide resources and biodiversity for generations to come. These ecosystems will increasingly feel the effects of climate change in the coming decades, presenting a challenge for both regional and global biogeochemical models and the scientific community to deliver well-founded advice to society.

References

- Alcaraz, M., E. Saiz, and M. Estrada, Excretion of ammonia by zooplankton and its potential contribution to nitrogen requirements for primary production in the Catalan Sea (NW Mediterranean), *Marine Biology*, 119(1), 69–76, doi:10.1007/BF00350108, 1994.
- Arévalo-Martínez, D. L., A. Kock, C. R. Löscher, R. A. Schmitz, and H. W. Bange, Massive nitrous oxide emissions from the tropical South Pacific Ocean, *Nature Geoscience*, 8(7), 530–533, doi:10.1038/ngeo2469, 2015.
- Armstrong, F. A. J., C. R. Stearns, and J. D. H. Strickland, The measurement of upwelling and subsequent biological process by means of the Technicon Autoanalyzer® and associated equipment, *Deep Sea Research and Oceanographic Abstracts*, 14(3), 381–389, doi:[https://doi.org/10.1016/0011-7471\(67\)90082-4](https://doi.org/10.1016/0011-7471(67)90082-4), 1967.
- Astudillo, O., B. Dewitte, M. Mallet, F. Frappart, J. A. Rutllant, M. Ramos, L. Bravo, K. Goubanova, and S. Illig, Surface winds off Peru-Chile: Observing closer to the coast from radar altimetry, *Remote Sensing of Environment*, 191, 179–196, doi:10.1016/j.rse.2017.01.010, 2017.
- Aumont, O., C. Ethé, A. Tagliabue, L. Bopp, and M. Gehlen, PISCES-v2: An ocean biogeochemical model for carbon and ecosystem studies, *Geoscientific Model Development*, 8(8), 2465–2513, doi:10.5194/gmd-8-2465-2015, 2015a.
- Aumont, O., C. Ethé, A. Tagliabue, L. Bopp, and M. Gehlen, PISCES-v2: An ocean biogeochemical model for carbon and ecosystem studies, *Geoscientific Model Development*, 8(8), 2465–2513, doi:10.5194/gmd-8-2465-2015, 2015b.
- Ayón, P., M. I. Criales-Hernandez, R. Schwamborn, and H.-J. Hirche, Zooplankton research off Peru: A review, *Progress in Oceanography*, 79(2), 238–255, doi:<https://doi.org/10.1016/j.pocean.2008.10.020>, 2008.
- Bakun, A., and C. S. Nelson, The seasonal cycle of wind-stress curl in subtropical eastern boundary current regions, doi:10.1175/1520-0485(1991)021<1815:TSCOWS>2.0.CO;2, 1991.
- Behrenfeld, M. J., and P. G. Falkowski, Photosynthetic rates derived from satellite-based chlorophyll concentration, *Limnology and Oceanography*, 42(1), 1–20, 1997.
- Boyd, C. M., and S. L. Smith, Plankton, upwelling, and coastally trapped waves off Peru, *Deep Sea Research Part A. Oceanographic Research Papers*, 30(7), 723–742, doi:[https://doi.org/10.1016/0198-0149\(83\)90019-5](https://doi.org/10.1016/0198-0149(83)90019-5), 1983.
- Brannigan, L., Intense submesoscale upwelling in anticyclonic eddies, *Geophysical Research Letters*, 43(7), 3360–3369, doi:10.1002/2016GL067926, 2016.
- Brink, K., The near-surface dynamics of coastal upwelling, *Progress in Oceanography*, 12(3), 223–257, doi:10.1016/0079-6611(83)90009-5, 1983.

References

- Brink, K. H., B. H. Jones, J. C. Van Leer, C. N. K. Mooers, D. W. Stuart, M. R. Stevenson, R. C. Dugdale, and G. W. Heburn, Physical and Biological Structure and Variability in an Upwelling Center off Peru Near 15°S During March, 1977, in *Coastal Upwelling*, pp. 473–495, American Geophysical Union, doi:10.1029/CO001p0473, 1981.
- Bruland, K. W., E. L. Rue, G. J. Smith, and G. R. DiTullio, Iron, macronutrients and diatom blooms in the Peru upwelling regime: Brown and blue waters of Peru, *Marine Chemistry*, 93(2-4), 81–103, doi:10.1016/j.marchem.2004.06.011, 2005.
- Burt, W. V., D. B. Enfield, R. L. Smith, and H. Crew, The surface wind over an upwelling area near Pisco, Peru, *Boundary-Layer Meteorology*, 3(3), 385–391, doi:10.1007/BF00736188, 1973.
- Capet, X. J., P. Marchesiello, and J. C. McWilliams, Upwelling response to coastal wind profiles, *Geophysical Research Letters*, 31(13), doi:10.1029/2004GL020123, 2004.
- Chaigneau, A., N. Dominguez, L. Vasquez, R. Flores, C. Grados, and V. Echevin, Near-coastal circulation in the Northern Humboldt Current System from shipboard ADCP data, *Journal of Geophysical Research*, 118, 5251–5266, doi:10.1002/jgrc.20328, 2013.
- Chavez, F. P., R. T. Barber, P. M. Kosro, A. Huyer, S. R. Ramp, T. P. Stanton, and B. R. De, Horizontal Transport and the Distribution of Nutrients in the Coastal Transition Zone off Northern California: Effects on Primary Production, Phytoplankton Biomass and Species Composition, *Journal of Geophysical Research*, 96848(15), 833–14, doi:10.1029/91JC01163, 1991.
- Chavez, F. P., T. Takahashi, W. J. Cai, G. Friederich, B. Hales, R. Wanninkhof, and R. A. Feely, Coastal oceans, *The First State of the Carbon Cycle Report (SOCCR): The North American Carbon Budget and Implications for the Global Carbon Cycle*, pp. 157–166, 2007.
- Chavez, F. P., A. Bertrand, R. Guevara-Carrasco, P. Soler, and J. Csirke, The northern Humboldt Current System: Brief history, present status and a view towards the future, *Progress in Oceanography*, 79(2-4), 95–105, doi:10.1016/j.pocean.2008.10.012, 2008.
- Colas, F., J. C. McWilliams, X. Capet, and J. Kurian, Heat balance and eddies in the Peru-Chile current system, *Climate Dynamics*, 39(1-2), 509–529, doi:10.1007/s00382-011-1170-6, 2012.
- Dagg, M., T. Cowles, T. Whitledge, S. Smith, S. Howe, and D. Judkins, Grazing and excretion by zooplankton in the Peru upwelling system during April 1977, *Deep Sea Research Part A: Oceanographic Research Papers*, 27(1), 43–59, doi:[https://doi.org/10.1016/0198-0149\(80\)90071-0](https://doi.org/10.1016/0198-0149(80)90071-0), 1980.
- D'Asaro, E., C. Lee, L. Rainville, R. Harcourt, and L. Thomas, Enhanced Turbulence and Energy Dissipation at Ocean Fronts, *Science*, 332(6027), 318–322, doi:10.1126/science.1201515, 2011.
- Dengler, A. T., Relationship between physical and biological processes at an upwelling front off Peru, 15°S, *Deep Sea Research Part A, Oceanographic Research Papers*, 32(11), 1301–1315, doi:10.1016/0198-0149(85)90050-0, 1985.

- Dewitte, B., S. Illig, L. Renault, K. Goubanova, K. Takahashi, D. Gushchina, K. Mosquera, and S. Purca, Modes of covariability between sea surface temperature and wind stress intraseasonal anomalies along the coast of Peru from satellite observations (2000-2008), *Journal of Geophysical Research: Oceans*, 116(4), 1–16, doi:10.1029/2010JC006495, 2011.
- Dugdale, R. C., and J. J. Goering, Uptake of New and Regenerated Forms of Nitrogen in Primary Productivity, *Limnology and Oceanography*, 12(2), 196–206, doi:10.4319/lo.1967.12.2.0196, 1967.
- Echevin, V., O. Aumont, J. Ledesma, and G. Flores, The seasonal cycle of surface chlorophyll in the Peruvian upwelling system: A modelling study, *Progress in Oceanography*, 79(2-4), 167–176, doi:10.1016/j.pocean.2008.10.026, 2008.
- Eden, C., and H. Dietze, Effects of mesoscale eddy/wind interactions on biological new production and eddy kinetic energy, *Journal of Geophysical Research: Oceans*, 114(5), 1–13, doi:10.1029/2008JC005129, 2009.
- Eppley, R. W., J. N. Rogers, and J. J. McCarthy, Half-saturation Constants for Uptake of Nitrate and Ammonium by Marine Phytoplankton, *Limnology and Oceanography*, 14(6), 912–920, doi:10.4319/lo.1969.14.6.0912, 1969.
- Falkowski, P. G., D. Ziemann, Z. Kolber, and P. K. Bienfang, Role of eddy pumping in enhancing primary production in the ocean, *Nature*, 352(6330), 55–58, 1991.
- Ferrari, R., A Frontal Challenge for Climate Models, *Science*, 332(6027), 316–317, doi:10.1126/science.1203632, 2011.
- Fiedler, P. C., and L. D. Talley, Hydrography of the eastern tropical Pacific: A review, *Progress in Oceanography*, 69(2-4), 143–180, doi:10.1016/j.pocean.2006.03.008, 2006.
- Flament, P., and L. Washburn, The evolving structure of an Upwelling Filament, *Journal of Geophysical Research*, 15(90), 11,765–11,778, 1985.
- Fonseca, T. R., An Overview of the Poleward Undercurrent and Upwelling along the Chilean Coast BT - Poleward Flows Along Eastern Ocean Boundaries, pp. 203–228, Springer New York, New York, NY, doi:10.1007/978-1-4613-8963-7_15, 1989.
- Friederich, G. E., J. Ledesma, O. Ulloa, and F. P. Chavez, Air-sea carbon dioxide fluxes in the coastal southeastern tropical Pacific, *Progress in Oceanography*, 79(2-4), 156–166, doi:10.1016/j.pocean.2008.10.001, 2008.
- Friedrichs, M. A. M., et al., Assessing the uncertainties of model estimates of primary productivity in the tropical Pacific Ocean, *Journal of Marine Systems*, 76(1), 113–133, doi:https://doi.org/10.1016/j.jmarsys.2008.05.010, 2009.
- Glibert, P. M., Regional studies of daily, seasonal and size fraction variability in ammonium remineralization, *Marine Biology*, 70(2), 209–222, doi:10.1007/BF00397687, 1982.
- Grasshoff, K., K. Kremling, and M. Ehrhardt, *Methods of seawater analysis*, John Wiley & Sons, 1983.

References

- Gruber, N., Ocean biogeochemistry: carbon at the coastal interface, *Nature*, 517(7533), 148–149, doi:10.1038/nature14082, 2015.
- Gruber, N., Z. Lachkar, H. Frenzel, P. Marchesiello, M. Münnich, J. C. McWilliams, T. Nagai, and G.-K. Plattner, Eddy-induced reduction of biological production in eastern boundary upwelling systems, *Nature Geoscience*, 4(11), 787–792, doi:10.1038/ngeo1273, 2011.
- Gunther, E. R., A report on oceanographical investigations in the Peru Coastal Current, *Discovery Rep.*, 13, 107–276, 1936.
- Gutknecht, E., et al., Coupled physical/biogeochemical modeling including O₂-dependent processes in the Eastern Boundary Upwelling Systems: Application in the Benguela, *Biogeosciences*, 10(6), 3559–3591, doi:10.5194/bg-10-3559-2013, 2013.
- Hamersley, M. R., et al., Anaerobic ammonium oxidation in the Peruvian oxygen minimum zone, *Limnology and Oceanography*, 52(3), 923–933, doi:10.4319/lo.2007.52.3.0923, 2007.
- Harrison, W. G., Experimental measurements of nitrogen remineralization in coastal waters, *Limnology and Oceanography*, 23(4), 684–694, doi:10.4319/lo.1978.23.4.0684, 1978.
- Hosegood, P. J., P. Nightingale, A. Rees, C. Widdicombe, M. Woodward, D. Clark, and R. Torres, Nutrient Pumping by Submesoscale Circulations in the Mauritanian Upwelling System Nutrient Pumping by Submesoscale Circulations in the, *Progress in Oceanography*, (October 2017), doi:10.1016/j.pocean.2017.10.004, 2017.
- Hutchins, D. A., et al., Phytoplankton iron limitation in the Humboldt Current and Peru Upwelling, *Limnology and Oceanography*, 47(4), 997–1011, doi:10.4319/lo.2002.47.4.0997, 2002.
- Huyer, A., M. Knoll, T. Palusziewicz, and R. L. Smith, The Peru Undercurrent: a study in variability, *Deep Sea Research Part A. Oceanographic Research Papers*, 38(Supplement 1), S247 – S271, doi:[https://doi.org/10.1016/S0198-0149\(12\)80012-4](https://doi.org/10.1016/S0198-0149(12)80012-4), 1991.
- José, Y. S., H. Dietze, and A. Oschlies, Linking diverse nutrient patterns to different water masses within anticyclonic eddies in the upwelling system off Peru, *Biogeosciences Discussions*, 14(March 2017), 1–20, doi:10.5194/bg-2016-228, 2017.
- Kalvelage, T., et al., Nitrogen cycling driven by organic matter export in the South Pacific oxygen minimum zone, *Nature Geoscience*, 6(3), 228–234, doi:10.1038/ngeo1739, 2013.
- Karstensen, J., and D. Quadfasel, Formation of Southern Hemisphere thermocline waters: Water mass conversion and subduction, *Journal of Physical Oceanography*, 32(11), 3020–3038, doi:10.1175/1520-0485(2002)032<3020:FOSHTW>2.0.CO;2, 2002.
- Karstensen, J., L. Stramma, and M. Visbeck, Oxygen minimum zones in the eastern tropical Atlantic and Pacific oceans, *Progress in Oceanography*, 77(4), 331–350, doi:10.1016/j.pocean.2007.05.009, 2008.
- Keister, J. E., T. J. Cowles, W. T. Peterson, and C. A. Morgan, Do upwelling filaments result in predictable biological distributions in coastal upwelling ecosystems?, *Progress in Oceanography*, 83(1), 303–313, doi:<https://doi.org/10.1016/j.pocean.2009.07.042>, 2009.

- Koné, V., E. Machu, P. Penven, V. Andersen, V. Garçon, P. Fréon, and H. Demarcq, Modeling the primary and secondary productions of the southern Benguela upwelling system : A comparative study through two biogeochemical models, *Gobal Biogeochemical Cycles*, 19, 1–22, doi:10.1029/2004GB002427, 2005.
- Krupke, A., W. Mohr, J. Laroche, B. M. Fuchs, R. I. Amann, and M. M. M. Kuypers, The effect of nutrients on carbon and nitrogen fixation by the UCYN-A – haptophyte symbiosis, *The ISME Journal*, 9(7), 1635–1647, doi:10.1038/ismej.2014.253, 2015.
- Lapeyre, G., and P. Klein, Impact of the small-scale elongated filaments on the oceanic vertical pump, *Journal of Marine Research*, 64(6), 835–851, doi:<https://doi.org/10.1357/02224006779698369>, 2006.
- Lathuilière, C., V. Echevin, M. Lévy, and G. Madec, On the role of the mesoscale circulation on an idealized coastal upwelling ecosystem, *Journal of Geophysical Research: Oceans*, 115(9), 1–14, doi:10.1029/2009JC005827, 2010.
- Lévy, M., Mesoscale variability of phytoplankton and of new production: Impact of the large-scale nutrient distribution, *Journal of Geophysical Research-Oceans*, 108(C11), 3358, doi:10.1029/2002JC001577, 2003.
- Lévy, M., R. Ferrari, P. J. S. Franks, A. P. Martin, and P. Rivière, Bringing physics to life at the submesoscale, *Geophysical Research Letters*, 39(14), 1–13, doi:10.1029/2012GL052756, 2012.
- Loginova, A. N., S. Thomsen, and A. Engel, Chromophoric and fluorescent dissolved organic-matter in and above the oxygen minimumzone off Peru, *Journal of Geophysical Research: Oceans*, pp. 1–18, doi:10.1002/2015JC011534. Received, 2016.
- Macisaac, J. J., R. C. Dugdale, R. T. Barber, and D. Blasco, Primary production cycle in an upwelling center, *Deep-Sea Research*, 32(5), 503–529, 1985.
- Mackas, D. L., L. Washburn, and S. L. Smith, Zooplankton Community Pattern Associated With a California Current Cold Filament, *Journal of Geophysical Research*, 96(C8), 14,781–14,797, 1991.
- Mahadevan, A., The Impact of Submesoscale Physics on Primary Productivity of Plankton, *Annual review of marine science*, (8), 161–184, doi:10.1146/annurev-marine-010814-015912, 2015.
- Mahadevan, A., L. N. Thomas, and A. Tandon, Comment on "Eddy/wind interactions stimulate extraordinary mid-ocean plankton blooms", *Science (New York, N.Y.)*, 320(5875), 448; author reply 448, doi:10.1126/science.1152111, 2008.
- McGillicuddy, D., A. Robinson, D. Siegel, H. Jannasch, R. Johnson, T. Dickey, J. McNeil, A. Michaels, and A. Knap, Influence of mesoscale eddies on new production in the Sargasso Sea, *Nature*, 285(1977), 263–266, 1998.
- McGillicuddy, D. J., L. A. Anderson, S. C. Doney, and M. E. Maltrud, Eddy-driven sources and sinks of nutrients in the upper ocean: Results from a 0.1° resolution model of the North Atlantic, *Global Biogeochemical Cycles*, 17.2(1035), doi:10.1029/2002GB001987, 2003.

References

- McGillicuddy, D. J., et al., Eddy/wind interactions stimulate extraordinary mid-ocean plankton blooms., *Science (New York, N.Y.)*, 316(5827), 1021–6, doi:10.1126/science.1136256, 2007.
- McWilliams, J. C., F. Colas, and M. J. Molemaker, Cold filamentary intensification and oceanic surface convergence lines, *Geophysical research letters*, 36(L18602), 1–5, doi:10.1029/2009GL039402, 2009.
- McWilliams, J. C., J. Gula, M. J. Molemaker, L. Renault, and A. F. Shchepetkin, Filament Frontogenesis by Boundary Layer Turbulence, *Journal of Physical Oceanography*, 45(1981), 1988–2005, doi:10.1175/JPO-D-14-0211.1, 2015.
- Minas, H. J., M. Minas, C. France, and T. T. Packard, Productivity in upwelling areas deduced from hydrographic and chemical fields, *Limnology and Oceanography*, 31(6), 1182–1206, 1974.
- Montes, I., F. Colas, X. Capet, and W. Schneider, On the pathways of the equatorial subsurface currents in the eastern equatorial Pacific and their contributions to the Peru-Chile Undercurrent, *Journal of Geophysical Research: Oceans*, 115(9), 1–16, doi:10.1029/2009JC005710, 2010.
- Nagai, T., Dominant role of eddies and filaments in the offshore transport of carbon and nutrients in the California Current System, *Journal of Geophysical Research: Oceans*, pp. 5318–5341, doi:10.1002/2015JC010889.Received, 2015.
- Nelson, D. M., J. J. Goering, and D. W. Boisseau, Consumption and Regeneration of Silicic Acid in Three Coastal Upwelling Systems, in *Coastal Upwelling*, pp. 242–256, American Geophysical Union, doi:10.1029/CO001p0242, 1981.
- Oerder, V., F. Colas, V. Echevin, S. Masson, C. Hourdin, S. Jullien, G. Madec, and F. Lemarié, Mesoscale SST–wind stress coupling in the Peru–Chile current system: Which mechanisms drive its seasonal variability?, *Climate Dynamics*, 47(7–8), 2309–2330, doi:10.1007/s00382-015-2965-7, 2016.
- Omand, M. M., E. A. D’Asaro, C. M. Lee, M. J. Perry, N. Briggs, I. Cetinić, and A. Mahadevan, Eddy-driven subduction exports particulate organic carbon from the spring bloom, *Science*, 348(6231), 222–225, doi:10.1126/science.1260062, 2015.
- Oschlies, A., Model-derived estimates of new production : New results point towards lower values, *Deep-Sea Research Part II*, 48.10, 2173 – 2197, doi:[https://doi.org/10.1016/S0967-0645\(00\)00184-3](https://doi.org/10.1016/S0967-0645(00)00184-3), 2001.
- Oschlies, A., Can eddies make ocean deserts bloom?, *Global Biogeochemical Cycles*, 16(4), 53–1–53–11, doi:10.1029/2001GB001830, 2002.
- Oschlies, A., and V. Garçon, Eddy-induced enhancement of primary production in a model of the North Atlantic Ocean, *Nature*, 394(6690), 266–269, 1998.
- Packard, T. T., P. C. Garfield, and L. A. Codispoti, *Oxygen Consumption and Denitrification Below the Peruvian Upwelling*, pp. 147–173, Springer US, Boston, MA, doi:10.1007/978-1-4615-6651-9_8, 1983.

- Paulmier, A., D. Ruiz-Pino, V. Garçon, and L. Farías, Maintaining of the Eastern South Pacific Oxygen Minimum Zone (OMZ) off Chile, *Geophysical Research Letters*, 33(20), 2–7, doi: 10.1029/2006GL026801, 2006.
- Pennington, J. T., K. L. Mahoney, V. S. Kuwahara, D. D. Kolber, R. Calienes, and F. P. Chavez, Primary production in the eastern tropical Pacific: A review, *Progress in Oceanography*, 69(2-4), 285–317, doi:10.1016/j.pocean.2006.03.012, 2006.
- Penven, P., C. Roy, G. B. Brundrit, A. de Verdiere, P. Freon, A. S. Johnson, J. R. E. Lutjeharms, and F. A. Shillington, A regional hydrodynamic model of upwelling in the Southern Benguela : research letter, *South African Journal of Science*, 97(11-12), 472–475, 2001.
- Penven, P., V. Echevin, J. Pasapera, F. Colas, and J. Tam, Average circulation , seasonal cycle , and mesoscale dynamics of the Peru Current System : A modeling approach, *Journal of Geophysical Research*, 110(C10021), 1–21, doi:10.1029/2005JC002945, 2005.
- Penven, P., P. Marchesiello, and L. Debreu, Software tools for pre- and post-processing of oceanic regional simulations, 23(2008), 2007–2009, doi:10.1016/j.envsoft.2007.07.004, 2007.
- Pérez-Aragón, M., C. Fernandez, and R. Escribano, Nitrogen excretion by mesozooplankton in a coastal upwelling area: Seasonal trends and implications for biological production, *Journal of Experimental Marine Biology and Ecology*, 406(1), 116–124, doi:<https://doi.org/10.1016/j.jembe.2011.05.029>, 2011.
- Pollard, R. T., and L. A. Regier, Vorticity and Vertical Circulation at an Ocean Front, *Journal of Physical Oceanography*, 22(6), 609–625, doi:10.1175/1520-0485(1992)022<0609:VAVCAA>2.0.CO;2, 1992.
- Rahn, D. A., and R. D. Garreaud, A synoptic climatology of the near-surface wind along the west coast of South America, *International Journal of Climatology*, 34(3), 780–792, doi:10.1002/joc.3724, 2013.
- Redfield, A. C., The influence of organisms on the composition of seawater, *The sea*, 2, 26–77, 1963.
- Renault, L., M. J. Molemaker, J. Gula, S. Masson, and J. C. McWilliams, Control and Stabilization of the Gulf Stream by Oceanic Current Interaction with the Atmosphere, *Journal of Physical Oceanography*, 46(11), 3439–3453, doi:10.1175/JPO-D-16-0115.1, 2016.
- Richardson, A. J., M. C. Pfaff, J. G. Field, N. F. Silulwane, and F. A. Shillington, Identifying characteristic chlorophyll a profiles in the coastal domain using an artificial neural network, *Journal of Plankton Research*, 24(12), p. 1289–1303, 2002.
- Ridgway, K. R., J. R. Dunn, and J. L. Wilkin, Ocean interpolation by four-dimensional weighted least squares - Application to the waters around Australasia, *Journal of Atmospheric and Oceanic Technology*, 19(9), 1357–1375, doi:10.1175/1520-0426(2002)019<1357:OIBFDW>2.0.CO;2, 2002.
- Rossi, V., C. López, J. Sudre, E. Hernández-García, and V. Garçon, Comparative study of mixing and biological activity of the Benguela and Canary upwelling systems, *Geophysical Research Letters*, 35(11), 1–5, doi:10.1029/2008GL033610, 2008.

References

- Rossi, V., C. López, E. Hernández-García, J. Sudre, V. Garçon, and Y. Morel, Surface mixing and biological activity in the four Eastern Boundary Upwelling Systems, *Nonlinear Processes in Geophysics*, 16(4), 557–568, doi:10.5194/npg-16-557-2009, 2009.
- Rudnick, D. L., and J. R. Luyten, Intensive surveys of the Azores Front: 1. Tracers and dynamics, *Journal of Geophysical Research: Oceans*, 101(C1), 923–939, doi:10.1029/95JC02867, 1996.
- Schneider, W., R. Fuenzalida, E. Rodríguez-Rubio, J. Garcés-Vargas, and L. Bravo, Characteristics and formation of Eastern South Pacific Intermediate Water, *Geophysical Research Letters*, 30(11), 1–4, doi:10.1029/2003GL017086, 2003.
- Shchepetkin, A. F., and J. C. Mcwilliams, The regional oceanic modeling system (ROMS): a split-explicit, free-surface, topography-following-coordinate oceanic model, *Ocean Modelling*, 9(2005), 347–404, doi:10.1016/j.ocemod.2004.08.002, 2004.
- Silva, N., N. Rojas, and A. Fedele, Water masses in the Humboldt Current System: Properties, distribution, and the nitrate deficit as a chemical water mass tracer for Equatorial Subsurface Water off Chile, *Deep-Sea Research Part II: Topical Studies in Oceanography*, 56(16), 992–1008, doi:10.1016/j.dsr2.2008.11.001, 2009.
- Smith, R. L., *Circulation Patterns in Upwelling Regimes*, pp. 13–35, Springer US, Boston, MA, doi:10.1007/978-1-4615-6651-9_2, 1983.
- Stewart, K. D., A. M. C. Hogg, S. M. Griffies, A. P. Heerdegen, M. L. Ward, P. Spence, and M. H. England, Vertical resolution of baroclinic modes in global ocean models, *Ocean Modelling*, 113, 50–65, doi:10.1016/j.ocemod.2017.03.012, 2017.
- Stramma, L., S. Schmidtko, L. a. Levin, and G. C. Johnson, Ocean oxygen minima expansions and their biological impacts, *Deep-Sea Research Part I: Oceanographic Research Papers*, 57(4), 587–595, doi:10.1016/j.dsr.2010.01.005, 2010.
- Strub, P., J. Mesías, V. Montecino, J. Rutlant, and S. Salinas, Coastal ocean circulation off western South America, 1998.
- Strub, P. T., P. M. Kosro, and A. Huyer, The nature of the cold filaments in the California Current system, *Journal of Geophysical Research*, 96(C8), 14,743, doi:10.1029/91JC01024, 1991.
- Stuart, D. V., Sea-Surface Temperatures and Winds During Joint II: Part II. Temporal Fluctuations, in *Coastal Upwelling*, pp. 32–38, American Geophysical Union, doi:10.1029/CO001p0032, 1981.
- Stukel, M. R., H. Song, R. Goericke, and A. J. Miller, The role of subduction and gravitational sinking in particle export, carbon sequestration, and the remineralization length scale in the California Current Ecosystem, *Limnology and Oceanography*, pp. 1–21, doi:10.1002/lno.10636, 2017a.
- Stukel, M. R., et al., Mesoscale ocean fronts enhance carbon export due to gravitational sinking and subduction, *Proceedings of the National Academy of Sciences*, 114(6), 1252–1257, doi:10.1073/pnas.1609435114, 2017b.

- Sverdrup, H. U., M. W. Johnson, R. H. Fleming, and Others, *The Oceans: Their physics, chemistry, and general biology*, vol. 7, Prentice-Hall New York, 1942.
- Thomas, L. N., A. Tandon, and A. Mahadevan, Submesoscale Processes and Dynamics, in *Ocean Modeling in an Eddying Regime*, pp. 17–38, doi:10.1029/177GM04, 2008.
- Thomas, L. N., A. Tandon, and A. Mahadevan, Submesoscale Processes and Dynamics, in *Ocean Modeling in an Eddying Regime*, pp. 17–38, American Geophysical Union, doi:10.1029/177GM04, 2013.
- Thomsen, S., T. Kanzow, F. Colas, V. Echevin, G. Krahmann, and A. Engel, Do submesoscale frontal processes ventilate the oxygen minimum zone off Peru ?, *Geophysical Research Letters*, pp. 8133–8142, doi:10.1002/2016GL070548.Abstract, 2016a.
- Thomsen, S., T. Kanzow, G. Krahmann, R. J. Greatbatch, M. Dengler, and G. Lavik, The formation of a subsurface anticyclonic eddy in the Peru-Chile Undercurrent and its impact on the near-coastal salinity, oxygen, and nutrient distributions, *Journal of Geophysical Research: Oceans*, pp. 476–501, doi:10.1002/2015JC010878.Received, 2016b.
- Veitch, J., P. Penven, and F. Shillington, The Benguela: A laboratory for comparative modeling studies, *Progress in Oceanography*, 83(1-4), 296–302, doi:10.1016/j.pocean.2009.07.008, 2009.
- Veldhuis, M. J., and G. W. Kraay, Phytoplankton in the subtropical Atlantic Ocean: Towards a better assessment of biomass and composition, *Deep-Sea Research Part I: Oceanographic Research Papers*, 51(4), 507–530, doi:10.1016/j.dsr.2003.12.002, 2004.
- Vélez-Belchí, P., and J. Tintoré, Vertical velocities at an ocean front, *Scientia Marina*, 65(S1), 291–300, 2001.
- Vergara, O. A., V. Echevín, H. Hito, and R. A. Quiñones, Controlling factors of the seasonal variability of productivity in the southern Humboldt Current System (30 – 40 ° S): A biophysical modeling approach, *Continental Shelf Research*, 148(July), 89–103, doi:10.1016/j.csr.2017.08.013, 2017.
- Walsh, J. J., Herbivory as a factor in patterns of nutrient utilization in the sea, *Limnology and Oceanography*, 21(1), 1–13, doi:10.4319/lo.1976.21.1.0001, 1976.
- Walsh, J. J., J. C. Kelley, R. C. Dugdale, and B. W. Frost, Gross features of the Peruvian upwelling system with special reference to possible diel variation, *Invest. Pesq*, 35, 25–42, 1971.
- Whitledge, T. E., Nitrogen Recycling and Biological Populations in Upwelling Ecosystems, in *Coastal Upwelling*, pp. 257–273, American Geophysical Union, doi:10.1029/CO001p0257, 1981.
- Worley, S. J., S. D. Woodruff, R. W. Reynolds, S. J. Lubker, and N. Lott, ICOADS release 2.1 data and products, *International Journal of Climatology*, 25(7), 823–842, doi:10.1002/joc.1166, 2005.
- Wyrtki, K., The oxygen minima in relation to ocean circulation, *Deep Sea Research and Oceanographic Abstracts*, 9, 11–23, doi:10.1016/0011-7471(62)90243-7, 1962.

References

- Wyrki, K., *The horizontal and vertical field of motion in the Peru Current*, University of California Press, 1963.
- Wyrki, K., Circulation and Water Masses in the Eastern Equatorial Pacific Ocean, *Int. J. Oceanol. & Limnol.* Vol. 1(2), 117–147, 1967.
- Zuta, S., and W. Urquiza, Temperatura promedio de la superficie del mar frente a la costa peruana, periodo 1928-1969, *Boletin Instituto del Mar del Peru*, 2, 459–520, 1972.

Acknowledgements

I would sincerely like to thank Andreas Oschlies for his supervision and helpful comments, Søren Thomsen for providing me with an interesting research topic, conducting the fieldwork and for many helpful suggestions that substantially improved this thesis, Vincent Echevin for sharing his ocean modeling expertise and for fruitful discussions, Yonss José for running the simulations even though she has been on parental leave, and Laura Brisstow and Gaute Lavik for conducting fieldwork, helpful discussions and their hospitality in Bremen. Furthermore, I would like to thank Ioana Ivanciu for keeping her positive attitude and René Schubert and Joost Hemmen for lunchtime discussions about music, politics and everything. Finally, I would like to thank Bodil Rühs for her patience and for taking care of me even when I didn't.

Erklärung

Hiermit erkläre ich, dass ich die vorliegende Arbeit selbstständig und ohne fremde Hilfe angefertigt und keine anderen als die angegebenen Quellen und Hilfsmittel verwendet habe. Die eingereichte schriftliche Fassung der Arbeit entspricht der auf dem elektronischen Speichermedium.

(Name der Datei: Hauschildt_5657.pdf)

Weiterhin versichere ich, dass diese Arbeit noch nicht als Abschlussarbeit an anderer Stelle vorgelegt hat.

Datum, Unterschrift

Jaard-Okke Frederik Hauschildt